A PARAMETRIC MODEL FOR THE ANALYSIS AND QUANTIFICATION OF FOVEAL SHAPES

Der Fakultät für Mathematik und Informatik
der Universität Leipzig
eingereichte

DISSERTATION

zur Erlangung des akademischen Grades

DOCTOR RERUM NATURALIUM
(Dr. rer. nat.)

im Fachgebiet

Informatik

vorgelegt

von Dipl.-Inf. Patrick Scheibe

geboren am 05.11.1979 in Markranstädt

Die Annahme der Dissertation wurde empfohlen von:
Prof. Dr. Peter F. Stadler, Universität Leipzig

Die Verleihung des akademischen Grades erfolgt mit Bestehen
der Verteidigung am 13.06.2019 mit dem Gesamtprädikat
magna cum laude

To Jens-Peer, my teacher, mentor and friend

1963 – 2009

ABSTRACT

Recently, the advance of optical coherence tomography (OCT) enables a detailed examination of the human retina in-vivo for clinical routine and experimental eye research. One of the structures inside the retina of immense scientific interest is the fovea, a small retinal pit located in the central region with extraordinary visual resolution. Today, only a few investigations captured foveal morphology based on a large subject group by a detailed analysis employing mathematical models.

In this work, we develop a parametric model function to describe the shape of the human fovea. Starting with a detailed discussion on the history and present of fovea research, we define the requirements for a suitable model and derive a function which can represent a broad range of foveal shapes. The model is one-dimensional in its basic form and can only account for the shape of one particular section through a fovea. Therefore, we apply a radial fitting scheme in different directions which can capture a fovea in its full three-dimensional appearance. Highly relevant foveal characteristics, derived from the model, provide valuable descriptions to quantify the fovea and allow for a detailed analysis of different foveal shapes.

To put the theoretical model into practice, we develop a numerical scheme to compute model parameters from retinal OCT scans and to reconstruct the shape of an entire fovea. For the sake of scientific reproducibility, this section includes implementation details, examples and a discussion of performance considerations.

Finally, we present several studies which employed the fovea model successfully. A first feasibility study verifies that the parametric model is suitable for foveal shapes occurring in a large set of healthy human eyes. In a follow-up investigation, we analyse foveal characteristics occurring in healthy humans in detail. This analysis will concern with different aspects including, e.g. an investigation of the fovea's asymmetry, a gender comparison, a left versus right eye correlation and the computation of subjects with extreme foveal shapes. Furthermore, we will show how the model was used to support investigations unrelated to the direct quantification of the fovea itself. In these investigations we employed the model to compute anatomically correct regions of interest in an analysis of the outer choroid boundary (OCB) and the calculation of an *average* fovea for an optical simulation of light rays. We will conclude with currently unpublished data that shows the fovea modelling of hunting birds which have unusual, funnel-like foveal shapes.

PUBLICATIONS

Throughout this thesis, we present ideas, methods and figures that were published in the articles shown below. The research regarding the modelling of the foveal shape started in 2013 when we began to analyse optical coherence tomography (OCT) datasets and concluded that a mathematical description of the foveal shape would lead to an improved understanding of its morphology. This initial work resulted in an article that presented the model and showed how its parameters were calculated from OCT data [1].

In a next step, we applied the model to subjects that were part of a larger study on strictly controlled healthy eyes in the range of 21 to 77 years of age. The goal was to characterise the morphology of the human fovea and provide insight into shape similarities and differences regarding, e.g. age or gender [2].

The fovea model was also used to support various other experiments that did not aim to quantify the shape of the fovea. Still, the model played a significant role in these analyses by providing information like regions of interest or selections of OCT scans which represent an average foveal shape from an extensive database [3, 4].

To carry out the calculation of determining the properties and characteristics of the model function, a computer algebra system (CAS) that is strong in symbolic computation is helpful. Since finding the antiderivative of symbolic expressions is typically hard, we worked on Rubi, a system for rule-based integration that can be used with several open-source CAS and can solve the integration problems occurring in this thesis [5].

Finally, the source code required for importing OCT data and modelling foveae is publicly available on the author's GitHub page.[1] A custom import library was developed to use data from the SPECTRALIS SD-OCT (Heidelberg Engineering) which provides both a *Mathematica* package and a Java interface. The implementation of this library is available in the `spectralis-raw-data` repository. For the modelling of foveae, a *Mathematica* package can be downloaded from the `FoveaAnalysis` repository.

[1] Patrick Scheibe, Anfisa Lazareva, Ulf-Dietrich Braumann, Andreas Reichenbach, Peter Wiedemann, Mike Francke, and Franziska G. Rauscher. „Parametric model for the 3D reconstruction of individual fovea shape from OCT data." In: *Experimental Eye Research* 119 (Feb. 2014), pp. 19–26. DOI: 10.1016/j.exer.2013.11.008.

[2] Patrick Scheibe, Maria T. Zocher, Mike Francke, and Franziska G. Rauscher. „Analysis of foveal characteristics and their asymmetries in the normal population." In: *Experimental Eye Research* 148 (2016), pp. 1–11. ISSN: 0014-4835. DOI: 10.1016/j.exer.2016.05.013.

[3] Marcus Wagner, Patrick Scheibe, Mike Francke, Beatrice Zimmerling, Katharina Frey, Mandy Vogel, Stephan Luckhaus, Peter Wiedemann, Wieland Kiess, and Franziska G. Rauscher. „Automated detection of the choroid boundary within OCT image data using quadratic measure filters." In: *Journal of Biomedical Optics* 22.2 (Feb. 2017), p. 025004. DOI: 10.1117/1.jbo.22.2.025004.

---

1 https://github.com/halirutan

[4] Katharina Frey, Beatrice Zimmerling, Patrick Scheibe, Franziska G. Rauscher, Andreas Reichenbach, Mike Francke, and Robert Brunner. „Does the foveal shape influence the image formation in human eyes?“ In: *Advanced Optical Technologies* 6.5 (2017), pp. 403–410. DOI: 10.1515/aot-2017-0043.

[5] Albert Rich, Patrick Scheibe, and Nasser Abbasi. „Rule-based integration: An extensive system of symbolic integration rules.“ In: *Journal of Open Source Software* 3.32 (Dec. 2018), p. 1073. DOI: 10.21105/joss.01073.

People who see life as anything more than pure entertainment
are missing the point.

— George Carlin

ACKNOWLEDGMENTS

Scientists are a unique bunch of people because we don't see work as *work*, that is, we don't see work as a daytime job from 8 am to 5 pm. Instead, we find interesting questions everywhere, and we like to spend every free minute on them. With a family and four children, this is an impossible combination unless you have a partner who is remarkably understanding.

I am lucky I found someone like that in my wife, Sophia. You support me every single day by keeping things off of my back and giving me the freedom to spend as much time as possible with my projects and our children. I love you for accepting my weird ways and for continuously supporting me over the years. Without you, all this would not have been possible.

The same goes for my parents, my grandparents and my little brother. It is rare today to have all of your loved ones within walking distance, and I am glad that we stuck so close together. I want to thank my mom in particular for constantly believing in what I did. To this day she may not be able to describe what exactly I am doing when I sit in front of a computer. Still, she never questioned my ways, even when we met early in the morning while she was going to work and I was heading for bed. Thank you tremendously for the faith you put in me.

During my work at the university, I met exceptional people who influenced me in one way or another and who I dearly want to thank for being part of my life. In particular, I want to acknowledge Franziska Rauscher, Mike Francke, Marcus Wagner, and Andreas Reichenbach. I have never worked in a more encouraging environment, and you were the reason why. Likewise, I thank my former colleague Ulf-Dietrich Braumann and my dear friend and colleague Karsten Winter who shared the office with me. Talking to you and discussing philosophical, political, or even trivial matters has always been a pleasure.

I also thank my dear friend Carolin for constantly challenging my views. You are the one who always sees things a bit differently, and you are never afraid of speaking up. For that and for your constant support and your friendship I am profoundly grateful.

The one person I would like to thank the most is not among us anymore. He was the one who guided me through my final years at university and offered me a position as his PhD student after I had finished my diploma thesis. I was allowed to enjoy another two years working beside him before he unexpectedly passed away on a summer day in 2009 at only 44 years old. His name is Jens-Peer Kuska.

Jens was exceptional in many ways. Those who knew him have their own stories to tell. As a theoretical physicist, he was unbelievably bright and had an astonishing gift to solve problems and put the solutions to practical use. His knowledge, not only about mathematics, physics and programming, but also about biology, literature and history seemed unlimited. From the very beginning, I admired his unique talent to explain things in simple words and to make complicated topics understandable. Words cannot express how

much I value the time I had with him and how much it still hurts that he had to go so soon.

I express my deepest gratitude to the people who stepped in and helped me with this work. Peter Stadler did not hesitate when I asked him to mentor this thesis, and his enormous experience with guiding PhD students was irreplaceable. Andreas Reichenbach, Franziska Rauscher and Mike Francke were unbelievably kind, and it has always been a pleasure to discuss biology with them. Also, by pure chance, we were most lucky to welcome Marcus Wagner, a mathematician, in our team. He was a life-saver when it came to helping with mathematical problems. Last but not least, I am grateful that Markus Löffler has been a constant throughout all of my years at the university. Although I never mentioned it personally, I hope he noticed that to me he always has been a role-model of a true *leader*.

CONTENTS

LIST OF FIGURES

1

INTRODUCTION

The human eye can be considered the most important sense organ. Our vision helps us to perceive our surroundings and to navigate through the environment.

The structure of the eye shares fundamental properties with a digital camera. The cornea and the lens in the front of the eye focus light onto the photoreceptors of the retina, while the optical lens system of the camera ensures a sharp image on the imaging sensor.

Unlike the sensor of the camera, which usually does not process the picture it is capturing, the human retina pre-processes acquired information before it reaches the brain to form the final optical sensation. The retinal pre-processing has developmental reasons because the eye and the light-sensitive retina are exterior parts of the brain and some of their neuronal processing power has remained [1].

Another difference in the camera-eye comparison is that the photoreceptor cells are not equally distributed in the retina. A central region exists with a higher density of photoreceptors called the *area centralis*. In this area, most humans possess a unique structure which forms a small pit in the retinal layers: the fovea. The foveal region is of utmost interest as it is the place with the highest visual resolution.

Humans are not the only species that posses a fovea. Similar structures were found in birds, reptilians and other animals. Some birds even possess two foveae, because they have two separated fields of vision: one for binocular viewing, where an image is formed by combining the information from both eyes, and one for monocular viewing that is employed when keeping small prey animals in visual focus. While their temporal fovea for binocular vision has a shallow shape similar to the human fovea, their central fovea is deep and funnel-like [2].

Although the structure of the retina and the ontogenesis of the foveae are different in humans and birds, it raises the question if the shape of the fovea serves an optical function that improves vision. In this regard, the inter-species comparison is interesting, as we know that some birds of prey have superior vision compared to humans and they can track even tiny prey animals from a large distance high above. Arguing that they might have a higher photoreceptor density and, therefore, a better visual resolution, has theoretical boundaries as the smallest dimension of photoreceptor cells is biologically limited. Thus, gaining more resolution cannot solely be realised by a higher packing of photoreceptors and the fovea has been suspected to play a role in superior vision [2].

Even among humans, the shape of the fovea is highly variable. To this day, it was not possible to successfully demonstrate an existing relationship between the form of the fovea and the quality of central vision, even though it has been postulated for almost a century that the shape of the fovea might

be an essential factor. Therefore, a detailed analysis of existing foveal shapes, their differences and an assessment of shape characteristics and properties is the first step to a better understanding of the importance of the foveal pit and its role in the quality of vision.

In this work, we will develop a parametric model to describe the structural form of human foveae. We will start with a short review of the anatomy of the eye, followed by a detailed discussion of early publications of foveal research to motivate the long-lasting interest in the form and function of foveae. In this historical review, we will highlight which hypotheses of the fovea's visual function were made. In contrast to the research of the 20th century, more recent publications about foveal morphology use optical coherence tomography (OCT), a technique for obtaining in-depth images of the retina in-vivo. Since the analyses in this work will also be based on OCT imaging, we will include a summary of this technique before we review recent publications which were concerned with the mathematical modelling of foveae.

Taking current research into account, we will motivate the requirements for a model and derive a function that is suitable for representing a broad range of possible foveal shapes. The model equation is one-dimensional in its basic form and can only account for the shape of one particular section through any fovea. Therefore, we will present how this can be extended to describe a fovea in its full three-dimensional appearance by developing a radial fitting technique that is suitable for the circular structure of foveae. Furthermore, we will discuss foveal characteristics that are derived from the model and can be used to describe and quantify foveal shapes in a more natural way.

Before we can turn to the analysis of in-vivo OCT data, a numerical scheme is required to compute model parameters from retinal OCT scans. Therefore, we will develop an algorithm that can fit the model parameters to a particular OCT scan. Starting from the initial OCT scan, we will present all necessary steps and also discuss computational details like parallelisation.

Following that, we present results that show where the method was successfully applied in scientific projects. This discussion will include a detailed analysis of a large set of retinal scans to find structural characteristics of foveae in the normal population. Furthermore, we will show how a quantification of the choroid boundary can take advantage of a previous calculation of foveal properties and how the model can support refraction simulations.

Finally, we will conclude with a critical discussion of the strengths and weaknesses of the overall approach, and end with an outlook showing next steps and future goals.

<div align="right">

2

</div>

BACKGROUND

In this chapter, we will shortly review the anatomy of the human eye and the fovea centralis in particular. This will provide us with the required knowledge about its structure, and it will define the terminology used throughout this thesis. Furthermore, we will have a closer look at the fovea-research of the last century as it helps motivate the vast interest in the form and function of the fovea. Before turning to the results of recent publications of the field, a brief introduction of optical coherence tomography (OCT) will explain how the data used in most recent studies and in this thesis is acquired. We will close this chapter by reviewing recent articles where mathematical models of the fovea were employed to describe its shape.

2.1 THE STRUCTURE OF THE EYE AND THE FOVEA CENTRALIS

To understand the importance of the fovea centralis[1], we will first review the structure of the eye and the pathway of the light inside it. Figure 2.1 shows a schematic section through a human eye. Light entering the eye firstly penetrates the cornea, the most refractive component in the optical system. In fact, the cornea has a refractive power of about 43 dpt which is considerably higher than that of the lens. The human lens is flexible and its form and curvature is influenced by the suspensory ligament that can stretch it. Therefore, it can change its refractive power in a range of 19 dpt to 33 dpt which gives the eye the ability to focus objects in different distances. Unfortunately, humans lose this ability to some degree in higher age [3]. At

---

1 From now on, we will use the term fovea interchangeably with fovea centralis. For the human eye, the exact specification *fovea centralis* is not required, because unlike some other species, humans only possess one fovea. Some birds, for instance, possess a second fovea, a fovea temporalis, and in such cases an exact specification is necessary.
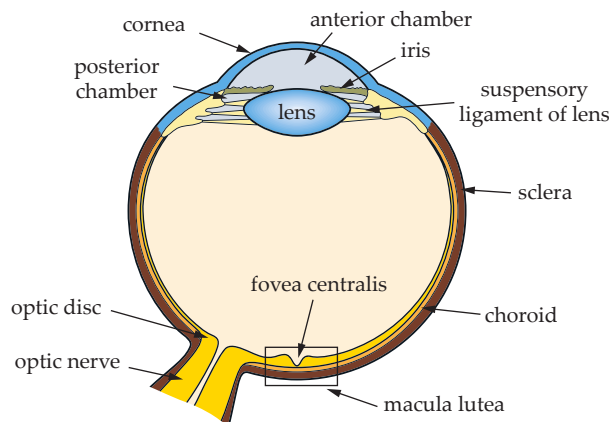
Figure 2.1: Schematic illustration of the eye and its parts.

a microscopic level, the crystalline lens is a highly complex structure that consists of hexagonal cross-sections of fibre cells and its refractive properties vary in different regions [4]. To adapt to differently bright environments, the amount of incoming light can be adjusted by opening and closing of the iris, which resides before the lens and acts like the aperture of a digital camera.

After passing the front part of the eye, the light travels through the vitreous, a gel-like substance inside the eyeball, and reaches the retina at the back of the eye, where a focused projection of the observed object appears. Inside the retina, light-sensitive photoreceptors transform the photons into signals that are intra-retinally processed and transmitted through the optic nerve to the brain.

The human retina contains two major types of photoreceptors: rods and cones (a third type was found in some mammals [5]). While rods are extremely sensitive and are possibly activated by a single photon, they do not provide colour information [6]. Cones, on the other hand, need a substantially higher activation energy but their different subtypes are activated by different wavelengths and, therefore, cones are responsible for colour vision.

Although the incoming light illuminates a substantial portion of the rear part of the eye, it is the central vision that has the highest resolving power. The box in Figure 2.1 marks this location on the retina, and, in human eyes it is called *macula lutea* or yellow spot due to its yellow colouring [7, 8]. However, as not all species develop such yellow colouring as humans do, the term *area centralis* is preferable.

The position of the *area centralis* at the back of the eye is advantageous, since the optical axis of the lens goes through this region and, therefore, incoming light illuminating this portion is least affected by optical artefacts like aberrations. Additionally, the retina shows several specialisations to maximise the visual resolution in the *area centralis*. One prominent feature is that this region contains almost no rods and is tightly packed with colour-sensitive cones. Another specialisation is the fovea, a small retinal pit in the centre of the area central. In the next section, we will take a closer look at its most important features.

2.1.1 *Fovea Centralis*
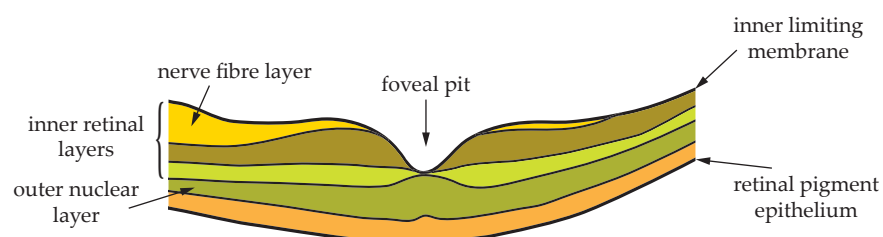
Figure 2.2: Simplified schematic of the retinal layers through the central part of the fovea. During development of the fovea, the inner retinal layers (IRL) are pushed outwards forming the foveal pit, while the outer nuclear layer (ONL) is thickened providing a dense packing of photoreceptors to increase the resolution.

The fovea is a small pit that is found in the *area centralis* of some primates, birds, lizards and fish [2, 9]. Most humans possess a fovea, although their shape varies in the population. The pit has a mean diameter from rim to rim of 1.75 mm and a mean depth of 128 µm. In comparison, the mean value

of the minimal retinal thickness inside the foveal pit is 230 µm, while it is 357 µm at the thick foveal rim [10].

As shown in Figure 2.2, the foveal pit is formed by a structural change of the retinal layers in the central region. During its post-natal development, the inner retinal layers undergo an outward or centrifugal movement that pushes them away from the foveal centre. This shift is the main cause for the formation of the pit. In contrast, the layers below, and the outer nuclear layer (ONL) in particular, become thicker by increasing the number of cells towards the centre in a centripetal movement. The denser packing of photoreceptors in the centre increases the resolution capacity in this area dramatically. However, to achieve a higher density of photoreceptors, they must become more slender and elongated, which then results in a thicker ONL.

While the thickening of the ONL is required to gain more resolution in the area centralis, the outward movement of the inner retinal layers (IRL) is still not completely understood. One common assumption is that the clearing of the central area from IRL reduces the scattering of incoming light in these layers and provide a direct pathway to the photoreceptors. As we will see in the next section, many scientists have discussed this topic critically.

In addition to the difference in retinal layers, the area of the fovea is an avascular zone, i.e. it is not crossed by blood vessels, which also reduces light scattering in the region of the highest vision. This zone is commonly referred to as foveal avascular zone (FAZ) and it was possible to find correlations between the morphology of the FAZ and the fovea [11].

Figure 2.3 shows the scheme of the vascular system of the retina with the central area free from vessels which instead are led around this region, building a ring and leaving out the inner part. Although not shown here, the nerve fibres form a similar pattern, because, as indicated in Figure 2.2, the nerve fibre layer (NFL) is one of the layers that is pushed outwards and is not present in the foveal region. Therefore, the path of nerve fibres bypasses the area centralis as well and we refer to Figure 3 in Lamparter et al. [12].

In conclusion, the fovea is a highly specialised, avascular area with an altered structure of retinal layers. When it is fully developed, the IRL are pushed towards its side while the ONL is thickened to account for the higher number of photoreceptors. The fovea represents the area of the highest resolution in the human retina.

This overview of the eye's structure and the fovea can only serve as a very compact illustration of the matter. We refer to Walls [2] for a more detailed presentation of their anatomy and to Bringmann et al. [9] for the primate fovea in particular. For a general overview of the human eye, the reader can turn to the book of Trotter [3].

2.1.1.1 *Foveal measurement grids and terminology*

To classify different regions around the *area centralis*, literature presents several attempts to define circular grids with fixed sizes that reflect the underlying foveal structure to some degree. Figure 2.3 shows a top-view onto the retina with two of such grids [13, 14].

The first one in Figure 2.3a defines four radial regions around the fovea centre with diameters 0.35 mm, 1.5 mm, 2 mm and 6 mm and refers to them with foveola, fovea, parafoveal region and perifoveal region respectively. The innermost region, the foveola, aims to resemble the bottom part inside the foveal pit.
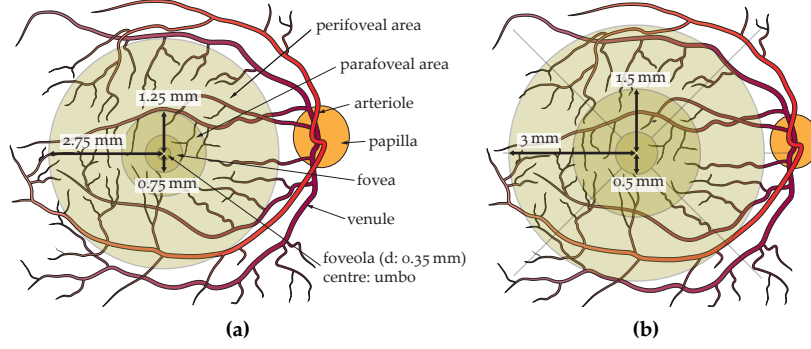
Figure 2.3: Foveal regions and the vascular system. Both figures show a reproduction of the vascular system of the author's right eye that was created using an infrared image of the retina. (a) shows the classification into different foveal zones after Yanoff and Duker [13]. (b) shows the nine-field ETDRS grid that has become the *de facto* standard grid used in academic publications and in most OCT devices [14].

However, the most commonly used measurement grid was introduced for a diabetic retinopathy study [14]. It is depicted in Figure 2.3b and consists of three radial regions and a division into sectors. The innermost circle has a diameter of 1 mm and is surrounded by two outer rings with a diameter of 3 mm and 6 mm respectively. The two outer rings are divided into four sectors that resemble the anatomical directions nasal, superior, temporal and inferior. Nasal is the direction on the retina that points to the optic nerve head (papilla), i.e. the sectors to the right of the fovea in the depicted right eye of Figure 2.3b. The temporal direction is the one opposite to the nasal direction on the retina, while superior and inferior denote the up- and down-direction respectively.

The Early Treatment Diabetic Retinopathy Study Research Group (ETDRS) grid with its nine sectors is widely used in many publications today. For example, retinal thicknesses inside the central 1 mm disk in particular is often analysed. There are two measures here that are of interest: The minimal retinal thickness inside the foveal centre and the mean retinal thickness of the aforementioned 1 mm circle. In this thesis, we will denote the first one as minimal central retinal thickness in the fovea (CRT_{min}) and the latter one as central foveal subfield thickness (CFST).

Please note that terminology is not consistent and some publications denote CFST as foveal central subfield (FCS) [15], CSF² [16] or simply central retinal thickness in the fovea (CRT) [17, 18]. Also, Grover et al. [16] denote the CRT_{min} as central point thickness (CPT).

2.2 HISTORY OF FOVEA RESEARCH

In this section, we want to revisit significant historical publications to get an insight into different existing, and often contradictory, beliefs about the function of foveae before modern technology made an in-vivo examination of human eyes possible. Most of these papers investigated foveae of animals rather than humans for the apparent reason that animal eyes were more accessible. Nevertheless, the conclusions drawn there can to some extent be generalised.

---

2 This acronym was probably an unintended error, since the author refer to it as *central foveal subfield* but used CSF throughout the manuscript.

One problem in earlier days was that an in-vivo examination of the retina was not possible. Histological sections, which are often affected by shrinking artefacts, were the only resources to gain insight into the retina's internal structures. Therefore, scientists needed to be careful with their conclusions as it was not evidently clear whether structural anomalies indeed represent the reality.

The history of foveal research is more than a century old but was mainly initiated by the work of Gordon L. Walls in 1937. Walls not only described the shape of the fovea but even presented an explanation how the form might advance the quality of the retinal image. After the initial work of Walls, a series of high impact publications appeared throughout the century that critically discussed the matter. Those publications often presented a different working hypothesis for Walls' theories that could hardly be validated by facts and measurements.

In 1937, Walls published a first article with the title "Significance of the foveal depression" [19]. According to that work, there was a common belief that the development of a fovea, thus the outward displacement of the IRL, permits incoming light to reach the photoreceptors without being influenced by scattering in the layers above. Walls continued by indicating that this assumption must be flawed as the "perfect clarity of the living retina renders this dubious" [19]. There is no indication that retinal tissue is optically less penetrable than the vitreous that fills the inner eye. Furthermore, Walls objects that if the removal of retinal layers is the sole reason for a fovea, there would hardly be a reason for the different varieties in the shape of highly developed foveae [19].

Walls exemplifies this assumption by comparing different species of animals and eyes within the same species. He argues that a shallow fovea, that he called *concaviclivate*, often appears in animals that are either poor-sighed or have all-round eyes that are not specialised for high acuity vision. An interesting example is the eye of the hawk that has a funnel-like central and a shallow temporal fovea. The funnel-like, deep fovea is referred to as *convexiclivate* and its shape that is shown in Figure 2.4 is different from the human fovea in Figure 2.2.

Anatomically, it is reasonable that the location of the fovea centralis enables the high acuity vision needed to spot small prey animals on the ground whereas the fovea temporalis is used for binocular vision and therefore may not require this specialisation.

From these assumptions, he concluded that the reason for a fovea must be a different one. Especially, the differences in the foveal shapes, as Walls saw it, are likely to influence the visual performance of the eye. Walls hypothesised that since the refractive index[3] of vitreous and retina is different, the incoming light would be refracted at their boundary. If the light hits this boundary perpendicular, the ray is, following the laws of optics, not refracted. As illustrated in Figure 2.4 the angle between the incoming light-ray and the boundary is not 90° at the walls of the foveal pit. The refraction depends on the shape of the fovea and will be greater for steep foveae. According to Walls, "the foveal depression is designed deliberately to take advantage of this refraction", because "the retinal image is expanded on its way through the retinal tissue, and is thus magnified somewhat" [2].

---

3 The refractive index or (or sometimes optical density) is a dimensionless number describing the light propagation through a material. For our observations, it is enough to notice that light passing the boundary between two materials at some angle is refracted when their refractive indices are different. The refraction then depends on the angle at which the incoming light hits the boundary and the ratio between the indices of the two materials.
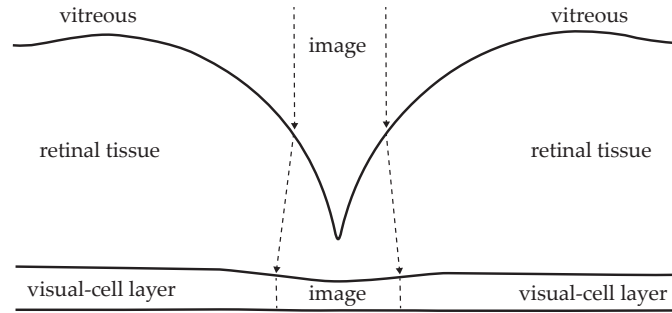
Figure 2.4: Example of the foveal shape of a bird of pray showing the hypothesis of local magnification due to the convexiclivate foveal depression. Incoming light is refracted when it hits the retinal surface at a non-vertical angle. This happens because the refractive index of the vitreous is smaller than that of the retinal tissue. The refraction of light leads here to a magnified image on the photoreceptors (visual cell layer). Adaption of Figure 76 from [2, p. 183].

One crucial prerequisite for the aforementioned refraction is a difference in refractive indices between vitreous and retinal tissue. While Walls only speculated about this in his first article [19], he later discovered an old publication of Valentin [20] who had already measured the refractive indices for vitreous and retinal tissue. Walls published the missing refractive indices in a postscript [21], and included an updated version of the matter two years later in his book [2].

Valentin measured vitreous and retina of different species, and in particular, he found a refractive index of 1.3395 for the vitreous and 1.3488 for the retinal tissue in humans. For other species, he found similar refractive indices with the one of the retina always being higher. These measurements supported the hypothesis of Walls and according to him, the different refractive indices lead to a linear magnification of about 13 % in birds.

However, as reproduced in Figure 2.4, Walls exemplified his theory with only two light-rays. This representation of the situation is misleading as it does not immediately show that only a portion of the incoming light is magnified. In fact, parts of the image near the boundary of the fovea will be contracted. The image projected on the photoreceptors is, therefore, somewhat distorted and not uniformly magnified.

This shortcoming was pointed out several years later by Pumphrey who developed a simpler model by resembling the foveal shape using circle quadrants [22]. Circles had the advantage that Pumphrey was able to calculate exact displacements introduced by the foveal surface when computational power was not available as it is today. Additionally, the circle quadrants resembled the form of a central fovea that was published by Polyak [23] to a reasonable degree.

The conclusion of this investigation was that the fovea's primary purpose is not to provide a higher acuity by magnifying the image. The purpose of a convexiclivate fovea is the "maintenance of accurate fixation and the sensitive appreciation of angular movements of a fixated object" [22]. Therefore, Pumphrey suggests that the local distortion introduced by a steep fovea helps the eye to keep track of small, moving objects. When both eyes are employed for binocular vision, these local disturbances would have a negative effect when combining two images to a stereo representation. Therefore, Pumphrey indicated a possible explanation why shallow foveae are often found in species that use both eyes to form one image.

To put this into perspective, two things are worth mentioning: for one, the work of Walls, Pumphrey and the references therein focused on the understanding of highly developed, non-human foveae. They mainly investigated the deep funnel-like foveae of birds. Nevertheless, the goal was to understand the function of the foveal pit and to draw conclusions even regarding the role of the fovea in humans.

Secondly, although it might seem that there was a gradual gain of knowledge and a shared belief as research moved forward, this was actually not the case. Even in the middle of the 20th century, after Walls and Pumphrey had published their work, the opinions about the function of the fovea were divided. For instance, both Fulton and Wolff [24, 25] still held the belief that retinal layers inside the fovea were spread aside to provide a direct path for the light onto the photoreceptors.

In 1966, Weale [26] attempted to give insight why the human retina possesses a fovea. In his work, Weale concentrated on whether light is indeed scattered by the retina and whether the purpose of a fovea is to minimise this scattering by clearing the central part of the eye from retinal layers. The analysis was based on a previous work [27] where polarised light was projected onto the retina and the reflected light was measured. The apparatus was based on a fundus reflectometer and the experiment showed that reflections consisted not solely of polarised light. It also contained a diffusely reflected component and Weale identified the amount of both, i.e. the amount of polarised light p and the amount of diffusely reflected light d. From these two quantities, a ratio $P_\lambda = p/(p+d)$ was obtained that represented to what degree the retina has scattered the polarized source light in this experiment.

The hypothesis was that if the existence of a fovea indeed "clears" the light path, then there should be a difference between P_λ inside the foveal region and P_λ outside of it. Thus, if the missing retinal layers lead to less scattering of incoming light, the specular component should be higher in the fovea.

Weale measured two differently sized semi-circular fields. The first one included more than twice of the FAZ and the second one only covered about half the size of the FAZ. Comparing P_λ for these two regions, Weale found that their ratio was always close to one and, therefore, light seems not to be affected differently inside the foveal region. This result suggested that the missing retinal tissue inside the fovea does not reduce light scattering which, therefore, would suggest it does not directly improve the visual acuity.

Weale concluded that if retinal tissue does not impact the quality of vision, it might be the retinal blood supply that affects the vision negatively. Therefore, the FAZ is the central reason for superior vision inside the foveal area. If this is the case, the argument needs to be turned around, and the removal of retinal layers from the foveal region is a necessity that ensures that retinal cells for neural processing of information are provided with nutrition despite the lack of retinal blood supply in this area. Weale's conclusion is, therefore, a different one from those we have seen so far as it does not claim that the fovea itself has a function. The fovea is merely a consequence of the missing blood supply in the central region.

A different standpoint was taken 12 years later by Harkness and Bennet-Clark [28] who returned to the view that the shape of the fovea is the reason for its function. They investigated deep foveae and regarded them as a focus[4] indicator that provides the eye with "unambiguous information on focus error" [28]. As others too, Harkness and Bennet-Clark relied on the refraction of light at the retinal boundary inside the fovea. However, they

---

4 Here, *to focus* means to accommodate the lens of the eye to achieve a sharp image.

suggest that especially in convexiclivate foveae this refraction will only affect a tiny portion of the image and does not magnify the image to a degree that is relevant for an improvement of vision. Nevertheless, the introduced distortion at the bottom of deep foveae can be used to estimate as to when the projected image is in focus, i.e. the viewed object is sharp and not blurred.

In their model, the refraction is larger in convexiclivate than in concaviclivate foveae. This difference, however, can be explained acknowledging that deep, funnel-like foveae are often correlated with monocularity. Hunting birds, for instance, use their central fovea to observe each side independently and have two separate images that are not joined into one. A correct focus does, therefore, only depend on the information from one eye. Humans on the other hand, possessing binocular vision, do not depend on the fovea to estimate object distances because such can be reconstructed from the difference of the two images provided by both eyes. Therefore, binocularity provides additional information for the eye to focus and this might be a reason why those eyes often present with shallow foveae.

Around the time of the work of the previous paragraph, Snyder and Miller [29] published the theory of the "Telephoto lens system of falconiform eyes". This work used the old assumption of Walls that light is refracted by the fovea to provide an enlarged image on the retina. Opposed to Walls, who claimed that the steep fovea margins are the reason for the enlargement, Snyder concentrated his research on the bottommost portion of the foveal pit which forms a small hemisphere. When this hemisphere acts as a negative lens, the eye might behave like a telephoto lens.

To support the hypothesis, Snyder and Miller compared the anatomical resolving power of falconian eyes with that of humans as these birds possess superior vision, while the dimension of both eye-types is similar. To do so, the foveal inter-cone distance d in various birds was measured and found to be around $2\,\mu m$, while in humans it was found to be around $3\,\mu m$. After estimating the focal length in falcons from the curvature of their retina ($f = 15.6\,mm$) and using $f = 17\,mm$ for humans, the resolving power was calculated with $RP = f/d$.

Employing this calculation, Snyder and Miller found that falconian eyes have a resolving power that is only 1.38 times larger than the resolving power of humans. This finding is different from that published by Fox, Lehmkuhle, and Westendorf [30], who earlier reported the grating detectability to be 2.6 greater compared to humans by employing a two-choice discrimination task and comparing the performance of an American kestrel with a person.

Therefore, Snyder and Miller suggested that the resolving power of the bird's eye is enlarged by the foveal pit, i.e. the bottommost part of the fovea, which acts as a negative lens [29, Figure 1]. The pit will then introduce an additional magnification factor m in the equation $RP = mf/d$ that depends on the dimensions of the pit-hemisphere, its distance to the photoreceptors and the difference in optical density between the vitreous humour and the retinal tissue.

In conclusion, Snyder and Miller found that eagle eyes can detect point objects at a distance 3 to 8 times larger than humans can. However, they admitted that the fovea may additionally act as focus indicator as reported by Harkness and Bennet-Clark [28].

So far, we have reviewed several of the existing hypotheses concerning the function of the fovea in vertebrate eyes. Several other theories have been published which have not been considered since the presented material already shows the diversity of conflicting beliefs. The interested reader

can turn to the work of Maldonado, Maturana, and Varela [31], Bloch and Martinoya [32], and Steenstrup and Munk [33]. In addition, Locket [34] re-evaluated the light tracings through many deep foveae that were available as histological drawings.

At this point, we must acknowledge that it remains unclear if the refraction of light at the retinal boundary indeed takes place. Recent publications reported that it might be wrong to assume that conventional geometrical optics can be applied at the scale of cells. It was found that retinal cells instead act as optic fibres which in turn would make the premise of Walls and all who followed the same path questionable [35].

All early publications regarding the fovea form have in common that they base their investigation on shapes that have been extracted from ex-vivo samples. An in-vivo assessment of the fovea was not possible without further advances in technology. Therefore, studying the complete three-dimensional fovea shape was as impossible as it was to make continuous measurements of the same eye on the same location to show the development of an ageing fovea. Nevertheless, some attempts have been carried out.

Hendrickson and Yuodelis [36] described the human fovea during development and used samples from different subjects as the analysis had to be done ex-vivo. With an in-vivo imaging method it would be possible to repeat this kind of study on the same subject, eliminating errors that are introduced by using unrelated eyes from different specimens.

O'Leary [37] presented a first approach to tackle this problem by analysing photographs of retinas. These images showed a specific reflection pattern around the fovea which was used to estimate the radius of foveal curvature in living subjects. Although the shape of the fovea could not be assessed, this method analysed the dimension by relying on harmless in-vivo imaging only. Around the time when O'Leary [37] published his work, a technology called optical coherence tomography (OCT) was developed that would open new ways of analysing retinas.

2.3 OPTICAL COHERENCE TOMOGRAPHY

In the past, histological sections were the main resource when investigating form and function of foveae. This approach has several drawbacks. Firstly, the process of preparing sections involves deformations when cutting and handling the samples. While this can be minimised, it cannot be completely eliminated. Therefore, when the form of a fovea is analysed, careful consideration of the histology-introduced errors is necessary. Secondly, using histology is only possible post-mortem ruling out any large study on human eyes over a wide range of ages. Additionally, the analysis of foveal development is not possible within the same patient.

With the introduction of optical coherence tomography (OCT), a technology became available that would eliminate these drawbacks. Introduced as a system for "noninvasive cross-sectional imaging in biological system" [38] it became the standard tool for imaging retinal layers.

OCT works similarly to sonography with the difference that it employs light instead of ultrasound. First, the light is split into a reference beam and a sample beam. While the reference beam is left unaltered, the sample beam penetrates the retinal tissue and is partly transmitted and partly scattered. The reflected light from the tissue is then interferometrically compared to the reference beam, and an output intensity is computed that represents certain optical properties of the tissue. Areas of the tissue that have a higher
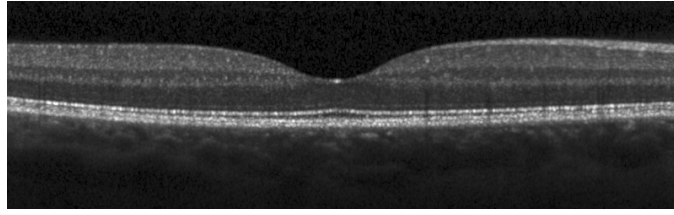
Figure 2.5: OCT B-scan through the fovea acquired with a SPECTRALIS SD-OCT (Heidelberg Engineering). Bright areas indicate tissue with a higher reflectivity.

reflectivity will produce a higher output intensity than areas with lower reflectivity that are translucent to the incoming light. Representing the intensity as a greyscale image can be achieved by displaying the rescaled intensity values as pixels and applying, e.g. a gamma correction to enhance the visibility of retinal layers. In images, higher reflectivity values can either be represented as brighter or as darker areas and both forms can be found in literature. In OCT images of this work, brighter pixels will indicate a higher reflectivity.

Figure 2.5 shows such an image-representation of an OCT. One column in the image corresponds to one depth profile of the scan and is called an *A-scan*. When the position of the depth scan is shifted and measurement is repeated, we get a series of A-scans that is usually referred to as *B-scan* and which can be represented as a greyscale image. To obtain a three-dimensional volume scan, several B-scans that have a certain distance between them are combined so that the surface of the tissue can be sampled in a rectangular area.

In addition to this traditional rectangular volume scan, modern OCTs have several other scanning modes. Two popular ones are:

- a star scan where several B-scans are acquired that run through a fixed position, e.g. the foveal centre

- a ring scan where a B-scan is acquired that samples a circle with fixed scanning radius, e.g. around the optic nerve.

In the last decades since the introduction of the OCT, many advances have been made that go far beyond the scope of this text. For an advanced overview, we refer to the work of Schmitt [39] which provides detailed information about the OCT's mode of operation, interferometry, tissue scattering models and hardware. More recent reviews by Drexler [40] and Drexler and Fujimoto [41] report advances in the field of OCT without going into too much technical detail or physics. Finally, Kiernan, Mieler, and Hariprasad [42] provide an excellent review about commercially available OCT devices which also includes the SPECTRALIS SD-OCT device that was used for acquiring the data used in this work.

Another interesting work in the light of this thesis was published by Wolf-Schnurrbusch et al. [18] because it compares a single measurement repeated with six of the most popular OCT devices. Such a comparison is interesting because when quantifying the shape of the fovea, we are interested in sizes, thicknesses, widths or heights of certain features in *metric units*. As we will see in the discussion, the OCT needs to make certain assumptions about the eye to provide these quantities and different devices use different calculation models. Wolf-Schnurrbusch et al. [18] measured the CFST and reported that OCT devices provided (sometimes significant) differences in such data for the same subjects, which will be presented in the next section.

While the correct conversion to metric units is certainly an important aspect, OCT devices need to account for eye movement or noise reduction as well. Therefore, image processing plays a major role in the data processing pipeline of commercial devices. Gabriele et al. [43] and the references therein provide an insight into these aspects of OCT imaging for eye research.

Summarizing, OCT has become the standard tool for investigations that concern the structure of the retina because it provides a contactless measuring method with high resolution. Major advances in the last years made it possible that volume scans of retinal areas can be acquired and modern image processing enhances the quality even further. Most importantly, since OCT data is instantly available in digital form, modern computers make algorithmically complex analyses feasible.

2.4 CURRENT RESEARCH

As motivated in Section 2.2, insights in the form of the fovea are driven by a search for meaningful explanations about its function. While former analyses had to draw their conclusions from small sets of histological sections, the introduction of OCT provides researchers with the technological ability to analyse larger numbers of retinas in high resolution.

Since around 2005, most of the appearing publications that quantify properties of the fovea use OCT as a provider for data. In this section, we briefly review published work, and we will later compare the reported findings as a comparison to the results of this work.

Wu et al. [44] used an OCT-3 system (Carl Zeiss Meditec) to compare retinal thickness between normal adult eyes and highly myopic eyes. The acquired thickness data was provided by the built-in software of the OCT using the ETDRS grid. They reported a statistically significant difference in retinal thickness between the examined 80 myopic and 40 normal eyes. The myopic eyes had a significantly greater retinal thickness in the foveola and the 1 mm foveal area. It was found that the retinal thickness in the foveola (see Figure 2.3) was 166 μm *vs* 149 μm and the mean thickness inside the 1 mm circle was 199 μm *vs* 188 μm for myopic and normal eyes respectively. However, for the regions outside the 1 mm circle, it was reported that the myopic group had a significantly smaller retinal thickness and macular volume.

A similar study with 50 subjects was done by Grover et al. [45] who reported retinal thicknesses for all the nine subfields of the ETDRS grid. Most notably, they reported a CRT_{min} of 227.3 ± 23.2 μm and a CFST of 270.2 ± 22.5 μm which is notably larger than what was reported by Wu et al. [44] [5] which may be due to the different device employed (SPECTRALIS SD-OCT (Heidelberg Engineering)).

In a following publication, Grover et al. assessed also the retinal thickness, but presented a comparison between two different OCT devices [16]. The CRT_{min} and CFST measured with the SPECTRALIS SD-OCT showed a similar value as earlier reported and was found to be 225.1 ± 17.1 μm and 271.4 ± 19.6 μm respectively. This measurement differed significantly from that of the Stratus OCT (Zeiss, Oberkochen, Germany) which showed CRT_{min} and CFST values of 166.9 ± 20.9 μm and 202.3 ± 19.6 μm respectively.

The difference has two main reasons. First, the SPECTRALIS SD-OCT is a Fourier-domain OCT as opposed to the Stratus OCT which works in the time-domain to calculate the depths of tissue reflections. More notably, however,

---

5 The CRT_{min} in this publication was referred to as CPT

the Spectralis SD-OCT included the thickness of Bruch's membrane, a layer below the retinal pigment epithelium (RPE), in the calculation of the overall retinal thickness. In recent versions of the Spectralis SD-OCT software, this issue was corrected and separate segmentations of the RPE and the Bruch's membrane are available.

An even more extended comparison of different OCT devices was published by Wolf-Schnurrbusch et al. [18]. There, the CFST of 20 healthy subjects was assessed with six different OCT devices. Again, the Spectralis SD-OCT was among those that showed the highest retinal thickness with $288 \pm 16\,\mu m$ and $290 \pm 15\,\mu m$ for the right and left eye respectively.

Chui et al. reported findings about the relationship of the FAZ and the foveal pit morphology [11, 46]. Ooto et al. [47] investigated the retinal thickness in Japanese eyes and later [47] described race- and sex-related differences in retinal thickness and foveal pit morphology. Tick et al. [48] reported foveal characteristics of 57 healthy subjects to investigate the variability of shapes in a normal population and Yanni et al. [49] examined correlation between the FAZ and the foveal pit in 24 preterm and 34 full-term children.

All publications discussed so far did not employ mathematical models of the fovea to assess their measurements. Rather, they relied on built-in software of the OCT devices for the reported data. However, in comparison to the results presented here, they are nevertheless of interest.

To the knowledge of the author, the first notable approach to extract foveal features using a mathematical model that can be fitted onto different datasets was published by Dubis, McAllister, and Carroll [50]. By reducing the measured OCT data to a small set of model-parameters, the extraction of fovea characteristics can be broken down to the pure analysis of the model function.

Dubis, McAllister, and Carroll [50] employed a difference of Gaussians (DOG) function to represent the foveal pit and used this model to extract foveal properties. However, the DOG is a symmetric function and cannot cope with the fact that foveae are generally asymmetric, mainly due to the thickness of the NFL which is not constant for different anatomical directions. Additionally, regarding the wide range of foveal shapes including specimens with broad bottom but steep rim occurring in some higher primates, or very narrow and steep foveae observable in birds, the DOG method cannot comprise these variations with acceptable accuracy.

Due to their analysis that went far beyond what commercial OCT software could provide, Dubis, McAllister, and Carroll where able to quantify foveal pit depth, foveal diameter and foveal slope. For the two OCT devices and different subject groups the following values where reported: foveal pit depth in the range of $110.7\,\mu m$ to $122.53\,\mu m$, foveal diameter in the range of $1.905\,mm$ to $2.078\,mm$, and foveal slope in the range of $10.407°$ to $12.241°$.

Three years later, Dubis et al. [51] used their model to examine the relationship between foveal pit morphology and the FAZ. Beside the high variation in pit morphology and FAZ for the 42 subjects, they reported a significant correlation between the foveal pit properties and FAZ. The same model was then used to investigate in race- and sex-related differences in retinal thickness, foveal depth, diameter and slope [52].

Barak, Sherman, and Schaal [53] employed an automated regression software (Eureqa, Cornell Creative Machines Lab) to identify underlying equations of subjects with a premacular hole formation in comparison to a control group. Their approach is somewhat different as it does not employ a fixed model of the foveal region. Instead, it identifies formulas found by the

software and calculates foveal characteristics from these findings. Barak, Sherman, and Schaal reported that both compared groups followed polynomials that mainly consisted of trigonometric functions. A similar approach with the same software was presented by Nesmith et al. [54] who investigated in the influence of age in regard to the foveal morphology.

At this time, the basic method presented here was published [10] which, as we will see soon, introduced not only a flexible, parametric model for the foveal shape, but also developed a distinguished way of modelling radially to allow for capturing asymmetries. Therefore, the ideas herein have already been discussed or were even reused, and the following publications referenced this work accordingly: Nesmith et al. [54], Ding et al. [55], Turpin et al. [56], Liu et al. [57], Sepulveda, Turpin, and Mckendrick [58], Yadav et al. [59], and Karl et al. [60]. Three of the mentioned publications are of particular interest as they also developed models for the foveal shape.

Ding et al. [55] used a two component model that consists of a second-order bivariate polynomial and a zero-mean bivariate Gaussian function to assess differences of parameters in patients with Parkinson disease. The mean parameters of the two groups, i.e. normal eyes *vs.* eyes of patients with Parkinson disease, were used as a classification-criterion. It was reported that a single model parameter discriminated 70 % from the control group, while using seven parameters increased the correctness to 76 %.

Liu et al. [57] developed a Sloped Piecemeal Gaussian (SPG) model that can account for a larger number of known foveal pit variations and tested it on 3488 macular scans from both eyes of 581 young adults. The SPG model is a Gaussian function that is pulled apart in its centre and connected with a straight line. This approach was chosen to account for foveal pits with a flat bottom which a normal Gaussian cannot account for. To incorporate asymmetry, a sloped line was added to the final function. Liu et al. presented an extensive comparison between their model and existing DOG, Gaussian and sloped Gaussian models. In relation to the method presented in this work, one should note that we will model both sides of a fovea shape with two unrelated functions that naturally connect at the centre. Since the model developed here will have four parameters for each side, this will increase the numbers of parameters from six (SPG) to eight, but it does not assume that the asymmetric relation purely depends on a linear difference in height introduced by a sloped line.

Yadav et al. [59] extended the radial modelling approach we will present here and used a cubic Bézier polynomial as model function. Using Bézier polynomials allows for a greater flexibility and their model was claimed to be more accessible to an analytic investigation to, e.g. calculating the volume of the foveal pit. We will show here that the analytic calculations necessary for the foveal pit volume, i.e. calculating the antiderivative of the model function, are indeed possible and that the resulting formulas can be expressed concisely. Finally, Yadav et al. compared the performance of their model with the models of Dubis, McAllister, and Carroll [50] and Ding et al. [55]. Unfortunately, the method presented here was not included in the comparison.

2.5 SUMMARY

In the previous sections, we motivated the scientific interest in the fovea by presenting important publications of the last century which discussed different explanations for the existence of the foveal pit inside the retina.

Starting from the assumption that the fovea's purpose is to remove tissue from the light-path, researchers suggested it might lead to a magnification by the refraction on either the foveal boundaries [2] or the pointy pit in birds of prey that act like a telephoto-lens [29]. It was hypothesized that the fovea is a focus indicator to track small objects [22] or a device to help a monocular lens to find the correct focus to achieve a sharp image [28]. For the human fovea in particular, another work suggested that the fovea is only a result of the FAZ as otherwise nutrition and oxygen cannot be provided to an area that can, for optical reason, not be crossed by blood-vessels [26]. Moore et al. [61] provide an exceptionally detailed report about the topic and they carefully addressed existing hypotheses of the fovea's function. However, their conclusion clearly highlights why the fovea is to this day an important research topic:

> Consequently, little is known about the functional properties of retinal specializations in different vertebrate taxa. This has limited our understanding of the diversity of strategies animals use to gather visual information from different environments, and it has slowed our progress in mapping the functional evolution of vertebrate eyes. By focusing future research efforts on testing these functional hypotheses, we will be able to better comprehend the relationship between the eye and the physical environment, and ultimately the visual ecology of vertebrates. (Moore et al. [61])

Today, researchers are more careful with new hypotheses and they rather concentrate on building a rigorous foundation of the fovea morphology. We have shown several publications that reported retinal measurements of the foveal area, many of which employed recent OCT technology [11, 18, 44–47]. These publications are vital as a database of reference values of retinal properties inside the fovea, but they did not capture the exact morphology of the fovea.

With the introduction of foveal modelling, researchers were firstly able to describe foveal shapes in mathematical terms. The models can be classified into two groups: free-form models that try to find a mathematical formula for the shape (e.g. [53]) and parametric models that fit parameters of a fixed formula. The latter are of particular interest because parametric models need to be designed carefully to be as flexible as necessary and as restricted as possible [62]. Early models were insufficient to represent the asymmetric nature of the fovea (e.g. [50]) which was accounted for by introducing additional terms or using a more general formula (e.g. [59, 63]).

The work we present here will employ a model function that was designed to represent most appearing foveal shapes. Nevertheless, its formula is comparably simple as it only represents one foveal shape starting from the centre of the fovea. The flexibility is achieved by the way the model is incorporated into a radial fitting procedure to allow for the modelling of a complete, three-dimensional, and possibly asymmetric fovea.

PARAMETRIC FOVEA MODEL

As already discussed in Section 2.4, common choices to model foveal pits include Gaussian functions or difference of Gaussians (DOG) that are sometimes combined with a slope term to account for asymmetries. They are well understood and their mathematical nature make them easily accessible.

Starting from the second derivative of a Gaussian, it becomes apparent that such functions already resemble major characteristics of a fovea:

$$\mathcal{G}(r) = \partial_{rr} \exp\left(-r^2/2\right) = r^2 \exp\left(-r^2/2\right) - \exp\left(-r^2/2\right). \tag{3.1}$$

Figure 3.1a shows that the graph of $\mathcal{G}$ and the inner limiting membrane (ILM) share similarities that make $\mathcal{G}$ an excellent candidate for developing a fovea model. For one, the graph of $\mathcal{G}$ has a smooth pit at the origin where it has its minimum. From the centre, the height of $\mathcal{G}$ increases until it reaches a maximum before it finally converges to a constant value. These features correlate to the foveal bowl, rim and the flattening of the thickness outside the rim.

However, to turn $\mathcal{G}$ into a flexible model for foveae, certain model parameters need to be introduced to allow for an adaption on the vast number of possible foveal shapes. Before we go into detail, some properties and requirements of the final model need to be motivated.

(a)   **(b)**
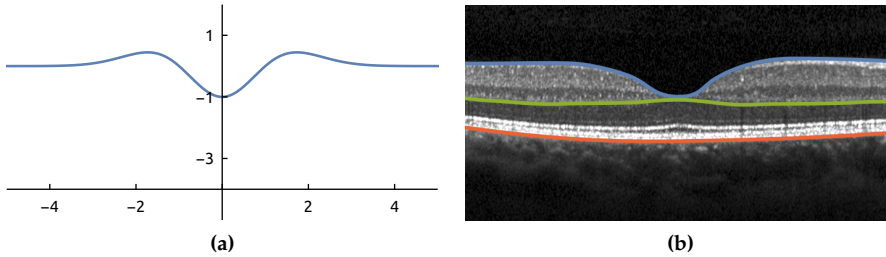
Figure 3.1: Comparison of the function $\mathcal{G}(r)$ from Equation 3.1 in (a) and an OCT through the foveal region in (b). Coloured lines denote the ILM boundary (blue), the ONL boundary (green) and the RPE boundary (red). Retinal thickness is considered to be the distance between ILM and RPE.

3.1 MODEL PROPERTIES AND REQUIREMENTS

3.1.1 *Modelling relative to the RPE boundary*

Modelling the height of the foveal shape requires an appropriate reference coordinate system. Although not explicitly stated, Figure 3.1a suggests that

this reference line is the arbitrarily chosen x-axis[1], but when data is extracted from an OCT, the position of the retina depends on the particular scan and image coordinates vary drastically.

Employing image coordinates in the modelling procedure would inherit several drawbacks. Unlike Figure 3.1b, retinal scans acquired in clinical routine are often slightly tilted, and the retina is rarely aligned horizontally in the centre of the image. These artefacts are inherent to the measuring procedure and even experienced operators cannot prevent them. Additionally, the absolute horizontal position of the retina is not constant. Although the operator ensures that the scan of the retina is indeed inside the image, the exact y-position may vary. Therefore, using image coordinates, e.g. measure from the bottom of the image, to refer to positions on the retina is a poor choice.

Another reason against the bottom of the image as reference is the eye itself, which is a spherical structure. Its rounding is visible in the OCT and we would have to take care of the addition in height at points far from the centre. Note that the RPE in Figure 3.1b is significantly higher at the left and right image border.

Finally, we cannot neglect the importance of the retinal thickness in modelling foveal shapes. Thus, the shapes of two foveae might be similar even when the thickness of the retina beneath them is different. But both the shape and the retinal thickness is important for future analyses.

Therefore, instead of using image coordinates directly, we are using the retinal thickness, defined by the height difference between ILM and RPE, as an appropriate choice in the modelling procedure. It will make the modelling independent of the absolute position of the retina inside the OCT and will account for cases where the scan is not aligned parallel to the bottom of the image.

To calculate the correct distance between a point on the RPE and its corresponding point on the ILM above, we would have to determine the normal direction[2]. This, however, is impractical as it requires a smooth RPE which cannot be ensured for all retinas and might lead to unexpected results in the thickness calculation. Since we expect a certain quality from the OCT scans and since the visible curvature of the eye inside the scan is small, deviation angles of the RPE are expected to be small as well. Therefore, using the vertical distance between RPE and ILM is a valid approximation for the thickness of the retina. This approach was already used by others (e.g. [50, 51]), and for a whole OCT scan, we will refer to it as *retinal thickness map*.

3.1.2   *Radial modelling with a one-sided model*

The foveal pit is an asymmetric, often elliptical structure as the cited publications in Section 2.4 reported. One primary reason for that is that the pit of a completely developed human fovea lacks of inner retinal layers which includes the nerve fibre layer (NFL) that is responsible for relaying signals from the photoreceptors. However, information from all photoreceptors inside the retina need some path to the optic disc where the eye has its neural connection to the brain or they would otherwise be useless.

In a fovea-free retina, a neural path from all positions to the optic disc can be achieved by a radial path pattern with the optic disk in its centre.

---

1 Note that this general form of $\mathcal{G}$ has a value of -1 in the centre and is almost 0 at both ends. The x-axis in the figure has a height of $y = -4$.
2 i.e. the direction vertical to the RPE surface on each point of the RPE
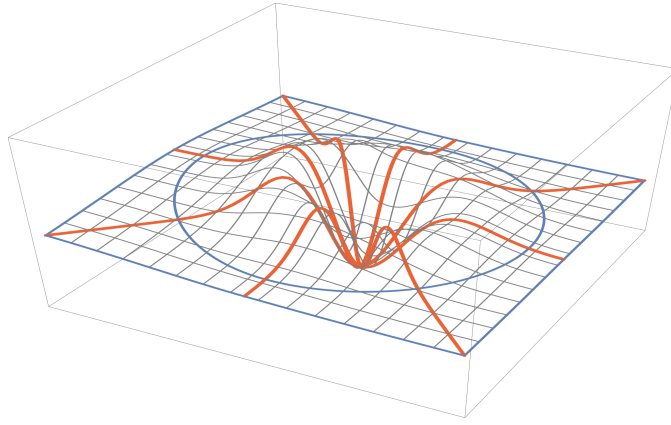
Figure 3.2: Visualisation of the radial modelling approach for eight fitted foveal shapes. Each red line represents one particular foveal shape starting from the centre and going outwards. The blue circle indicates the boundary of the fitted region. The surface, as indicated by the grey grid, is reconstructed by interpolating the foveal shapes.

Since neural paths do not cross the foveal zone, such a direct connection is impossible and all paths through the fovea need to bypass this area. This increases the thickness of the NFL around the fovea asymmetrically because on the nasal side (the side of the fovea where the optic disc resides), more nerve fibres are bundled than on the opposite, temporal side. In fact, in the OCT image in Figure 3.1b this is visible by the thickened bright NFL layer on the right side below the blue line.

Therefore, an approach to model the three-dimensional structure of a fovea needs to take into account that foveal shapes will be distinct for different directions from the foveal centre. Some existing publications have solved this by using symmetric formulas to model a complete section through the foveal centre and introducing an additional slope term in the model (see [57] and the references therein) to account for such differences.

However, using a one-sided model and representing the two opposite sides of a fovea separately has the advantage that it is possible to compare the model parameters for both sides and draw conclusions from their difference. Generalising this idea further, one can model not only two opposite sides from one B-scan but applying the approach in several directions from the foveal centre. This naturally leads to a method that is capable of modelling the complete three-dimensional structure of a fovea around its centre.

Therefore, in this work we use a radial scheme, which fits several directions independently with a model that represents only one side of the fovea. A visualisation of this method is given in Figure 3.2, which shows the reconstruction of a foveal surface by using eight different modelling directions. Each red shape starts in the centre of the fovea and models the structure in one particular direction.

The radial approach has the following advantages:

1. Each direction is represented by a simple one-dimensional model function that can be examined and characterised analytically.

2. When every direction is modelled independently, it is possible to account for asymmetries of the three-dimensional structure of the fovea.

3. The resolution of this radial representation can be increased arbitrarily by increasing the number of modelled directions.

4. Fitting independent directions with a simple one-dimensional model can be done in parallel which might have superior performance than modelling the complete foveal surface with a mathematically complex formula.

3.1.3 *Coordinate system of the model*

Using the distance between ILM and RPE as explained in Section 3.1.1 leads to a coordinate system where the model function has a value of minimal central retinal thickness in the fovea (CRT_{min}) in the foveal centre. However, when modelling different directions of a fovea, the value of CRT_{min} is an additive constant that is the same for each direction. Therefore, this component should not be a part of the model, and the fovea model itself will only include parameters necessary for representing the shape, using the bottom of the foveal pit as origin of the coordinate system as shown in Figure 3.3.

3.1.4 *Simplicity of the model formula*

In general, the goal is to find the smallest possible model that is able to represent important properties of the data. While we wish to represent a large variety of foveal shapes, a model with many free parameters is often overly complex and can sometimes be led astray [62].

Additionally, the model equation we seek should aim to exhibit two features: A certain *mathematical accessibility* and a *human accessibility*. The human accessibility is certainly optional but it would add considerable value and assert that parameters can be *intuitively understood* in a similar way that one understands the influence of the parameters μ and σ of a normal distribution.

Mathematical accessibility is the ability to analyse the model function without numerical values for the free parameters. In later analyses, we will calculate foveal characteristics like steepness of the fovea wall or height of the foveal rim that will include finding antiderivatives and derivatives of model-based formulas. With a mathematically challenging model equation, one might be left with numerical schemes to find solutions for these problems.

However, when it is possible to obtain results for unknown parameter values, i.e. solve them *symbolically*, general conclusions can be drawn about valid ranges for parameter values and the properties of the model itself. Finally, with an analytic solution to fovea characteristics, the numerical calculation for specific parameter values turns into a trivial substitution of numbers.

3.2   MODEL EQUATION

The fundamental form of Equation 3.1 already shows typical shape features required for real foveae, however, it is a symmetric formula, i.e. $\mathcal{G}(r) = \mathcal{G}(-r)$. Since the goal is to model foveae which are asymmetric, only the right half with $r \geq 0$ is used.
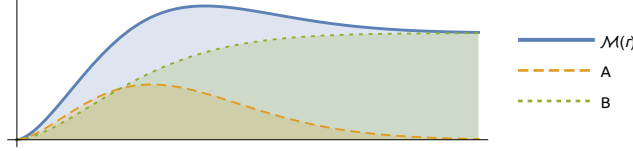
Figure 3.3: The model $\mathcal{M}(r)$ as sum of terms A and B.

To extend Equation 3.1 into a flexible model, four parameters, namely μ, σ, γ and α are introduced. The final form of the radial model is given by

$$\mathcal{M}(r; \mu, \sigma, \gamma, \alpha) = \underbrace{\mu\sigma^2 r^\gamma \cdot \exp\left[-\mu r^\gamma\right]}_{A} + \underbrace{\alpha\left(1 - \exp\left[-\mu r^\gamma\right]\right)}_{B}. \tag{3.2}$$

Like the derivative of the Gaussian, Equation 3.2 consists of two additive terms A and B, which are depicted separately in Figure 3.3 to facilitate a deeper insight into the structure. In general, the first term A mainly controls the form of the foveal rim, and term B mainly influences the thickness outside the foveal pit. Both terms contribute to the width and steepness of the foveal pit, since the controlling parameters μ and γ appear in A as well as in B. To gain a complete understanding on how the parameters influence the shape, the following sections provide a detailed examination of their behaviour and properties.

3.2.1 *Parameter σ, the height of the rim*
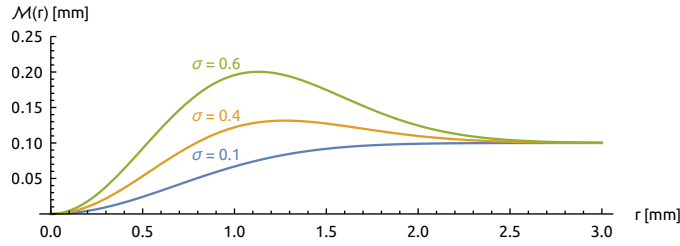
Figure 3.4: Influence of parameter σ onto the shape of the model.

The dashed orange line in Figure 3.3 represents term A of the model equation. This term forms the rim of the fovea and its height is proportional to the square of σ and, therefore, a fovea with a prominent rim will have a larger σ-value than a fovea without one. Since this parameter does not appear in term B of $\mathcal{M}$, it has only marginal influence on the shape of the fovea outside the rim region.

3.2.2 *Parameter α, the retinal thickness outside the foveal pit*

The parameter α, only present in term B, controls the height of the monotonically increasing function which is displayed as dotted green line in Figure 3.3. Since we assume a constant retinal thickness outside the foveal area, the model function has to converge to a specific value. Therefore, α was introduced to influence term B in such a way that the model converges to the value of α as $r \to \infty$.
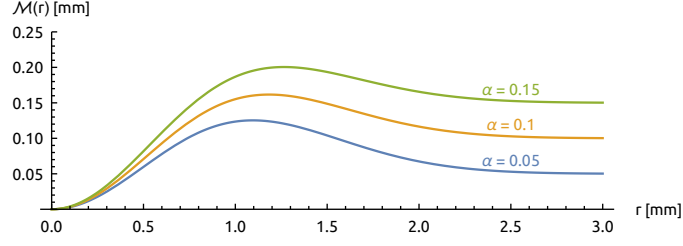
Figure 3.5: Influence of parameter α onto the shape of the model.

Lemma 1. *Given $r \in \mathbb{R} > 0$ and $\mu, \sigma, \gamma, \alpha \in \mathbb{R}$ and $\mu > 0$, $\sigma > 0$, and $\gamma > 1$ (we will refer to these conditions as* usual parameter restrictions *for μ, σ, γ, and α from now on), then*

$$\lim_{r \to \infty} \mathcal{M}(r; \mu, \sigma, \gamma, \alpha) = \alpha .$$

Proof. First, we will show that term A of Equation 3.2 vanishes as $r \to \infty$. Given the parameter restrictions, then $k = \mu r^\gamma > 0$ and proportional to r. Substituting k into term A, it suffices to see that

$$\lim_{k \to \infty} \sigma^2 \frac{k}{\exp[k]} = \lim_{k \to \infty} \sigma^2 \frac{k}{1 + k + k^2/2 + \dots} = 0.$$

As for term B, we have

$$\lim_{r \to \infty} \alpha \left(1 - \exp[-\mu r^\gamma]\right) = \lim_{r \to \infty} \alpha - \underbrace{\frac{\alpha}{\exp[\mu r^\gamma]}}_{=0} = \alpha.$$

$\square$

It can therefore be concluded that the retinal thickness outside the foveal region can be approximated by adding up α and the difference of ILM and RPE in the foveal centre, which is denoted by CRT$_{min}$.

Note that certain foveae might present a large CRT$_{min}$ and that the fovea centre can have a larger thickness than the surrounding retina. For those cases, α can be negative because the retinal thickness outside the fovea drops below the level of CRT$_{min}$.

3.2.3 *Parameter μ, the width of the foveal pit*

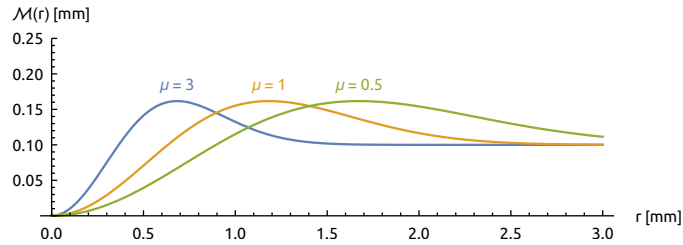

Figure 3.6: Influence of parameter μ onto the shape of the model.

To steer the width of the foveal pit, parameter μ was introduced. Unlike the usual mean of a Gaussian function, where μ is an additive parameter and therefore laterally shifts the whole function, here, μ is a *factor* of r inside the exponential. Therefore, it rather acts like a scaling of the function in

r-direction, and while μ still has the effect of shifting the rim, it also provides the important advantage of keeping the minimum of the foveal pit at $r = 0$. This property is crucial for the approach of radial modelling, since it ensures that two or more models naturally join at the centre.

Another occurrence of μ acts as factor in front of the term A in $\mathcal{M}$. It ensures that μ has no influence on the height of the rim. Before we prove this, we first show that for $\mu > 0$ there exists one defined maximum of $\mathcal{M}$ on the rim.

Lemma 2. *Given the usual parameter restrictions, $\mu > 0$, and $\alpha + \sigma^2 > 0$, the model $\mathcal{M}$ has one defined maximum at*

$$r_{\text{rim}} = \left(\frac{\alpha + \sigma^2}{\mu \sigma^2} \right)^{\frac{1}{\gamma}} .$$

Proof. We will show the existence of the maximum by calculating the first derivative and solving for its roots. A detailed calculation of $\partial_r \mathcal{M}$ is given in Section A.1.

$$0 = \partial_r \mathcal{M}(r) \tag{3.3}$$
$$= \gamma \mu \exp\left(-\mu r^\gamma\right) r^{\gamma - 1} \left(\alpha + \sigma^2 \left(1 - \mu r^\gamma\right) \right) . \tag{3.4}$$

For this product, the first term gives the trivial solution $r = 0$ which we are not interested in. The last factor is linear in r^γ and solving

$$0 = \alpha + \sigma^2 \left(1 - \mu r^\gamma\right)$$

leads to the proposed form of r_{rim}. To show that r_{rim} is indeed a maximum, we will substitute this solution into the second derivative and show that

$$\partial_{r^2} \mathcal{M}(r) \big|_{r = r_{\text{rim}}} < 0.$$

Details of the calculation of the second derivative can be found in Section A.2. After substituting r_{rim} and simplifying the expression, we get

$$\partial_{r^2} \mathcal{M}(r) \big|_{r = r_{\text{rim}}} = -\gamma^2 \mu \left(\alpha + \sigma^2 \right) \exp\left(-\frac{\alpha}{\sigma^2} - 1 \right) \left(\frac{\alpha + \sigma^2}{\mu \sigma^2} \right)^{\frac{\gamma - 2}{\gamma}} .$$

Now, given $\mu, \sigma > 0$, $\gamma > 1$, and $\alpha + \sigma^2 > 0$, we see that all factors of the above equation are positive. Therefore, the whole expression is negative which indicates that r_{rim} is indeed a maximum. $\square$

After calculating the position of the foveal rim, we can analyse if the height of the rim is constant when μ changes. This property is not as much important for an automated analysis as it is for human inspection of model parameters. If the rim height is indeed constant, then we can conclude that two foveae that have similar values in σ, γ, and α and only differ in μ have similar rim thicknesses, but the foveal pit has a different width.

Lemma 3. *The choice of the rim position μ has no influence on retinal thickness at r_{rim}.*

Proof. With r_{rim} from Lemma 2 given, we show that

$$\partial_\mu \mathcal{M}(r; \mu, \sigma, \gamma, \alpha) \big|_{r = r_{\text{rim}}} = 0.$$

First, we calculate the partial derivative $\partial_\mu \mathcal{M}$, where the substitution $k = r^\gamma$ is used to simplify terms
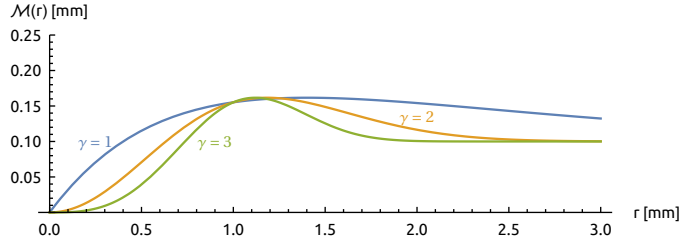
$$
\begin{aligned}
\partial_\mu \mathcal{M} &= \partial_\mu \left(\mu \sigma^2 k \exp[-k\mu] + \alpha \left(1 - \exp[-k\mu] \right) \right) \\
&= \sigma^2 k \exp[-k\mu] - \mu \sigma^2 k^2 \exp[-k\mu] + \alpha k \exp[-k\mu] \\
&= \exp[-k\mu] \left(\sigma^2 k - \mu \sigma^2 k^2 + \alpha k \right) \\
&= \exp[-k\mu] \left(-\mu \sigma^2 k + \sigma^2 + \alpha \right) k
\end{aligned}
$$

Re-substituting the solution $k = (\alpha + \sigma^2)/(\mu \sigma^2)$ from Lemma 2 will make the second factor and, therefore, the whole product zero:

$$
-\mu \sigma^2 \frac{\alpha + \sigma^2}{\mu \sigma^2} + \sigma^2 + \alpha = -\alpha - \sigma^2 + \sigma^2 + \alpha = 0.
$$

$\square$

3.2.4   *Parameter γ, the pit shape*

Figure 3.7: Influence of parameter γ onto the shape of the model.

The parameter γ is an exponent of r and influences the curvature of the foveal pit. It was introduced to allow the model to represent convexiclivate as well as concaviclivate shapes. As stated by Walls [19], most humans possess a concaviclivate fovea form. It is characterised by a pit that is shaped like an S between the rim and the centre.

In contrast, some avian species develop a narrow fovea with a very acute pit and no visible bottom in the centre. Figure 3.7 shows three variations with different values for γ. While $\gamma = 2$ and $\gamma = 3$ creates human-like shapes, $\gamma = 1$ shows an acute pit without visible bottom.

The depicted shape for $\gamma = 1$ indicates to have no flat bottom at the centre and reaches the centre at an angle. Thus, in the present work, we assume $\gamma > 1$ to ensure a zero gradient at its centre although the *flat pit* might be narrow for values close to 1. This is consistent with naturally occurring foveae, where the centre of the pit always has a smooth bottom, because infinitely sharp depressions are biologically impossible.

Lemma 4. *Given $\gamma > 1$, the model equation will have a gradient of zero at $r = 0$.*

Proof. The gradient at the centre $\partial_r \mathcal{M}(r)|_{r=0}$ is given by

$$
\alpha 0^{\gamma-1} \gamma \mu \exp\left(-0^\gamma \mu\right) - 0^{2\gamma-1} \gamma \mu^2 \sigma^2 \exp\left(-0^\gamma \mu\right) + 0^{\gamma-1} \gamma \mu \sigma^2 \exp\left(-0^\gamma \mu\right).
$$

Every term of this sum contains either $0^{\gamma-1}$ or $0^{2\gamma-1}$ as factor. Evidently, only for $\gamma > 1$ these become zero and the gradient at $r = 0$ vanishes. $\square$
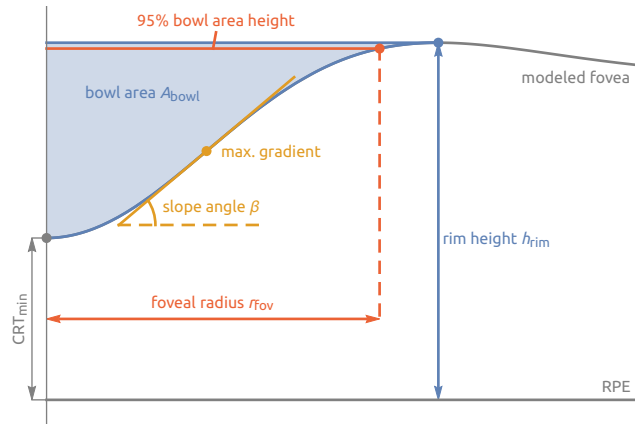
Figure 3.8: Diagram of common foveal characteristics.

3.3 MODEL BASED FOVEA CHARACTERISTICS

When the shape of a fovea is reduced to a few model parameters, there is a clear advantages when analysing properties of the shape. In this section, we want to derive a number of *fovea characteristics* that can be used to describe a fovea and to compare different subjects.

In general, characteristics can be divided into two groups:

1. Characteristics that exist for each modelled direction separately. For instance, the slope angle of the fovea can be evaluated for each direction separately, and we can raise the question if it is different for the anatomical nasal and temporal direction in one subject.

2. Characteristics that exist only once per fovea. The volume of the three-dimensional pit is such a characteristic.

Therefore, on the one hand there are cases where we want to analyse single directions of a fovea, on the other hand there are cases when information from several modelled directions is combined to draw conclusions for the fovea as three-dimensional structure.

Figure 3.8 shows common characteristics for a foveal shape. Some characteristics in this image were already discussed in the publications of Section 2.4 (e.g. CRT_{min} and slope angle) and in the following, we shortly discuss each and present how they can be calculated from the model.

3.3.1 *Minimal central retinal thickness (CRT_{min})*

The CRT_{min} is one of the basic characteristics and is often assessed in studies. In the radial model procedure, it is not directly a part of the model but a property that is extracted upfront as the difference between ILM and RPE at the extracted fovea centre.

Not only for a correct CRT_{min}, but also for the quality of the whole fitting procedure it is crucial to find the precise foveal centre within the OCT volume. Section 4.4 will present a discussion on how the centre can automatically be determined from the data.
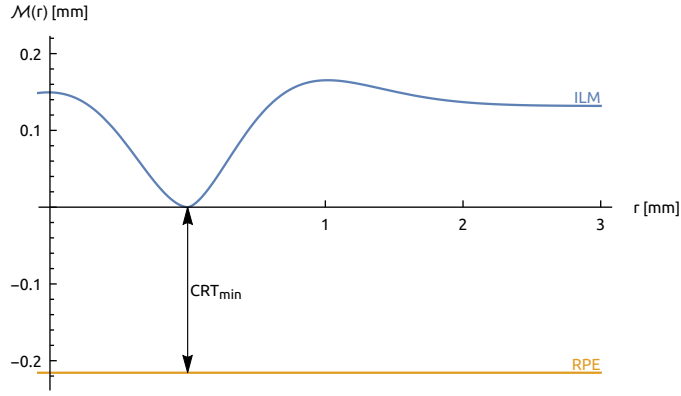
Figure 3.9: Minimal retinal thickness of a fovea.

3.3.2   *Rim height*

The rim height is, as the name suggests, the retinal thickness at r_{rim} and per definition of the model it is the point with the largest retinal thickness. It is depicted in Figure 3.10 and is the sum of the part above the x-axis and the one below it. The height between the RPE and the x-axis is given by CRT_{min} from Section 3.3.1. The part above the x-axis is given by evaluating $\mathcal{M}(r_{\text{rim}})$.
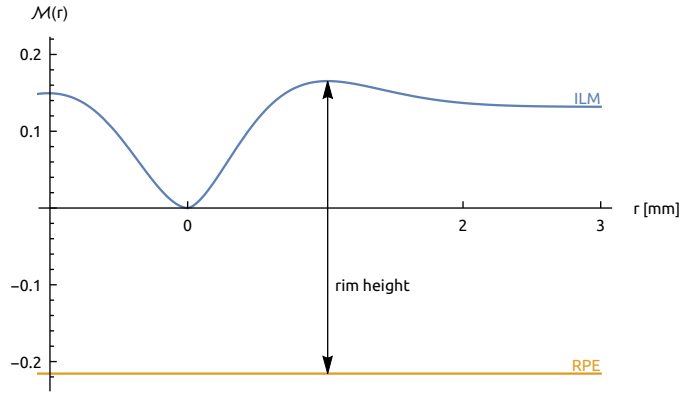
Figure 3.10: The rim height of a fovea.

Lemma 5. *Given the usual parameter restrictions for the model $\mathcal{M}$, the value of the retinal thickness at the rim is*

$$h_{\text{rim}} = \text{CRT}_{\text{min}} + \alpha + \sigma^2 \exp\left(-\frac{\alpha}{\sigma^2} - 1\right).$$

Proof. The concise representation of the above equation can be obtained by using the result for r_{rim} from Lemma 2, calculating $\mathcal{M}(r_{\text{rim}})$ and simplifying the expression taking the parameter restrictions into account. □

Note that the above solution does neither depend on μ nor γ. The absence of μ supports what we have already shown in Lemma 3: the choice of μ has no influence on the retinal thickness at the rim. The missing γ from this solution is unsurprising as well. As already seen in Figure 3.7, γ shapes the parts left and right from the foveal rim and leaves this point unchanged.
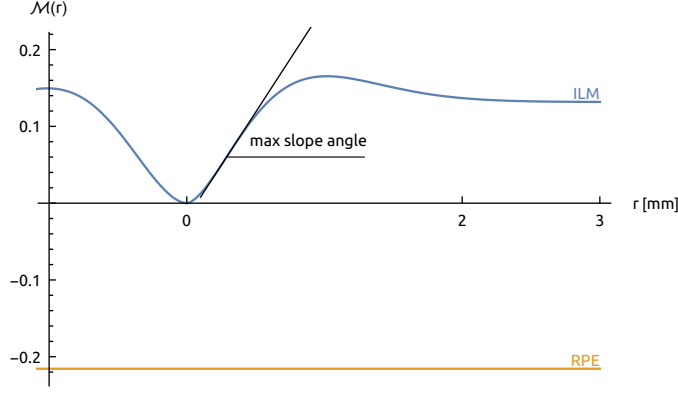
Figure 3.11: Maximum slope of the foveal pit.

3.3.3 *Maximum slope of the pit*

One of the characteristics that are of common interest is the angle of the pit at its steepest point as depicted in Figure 3.11. Since Walls [2] hypothesised that the steepness is correlated to an increase in foveal resolution power, many publications base their assumptions on the difference in foveal slope.

To calculate the point of maximum slope, we need to find the turning point between the origin and the r_{rim}.

Lemma 6. *Given the usual parameter restrictions, Equation 3.2 has 2 turning points of interest, where the first one lies between the foveal centre and the rim and the second one right of the rim. With the substitution $k = r^\gamma$, the 2 turning points can be given in the form*

$$k_{1,2} = \frac{-b \pm \sqrt{b^2 - 4ac}}{2a}$$

with

$$a = \gamma\mu^2\sigma^2, \qquad b = \mu(\sigma^2 - \gamma(\alpha + 3\sigma^2)), \qquad c = (\gamma - 1)(\alpha + \sigma^2).$$

Proof. We show this by solving $\partial_{r^2}\mathcal{M}(r) = 0$

$$0 = \partial_{r^2}\ \mathcal{M}(r)$$
$$= \partial_r\ \left(\gamma\mu r^{\gamma-1}\exp\left(-\mu r^\gamma\right)\left(\alpha + \sigma^2\left(1 - \mu r^\gamma\right)\right)\right)$$
$$= \gamma\mu r^{\gamma-2}\exp\left(-\mu r^\gamma\right)\Big[\alpha\left(\gamma - \gamma\mu r^\gamma - 1\right) +$$
$$\sigma^2\left(\mu r^\gamma + \gamma\left(\mu r^\gamma\left(\mu r^\gamma - 3\right) + 1\right) - 1\right)\Big].$$

We consider that only the last factor of the above product, since the leading term has only the trivial solution $r = 0$. By substituting $k = r^\gamma$ and collecting the coefficients for the different powers of k, we get

$$0 = \gamma\mu^2\sigma^2\,k^2 + \left(-\alpha\gamma\mu - 3\gamma\mu\sigma^2 + \mu\sigma^2\right)k + \alpha\gamma - \alpha + \gamma\sigma^2 - \sigma^2$$

which is a quadratic polynomial in k. Solving this equation leads to the solutions $k_{1,2}$ given above. $\square$
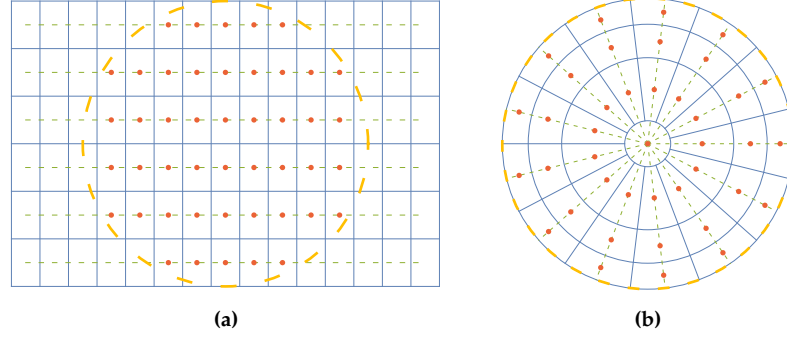
Figure 3.12: Distribution of sampling points to calculate the CFST. Sampling points are depicted as red dots inside a blue grid, dividing the area in equally sized partitions. (a) shows a possible distribution that uses the underlying OCT B-scans, drawn as green, dashed lines. All red sampling points are equally spaced along a B-scan and need to lie inside the 1 mm circle. (b) shows one possible distribution of sampling points that can be used, when retinal thickness is only available on radial model functions (depicted as green, dashed lines). Each small partition surrounded by blue lines has the same area.

3.3.4   *Central foveal subfield thickness (CFST)*

In the literature, it has been common to employ the nine-field Early Treatment Diabetic Retinopathy Study Research Group (ETDRS) grid to examine retinal thickness. The mean thickness in the central circle of the ETDRS grid with a diameter of 1 mm is an important measure and we refer to it as the central foveal subfield thickness (CFST). However, throughout literature, it is sometimes only called central retinal thickness in the fovea (CRT) and the distinction between the *mean* and the *minimal* central retinal thickness is not always evident.

Based on OCT data directly, one way to calculate the CFST is to uniformly distribute a number of sampling points inside the central circle. The CFST is then given by the mean of all retinal thickness values at these sampling points. For OCT data, the most direct approach is to use all A-scans that fall within the 1 mm circle as sampling points.

However, in this work, a fovea is represented by a number of radial model functions centred in the foveola and therefore, a different method is required to approximate uniform sampling. The key idea is, instead of sampling OCT data in x- and y-direction, to use a radial sampling that covers the inner 1 mm circle by varying angles φ and radii r. Since foveae are usually modelled in n_d equally spaced directions, the fixed sampling for φ is given. Along each of the n_d model functions, $\mathcal{M}(r)$ can be evaluated for arbitrary values of r.

To achieve a uniform distribution inside the circle, every sampling point should cover the same area-fraction. As depicted in Figure 3.12a, the built-in CFST of the OCT software tool employs the following paradigm: every sampling point covers a small rectangular area of the same size as indicated by the grey grid lines.

In Figure 3.12b, a different partition of the 1 mm circle is depicted, which shares the property that all areas containing a sampling point have the same size. Additionally, it is easily possible to construct this partition and make all sampling points lie on the green dashed lines that represent the given model functions.

The partition shown in Figure 3.12b can be derived from a recurrence equation to obtain the blue circles that are required to ensure all small sampling areas are of the same size:

- Given the number of modelled directions n_d, the number of different radial sampling points n_r that can be chosen freely, and with one additional central sampling point, the overall number of red points is $n = n_d \cdot n_r + 1$.

- With n given, the area of one small partition can be calculated by dividing the area of the measurement region, $A_{\text{CFST}} = \pi \cdot r_{\text{CFST}}^2$, into n equal partitions by $A_0 = A_{\text{CFST}}/n$. To obtain the usual definition of 1 mm circle CFST, $r_{\text{CFST}} = 1/2\,\text{mm}$. Therefore, the radius r_0 of the central blue circle in Figure 3.12b is given by $r_0^2 = A_0/\pi$.

- The area of the annulus between two adjacent radii r_n and r_{n+1} is given by $n_d \cdot A_0$ since each ring consists of n_d segments that have the same size A_0. Additionally, taking the standard definition of an annulus, its area can be calculated by the difference of two disks with radii r_{n+1} and r_n which leads to the recurrence equation

$$n_d \cdot A_0 = \pi r_{n+1}^2 - \pi r_n^2 \quad \text{with} \quad r_0^2 = A_0/\pi.$$

- By solving the above equation for r_{n+1}^2 and expanding a few of the recursive steps, one finds the explicit solution for the j-th radius to be

$$r_j^2 = r_{\text{CFST}}^2 \left(\frac{j \cdot n_d + 1}{n_d \cdot n_r + 1} \right), \quad j = 0, \ldots, n_r.$$

Note that r_{n_r} is simply r_{CFST} and that sampling points will be placed in the middle between two neighbouring radii.

Given the list of radii r_j, the final approximation of the CFST using the model is given by

$$\text{CFST} = \text{CRT}_{\min} + \frac{1}{n} \sum_{i=1}^{n_d} \sum_{j=0}^{n_r-1} \mathcal{M}_i \left(\frac{r_j + r_{j+1}}{2} \right), \tag{3.5}$$

where $\mathcal{M}_i$ denotes the model function in the i-th direction. Note that this is only one possible numerical approximation of the CFST using radial model functions and that different sampling, interpolating and integrating schemes can be derived as well.

The advantage of the above scheme is that only basic operations like additions, multiplications and powers are required for its computation. The inner sum of Equation 3.5, however, can also be replaced by the analytic result of the proper integral. That is, the volume (or total thickness) of the circular sector that belongs to one modelled direction is calculated symbolically and the CFST is calculated by computing the sum of all sectors divided by the total area.

With n_d modelled directions, every sector spans an angular range of the size $\varphi_d = 2\pi/n_d$. For each modelled direction, the volume under the model-curve $\mathcal{M}_i$ of this sector is given by

$$V_i = \int_0^{r_{\text{CFST}}} \int_0^{\varphi_d} r \cdot \mathcal{M}_i(r) \, \mathrm{d}\varphi \, \mathrm{d}r = \varphi_d \int_0^{r_{\text{CFST}}} r \cdot \mathcal{M}_i(r) \, \mathrm{d}r.$$

Above formula takes into consideration that for the integral in polar coordinates, we must not forget to multiply by r, which is the determinant of the

Jacobian matrix of the coordinate transform. The symbolic solution of V_i is given by

$$
V_i = \frac{\varphi_d \mu_i^{-2/\gamma_i}}{2\gamma_i} \cdot \left[\Gamma\left(\frac{\gamma_i + 2}{\gamma_i}\right) \left(2\sigma_i{}^2 - \alpha_i \gamma_i\right) + \right.
$$
$$
\left. 2\alpha_i \Gamma\left(\frac{2}{\gamma_i}, r_{\text{CFST}}^{\gamma_i} \mu_i\right) - 2\sigma_i{}^2 \Gamma\left(\frac{\gamma_i + 2}{\gamma_i}, r_{\text{CFST}}^{\gamma_i} \mu_i\right) + \alpha_i \gamma_i r_{\text{CFST}}^2 \mu_i^{2/\gamma_i} \right].
$$
$$(3.6)$$

Details about its derivation are presented in Section A.5. Using this result, an analytic approximation of the CFST can then be given by

$$
\text{CFST} = \text{CRT}_{\min} + \frac{1}{\pi \cdot r_{\text{CFST}}^2} \cdot \sum_{i=1}^{n_d} V_i. \tag{3.7}
$$

However, Equation 3.6 for the sector volumes V_i contains the incomplete Gamma-function $\Gamma(a, x)$ which is an integral form that has no analytic solution [64, sec. 6.5.3, p. 81]. Many software frameworks, like the GNU GSL library [65] or Wolfram Mathematica [66], provide implementations of incomplete Gamma functions. Therefore, if special functions are available for computation, the second scheme provides an alternative to calculate the CFST.

3.3.5 Foveal bowl area
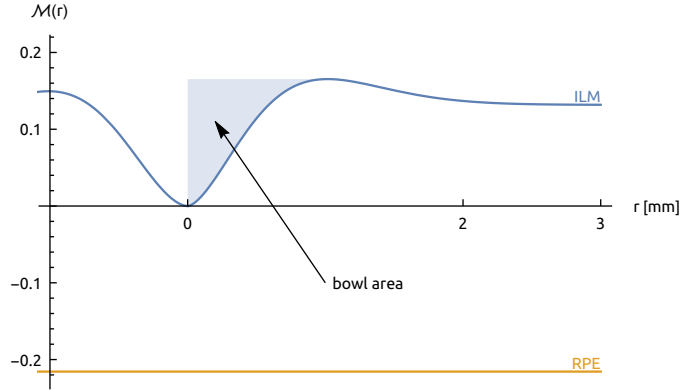
Figure 3.13: Bowl area of the foveal pit.

The *one-sided* bowl area is the blue region depicted in Figure 3.13 and it is defined as the area enclosed by the horizontal line to the highest point on the foveal rim and the model function.

To calculate an analytic formula for this area, the point $(r_{\text{rim}}, \mathcal{M}(r_{\text{rim}}))$ (see Lemma 2) is required. The rectangular area under the horizontal upper boundary line of the foveal bowl is given by the product of r_{rim} and $\mathcal{M}(r_{\text{rim}})$, and, therefore, the bowl area is the difference

$$
A_{\text{bowl}} = r_{\text{rim}} \cdot \mathcal{M}(r_{\text{rim}}) - \int_0^{r_{\text{rim}}} \mathcal{M}(r)dr. \tag{3.8}
$$

Substituting the antiderivative of $\mathcal{M}$ from Section A.4 and the symbolic result for r_{rim} from Lemma 2, the explicit form of Equation 3.8 is given by

$$A_{\text{bowl}} = \frac{1}{\gamma} \mu^{-1/\gamma} \left[\Gamma \left(1 + \frac{1}{\gamma} \right) \left(\alpha\gamma - \sigma^2 \right) + \sigma^2 \Gamma \left(1 + \frac{1}{\gamma}, \frac{\alpha}{\sigma^2} + 1 \right) - \right.$$
$$\left. \alpha\Gamma \left(\frac{1}{\gamma}, \frac{\alpha}{\sigma^2} + 1 \right) + \gamma\sigma^2 \left(\frac{\alpha}{\sigma^2} + 1 \right)^{\frac{1}{\gamma}} \exp \left(-\frac{\alpha}{\sigma^2} - 1 \right) \right], \quad (3.9)$$

where $\Gamma(a, x)$ is again the incomplete Gamma-function.

3.3.6 *Foveal bowl volume*

Opposed to the bowl area, the bowl volume measures the content of the three-dimensional foveal pit. A method for the approximation of the bowl volume was outlined by Yadav [59, 63], who used the difference between a *mean cylinder* and the volume under the model function to approximate the bowl volume. The mean cylinder that is used as a reference for the total volume under the rim disk is calculated from rim points:

$$\bar{r} = \frac{1}{n_d} \sum_{i=1}^{n_d} r_{\text{rim}_i}, \qquad \bar{h} = \frac{1}{n_d} \sum_{i=1}^{n_d} \mathcal{M} \left(r_{\text{rim}_i} \right), \qquad V_t = \pi \cdot \bar{r}^2 \cdot \bar{h}.$$

The total volume under the model with the rim disk as boundary is given by

$$V_r = \frac{2\pi}{n_d} \sum_{i=1}^{n_d} \left(\int_0^{r_{\text{rim}i}} r \cdot \mathcal{M}_i(r) \, dr \right),$$

where a symbolic form of the integral is given in Equation 3.6 when the radius is replaced appropriately. The foveal bowl volume can then be defined as

$$V_p = V_t - V_r. \tag{3.10}$$

The approximation of the foveal bowl volume in Equation 3.10 has already shown its practicability [59], and although Yadav et al. used a spline-based model, it works equivalently for the parametric model here. However, there are peculiarities which demand a further discussion. Intuitively, the concept of a three-dimensional foveal bowl volume can be imagined as filling the inner foveal cup with, e.g. water and measure how much of it fits into the bowl. A rigorous definition, however, is not easily possible since the foveal rim varies in its height and radius.

Figure 3.13 shows this problem when we inspect the left foveal rim that is notably lower than its right counterpart. Therefore, calculating the left and right part of the bowl with Equation 3.8 and adding both areas would lead to incorrect results.

In a two-dimensional section like in Figure 3.13, this problem can be solved by using a line from left to right rim as a boundary which leads to an intuitively sound approximation for the bowl area. For the three-dimensional bowl, however, the situation is ambiguous, because a plane does generally not cover the top part when the rim-heights of different directions vary.

To find a surface that covers the foveal bowl and connects to the complete crest of the rim, a different approach is required. One possible solution could employ a *minimal surface*, which is a surface that locally minimises its area.[3] For a foveal rim of constant height or a rim, that can be covered with a

---

3 Minimal surfaces naturally occur when covering a wire frame with a soap film. Now, assuming a circular shaped wire frame that represents the foveal rim, the soap film would connect to the complete wire frame and create a smooth, minimal surface inside.

plane perfectly, the minimal surface would naturally lead to the same planar solution. For foveae with highly varying rim, a minimal surface would lead to an intuitive cover for the bowl that fits the rim perfectly. Although, the procedure of calculating the foveal bowl volume by this approach and the required error analysis go beyond the scope of this work, we will give an outline of the algorithm.

Using the rim points for all modelled directions as fixed boundary, a minimal surface can be calculated by starting with an initial mesh that connects all rim points and fills the interior. Then, an iterative method is used that transforms the mesh gradually and minimises a certain energy measure. This procedure will eventually converge to a mesh that is the discrete approximation of a minimal surface and details can be found in the work of, e.g. Pinkall and Polthier [67]. This mesh is then used to calculate the volume under surface that has the foveal rim as boundary.

Now, Equation 3.6 is adapted by replacing r_{CFST} with r_{rim} of each sector and the overall volume under the model surface is calculated. Finally, the difference between the volume under the minimal surface and the volume under the model leads to a hopefully more accurate numerical estimate of the foveal bowl volume.

3.3.7 *Foveal radius*

The foveal radius is a measure for the extent of the foveal pit. For this purpose, it seems natural to use the distance between the fovea centre and the highest point on the foveal rim, r_{rim}. However, while most foveal shapes have a clear rim, we observed foveae where the rim is almost even. In such foveae, although they do possess a rim, this point might be located at a significantly greater distance to the foveal centre, compared to a fovea with similar properties but a more pointed rim. That would lead to a foveal radius definition with a high variance, even when the foveal shapes themselves are characteristically similar.

We found that the foveal bowl area, which includes r_{rim} only indirectly as integration boundary, can be used to obtain a consistent measure for the extent of the foveal pit. For this purpose, a defined percentage p (usually 95 %) of the foveal bowl area is introduced. This reduced amount of bowl area can be thought of filling the pit to a slightly lesser degree and reaching r_{rim} not entirely. This leads to the effect that in foveae with an almost even rim that is distant from the centre, the p-percentage radius reflects to a better degree the extent of the visually observable bowl. In Figure 3.8 this is exemplary shown by the red $p = 95$ % line and the distance between foveal centre and the red dot on the fovea shape.

Using the results from Section 3.3.5, the foveal radius r_{fov} can be obtained by solving the following equation

$$r_{\mathrm{fov}} \cdot \mathcal{M}(r_{\mathrm{fov}}) - \int_0^{r_{\mathrm{fov}}} \mathcal{M}(r) dr = p \cdot A_{\mathrm{bowl}}. \tag{3.11}$$

In this work, a numeric scheme was employed to solve Equation 3.11 for r_{fov} which consists of a simple bisection algorithm to find the root. This approach is justified due to the very nature of the expression, because Equation 3.11 will have exactly one solution in the interval $0 < r < r_{\mathrm{rim}}$ when the percentage p is between 0 % and 100 %.

To reconstruct a three-dimensional surface from the obtained parameter sets for different directions, it is necessary to interpolate model parameters. The interpolation of model parameters between two fitted directions φ_1 and φ_2 allows obtaining parameters for arbitrary angles $\varphi_1 < \varphi < \varphi_2$. However, the commonly used polynomial- or spline-interpolants are not optimal for two reasons. Firstly, most interpolation methods tend to *overshoot* in several situations. That means, to ensure a smooth interpolation function, these methods might introduce features that are likely not part of the original dataset. Although, it is unknown how parameters behave in detail in between modelled directions, empirical tests showed that for a sufficiently small angle-range φ_1 and φ_2, the foveal shapes employ a steady transition. Therefore, it is a common assumption to make a smooth, monotonic transition between two values. Secondly, in the fitted circular region, it is required that the angles $\varphi = 0$ and $\varphi = 2\pi$ have the same value and the same derivative. This provides equal smoothness on the 0-to-2π-angle boundary as in the rest of the circular region.

Therefore, parameter-sets of angular directions are interpolated with a monotonic scheme that was introduced by Steffen [68], which was adapted to be periodic to the first-order derivative. For this, one only has to calculate the boundary derivatives by assuming that parameter values were padded periodically.

A comparison that shows the advantage of the periodic Steffen interpolation is given in Figure 3.14 which depicts side-by-side with a non-periodic spline-interpolation of order 3. For this example, the aim is the interpolation of five data points $(1, 6, 7, 2, 3)$ which are repeated periodically. The overshooting of the spline is clearly visible in the ranges 2 to 3, 4 to 5, and 5 to 6. Opposed to that, the Steffen method presents with a monotonic transition between data points. Additionally, the periodic adaption of the Steffen method allows for a smooth transition at data point 6 with continuous first derivative of the interpolating function.
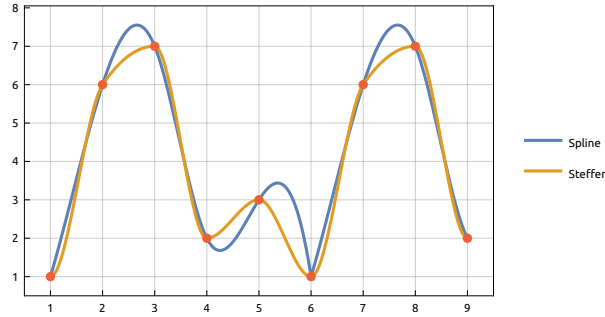
Figure 3.14: Comparison of spline interpolation and periodic Steffen interpolation.

This scheme is used to construct four interpolation functions, where each function represents the angle-dependent course for one parameter. To give an example: with n fitted directions the single $\mu_1, \mu_2, \ldots, \mu_n$ are used to construct the following interpolation function:

$$\tilde{\mu}(\varphi) : [0, 2\pi] \mapsto \mathbb{R}.$$

With the model Equation 3.2, the constructed interpolating functions $\tilde{\mu}, \tilde{\sigma}, \tilde{\gamma}$ and $\tilde{\alpha}$ and the transformation from polar to Cartesian coordinates, the final fovea surface can be given as

$$\mathcal{F}(x,y) = \tilde{\mu}(\varphi)\tilde{\sigma}(\varphi)^2 \left(x^2 + y^2\right)^{\tilde{\gamma}(\varphi)/2} \exp\left[-\tilde{\mu}(\varphi)\left(x^2 + y^2\right)^{\tilde{\gamma}(\varphi)/2}\right] +$$

$$\tilde{\alpha}(\varphi)\left(1 - \exp\left[-\tilde{\mu}(\varphi)\left(x^2 + y^2\right)^{\tilde{\gamma}(\varphi)/2}\right]\right)$$

$$\text{with } \varphi = \text{atan2}(y, x). \quad (3.12)$$

The `atan2` function in Equation 3.12 denotes the arc tangents of y/x that takes into account which quadrant the point (x, y) is in. Both Figure 3.2 and Figure 3.15 were created using the formula above. While the visualisation of $\mathcal{F}$ is surely very descriptive, the main application of the surface reconstruction is the computation of foveal characteristics for the whole angular interval.
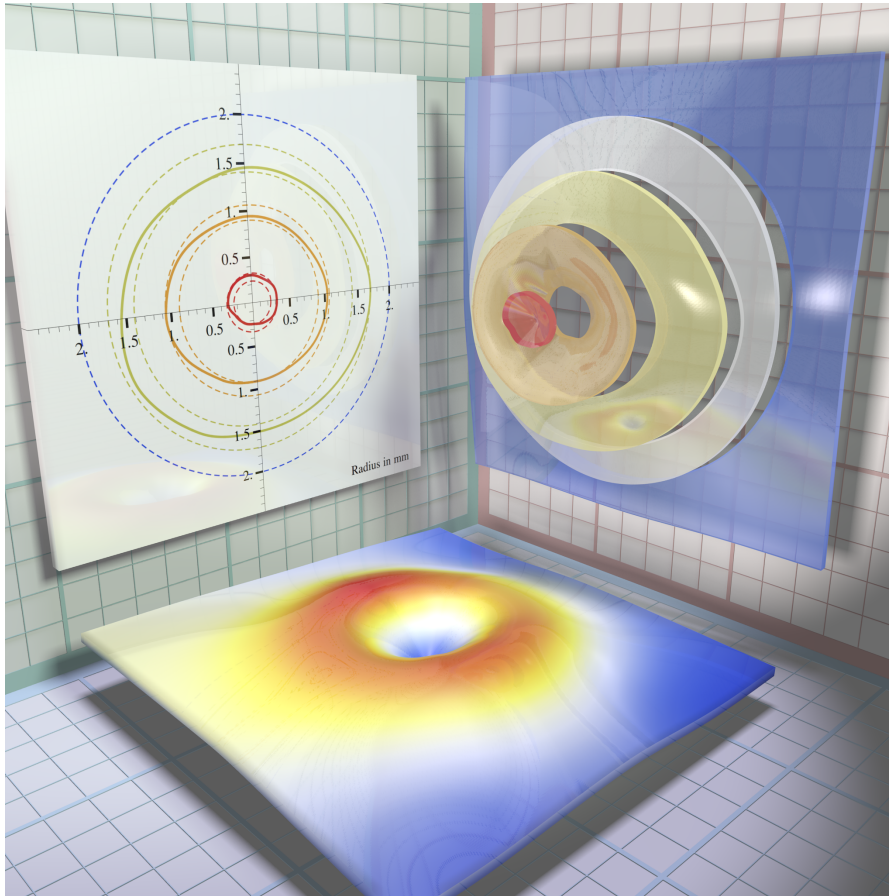
Figure 3.15: Visualisation of a reconstructed foveal surface of a left eye. The three graphs correspond to each other in a way that the back left edge of the bottom surface is the top edge of both upper graphs (in the retina this corresponds to the superior position). In the bottom figure the full foveal surface with its different heights is illustrated. The upper right illustration is an exploded view which shows the fovea as if it were cut along important characteristic points. These are from inside out: first inflection point, rim maximum line, second inflection point and maximum fitting radius. The upper left part shows a projection of the foveal region boundaries, where it becomes visible that the different radii, in fact, are varying and the foveal structure is asymmetric. While in the bottom figure different heights are colour-coded (red depicts the highest elevations), the top two figures utilise colours to separate different regions, whereby the colourings in left and right upper graphs correspond to each other. The front left part of the bottom surface corresponds to the nasal region of the fovea. This is clearly indicated by a higher elevation (coded in yellow) which is caused by thickening of the nerve fibre layer towards the optic nerve head.

IMPLEMENTATION

While the last chapter covered mathematics and theoretical details of the fovea model and its characteristics, the purpose of this chapter is to present computational details required to implement the procedure. In particular, we will demonstrate details of the employed algorithms backed by code examples to ensure that the work can be reproduced or re-implemented in a different language.

All code in this chapter was tested on an Intel Core i7-5960X CPU with 3.00 GHz and 64 GB RAM running Ubuntu 16.04. *Mathematica* (Wolfram Research, Inc., Version 11.3, Champain, IL (2018)) [66] and Java (version 8u152, Oracle Corporation, Redwood City) were used as programming languages. The complete source code of the modelling algorithm and the required optical coherence tomography (OCT) import library can be found on the GitHub page of the author.[1]

4.1 MODELLING PROCEDURE
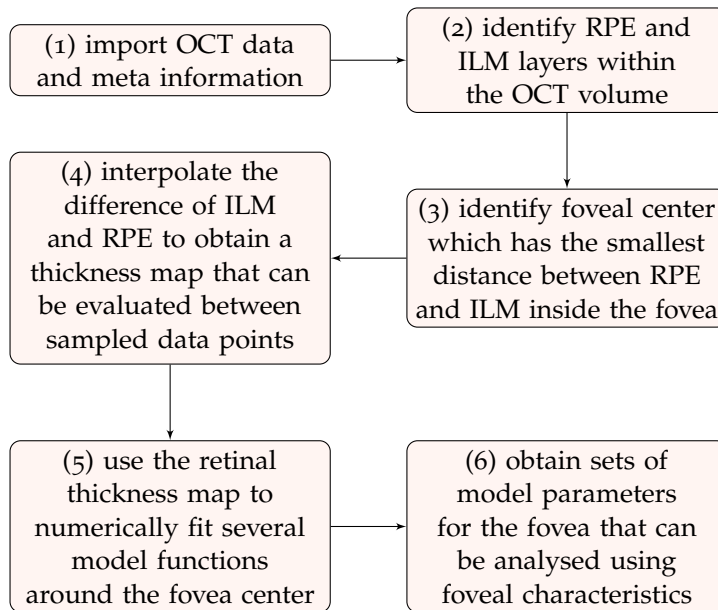
Figure 4.1: Flowchart of the modelling approach.

Figure 4.1 outlines all required steps to model an OCT scan and in the following, we discuss important steps in detail. As step (1) shows, it is first necessary to get access to the OCT data. For certain devices, this might pose

---

a problem as permission to work with proprietary formats is not always granted by manufacturers. Some devices grant access only through their software and expose no interface to the raw OCT data at all. In the case of the SPECTRALIS SD-OCT (Heidelberg Engineering), however, it was possible to implement an importer on the basis of a format specification that allowed for complete access to all acquired scan-, segmentation- and meta-data.

When the OCT data is available, step (2) is to identify the inner limiting membrane (ILM) and retinal pigment epithelium (RPE) layers for each B-scan. For the SPECTRALIS SD-OCT this step is unnecessary as the software contains an internal layer segmentation algorithm and the positions of both layers are included in the data.

The next step (3) is to extract the centre of the fovea within the OCT volume. For this work, we used both an automated and a semi-automated approach to find the centre. The latter one consists of manually obtaining an initial guess for the fovea and finding the correct centre through an optimisation scheme.

The next step (4) is to interpolate the retinal thickness using the foveal centre as the origin of the interpolated coordinate system. After this, the model equation can be fitted in arbitrarily many directions in step (5). This is again an optimisation that targets the difference between model and retinal thickness and minimises the error of the fit.

Once the model parameters are obtained, the fovea can either be analysed with the help of the described fovea characteristics, or one can use particular properties to support a different analysis, e.g. by providing region of interests or selecting patients depending of foveal properties.

In the following, we discuss several aspects of the modelling steps in detail.

4.2   IMPORTING SPECTRALIS SD-OCT DATA

The SPECTRALIS SD-OCT device provides a so-called *raw data export* that saves scans to a binary format. This feature is only available when the scientific version of the software is activated and the manual describing the data format is handed out by Heidelberg Engineering on request.

We have made two implementations available to import SPECTRALIS raw data files. The first one is written as a *Mathematica* package that contains basic functionality for earlier versions of the SPECTRALIS format (version `HSF-OCT-100` and `HSF-OCT-101`). It provides access to the scanned data, the layer segmentations and meta-data like scan settings.[2]

Heidelberg Engineering added several features in newer versions of their raw export and included, e.g. a superior layer segmentation for many internal retinal layers and the export of measurement grids (version `HSF-OCT-102` or later). To make the functionality accessible to more researchers, the existing *Mathematica* implementation was replaced by a Java library.[3]

The Java implementation is to be preferred as it grants access to more features and does not require the expensive *Mathematica* system. Nevertheless, the Java library also includes a *Mathematica* package and it can directly be used within the system. While in [10, 69] the *Mathematica* importer was used to access OCT data, in [70, 71] and for this thesis the Java implementation was employed.

---

2 https://github.com/halirutan/HeyexImport
3 https://github.com/halirutan/spectralis-raw-data
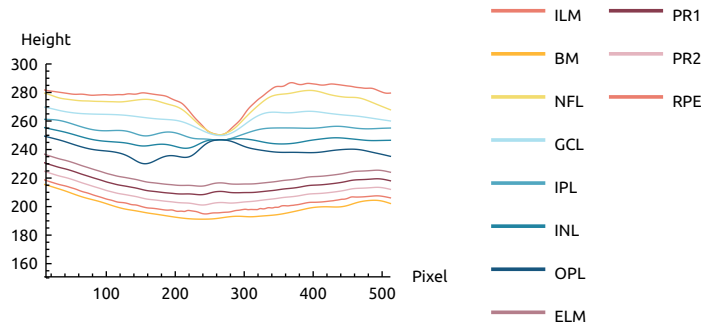
(a)

(b)

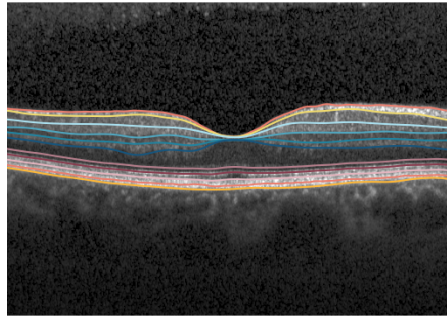**Figure 4.2:** Plot of retinal layers as provided by the SPECTRALIS SD-OCT. (a) shows a plot containing available layers for this particular scan. The coordinate-system of the provided layers refers to the pixel coordinates in the B-Scan. (b) demonstrates the projection of the layers into the corresponding B-scan.

4.2.1   *Example*

As accessing the segmentation layers is the most crucial part, we want to provide a small example that shows how to use the Java API from within *Mathematica*. When using only Java, the approach is similar and examples can be found in the online source code. Listing 4.1 shows how to obtain meta-data about the scan, access a B-scan and extract its layer segmentations.

As a prerequisite to load the package in *Mathematica*, the HSF folder of the repository needs to be placed in the user's package folder. All SPECTRALIS SD-OCT related functions are prefixed with HSF and the code-repository also contains OCT scans that can be used for testing purpose. After loading the package, Listing 4.1 shows how meta-data, the scanned volume and the segmented retinal layers can be accessed. The output of the ListLinePlot in line 11 is shown in Figure 4.2 and the extracted heights of the layers can directly be combined with the B-Scan using HighlightImage. Since the modelling works exclusively on the layer segmentations, a few important points about their properties should be noted:

- The SPECTRALIS SD-OCT might not be able to extract all layers in each B-scan and even successfully segmented layers might contain invalid sampling points. These invalid segmentation points have a specific value to

```
1   << HSF`;
2   file = "scanWithLayers.vol";
3
4   info = HSFInfo[file];
5   scanNumber = 49;
6   nz = info["SizeZ"];
7   bscan = HSFBScanImage[file, scanNumber];
8   layer = HSFLayerSegmentation[file, scanNumber];
9   layer = DeleteCases[layer, {$HSFInvalid ..}];
10
11  ListLinePlot[Evaluate[nz - # & /@ (Values[layer])],
12    PlotLegends -> Keys[layer], PlotStyle -> ColorData[24],
13    PlotRange -> {Automatic, {150, 300}}]
```

Listing 4.1: Extracting a B-scan and its layer segmentations from a SPECTRALIS raw data file.

indicate an error and acquired layers need to be processed accordingly. In the Java library, there is a public `HSFFile.INVALID_FLOAT_VALUE` that indicates an invalid value. This constant can be accessed in Mathematica by using `$HSFInvalid`. It is to be expected that the borders of B-scans contain a few invalid values. For layers that could not be extracted at all, each point contains the invalid constant (we delete them in line 9).

- The values of the retinal layers are the distance from the top of the B-Scan image in pixel. To display them correctly, these values need to be subtracted from number of pixel in this direction. Referring to the volume scan, this size is given as `"SizeZ"` in the scan's meta-data. We extract this value in line 6 and use it again in line 11.

- The meta-data of the scan is accessed through `HSFInfo[file]` in line 4 and provides, e.g. information about number of sampling points and scaling factors for the pixel values to convert data into metric units. Each B-scan also contains meta-data which can be accessed with `HSFBScanInfo` and provides coordinates that map the scan onto the scanning laser ophthalmology (SLO) image.

4.3 INTERPOLATION OF RETINAL THICKNESS DATA

The basis of fitting the model is a retinal thickness map which allows for accessing the thickness on sampled points inside the scanned region. The nature of the radial fitting approach, however, requires an interpolating function $f_{ip}(x, y)$ of the thickness map, since radial directions make it necessary to access thickness values located between sampling points (see Figure 3.2).

The interpolation function $f_{ip}(x, y)$ is the basis for the parametric model fit. To simplify computation, the translation and re-scaling of the coordinate system will be incorporated into the interpolation. In detail, $f_{ip}(x, y)$ is constructed from the thickness map and has the following properties:

- It re-scales the input values so that x and y are in millimetres instead of pixel coordinates.

- It re-scales the output values so that $f_{ip}(x, y)$ is in millimetres instead of pixel values.

- It translates the coordinate system so that $f_{ip}(0,0) = 0$ represents the centre of the foveal pit and shifts the values to minimal central retinal thickness in the fovea (CRT_{min}) so that the centre has a height of zero.

The centre of the foveal pit needs to be extracted either by manual inspection or an automatic algorithm. For OCT scans of sufficient quality, a global minimum search inside the central region returns correct foveal centres in most cases and we discuss this topic in the next section.

The scaling in B- and C-scan direction can be retrieved from the OCT as shown in line 6 of Listing 4.1. Such a conversion is necessary, because the OCT device moves to a different A-Scan position by deviating the laser a certain amount. However, experimenters are interested in the metric distance on the retina between neighbouring A-scans. The SPECTRALIS SD-OCT provides this information in the file header of the scan as the values of "ScaleX" and "Distance".

Before the interpolation, the thickness map is constructed by subtracting the ILM layer matrix from the RPE layer matrix and translating all values by the thickness at the foveal centre. The final construction of the interpolating function in *Mathematica* is shown in Listing 4.2 which takes the retinal thickness map, the position of the foveal centre and the scaling-factors as arguments.

```
1  interpolateFovea[data_, {cy_, cx_}, {sy_, sx_}] := Module[{nx, ny},
2    {ny, nx} = Dimensions[data];
3    ListInterpolation[
4      data,
5      {sy ({1, ny} - cy), sx ({1, nx} - cx)},
6      Method -> "Spline"
7    ]
8  ];
```

Listing 4.2: Construction of an interpolating function for the retinal thickness. Through its arguments, it can incorporate the correct scaling to metric units and it translates the origin of the function to the centre of the fovea.

Figure 4.3 shows a plot of such an interpolated thickness map that was constructed from an OCT scan. The visible noise and the B-scan lines from left to right in the original OCT data underline why a direct quantification of the data is difficult without either heavy preprocessing or, like in the case of the work here, fitting a smooth model.
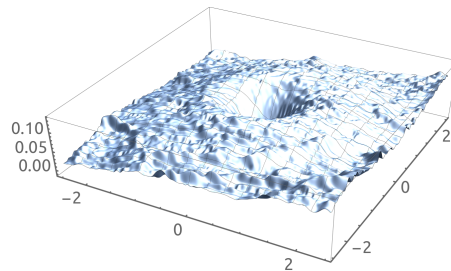
Figure 4.3: Surface of the interpolated retinal thickness map acquired from an OCT scan.

4.4   EXTRACTING THE FOVEAL CENTRE

Assuming that the common fovea has the shape of a pit, we are interested in the position of minimal retinal thickness inside the pit. Finding the centre completely automatically, however, can be tricky, because regions outside the foveal area might possess a retinal thickness that is below the value inside the foveal pit. Therefore, it is required to restrict the search region to the part where the fovea resides. Additionally, the noise in the scan might introduce local minima and the thickness data should be smoothed before searching for the minimum.

Here, we propose two different ways that work on foveal OCT scans of sufficient quality. The first method starts by calculating the thickness map as shown in the previous section. The next step is to smooth-out the noise by applying a Gaussian filter of sufficient radius which should take into account that the scanned data is usually anisotropic, i.e. the B-scan direction has a finer sampling than the C-scan direction. Finally, a simple loop is used to iterate over the central 50 % of scanned region to find the position with the minimal thickness value. This method works well on many datasets if no other information than the retinal thickness is available.

The second method uses a better initial estimate of the fovea position and has been proven to work reliably in a large set of over 900 OCT scans employed for a currently unpublished study. Recent versions of the SPECTRALIS SD-OCT file format support measurement grids to provide insight into the retinal thickness of different sectors of the fovea[4]. The grid is automatically positioned close to the foveal centre but with varying accuracy. However, the location can serve as an initial estimate of the foveal position.

To employ the grid coordinates, further processing is necessary as the coordinate system of the grid and the B-scans and their layer segmentations refer to the coordinate-system of the SLO image. Therefore, to map the centre of the grid into the thickness matrix, the transformation of the scanned area needs to be calculated by extracting the coordinates of the B-scans from the meta-data and computing the underlying rigid transformation.

By interpolating the smoothed retinal thickness matrix, the `NMinimize` function of Mathematica can be used to (1) automatically search for the minimum without an explicit loop, (2) restrict the search area to a circle around the grid position and (3) set the initial starting point to the centre of the grid.

4.5   NUMERICAL ESTIMATION OF MODEL PARAMETERS

Fitting the model onto an OCT dataset is an optimisation problem with the objective to minimise a certain distance between the model function and the retinal thickness data. The fitting procedure will find model parameters along one particular direction φ from the foveal centre outwards up to a radius $r_{\max}$.

The distance- or target-function to be optimised is the integral over the squared errors with the constrains that the found values for the parameters are restricted to their valid ranges. Given the interpolation of the thickness

---

4 One particular grid, the EDTRS grid, was explained in Section 2.1.1.1

map $f_{ip}(x, y)$, an arbitrary angle $0 \leq \varphi < 2\pi$ which defines the radial direction of the fit, and the fitting radius r_{max}, the target function is given by

$$\min_{\mu, \sigma, \gamma, \alpha} \int_0^{r_{max}} \left(f_{ip}(r\cos(\varphi), r\sin(\varphi)) - \mathcal{M}(r; \mu, \sigma, \gamma, \alpha) \right)^2 \, dr \tag{4.1}$$
$$\text{subject to } 0 < \mu \leq 12, \ 0 < \sigma < 2, 1 < \gamma < 10, \ -1 < \alpha < 1.$$

The constraints in Equation 4.1 are a combination of theoretical considerations as pointed out in Section 3.2 and practical experiences from numerous successful model fits. While, theoretically, e.g. only $\mu > 0$ is required, the upper bound helps to speed up the minimisation algorithm which takes constrains into account to adjust the search space. However, note that compared to the original publication [10], the parameter ranges were extended to some degree to allow for a wider range of possible foveal shapes.

To determine the solution of Equation 4.1, a discretised version of the integral was used with the Differential Evolution (DE) optimisation [72], which is one of the underlying algorithms in *Mathematica*'s NMinimize routine (see Section 4.6.1 for details). The fitting step is repeated to calculate a parameter set for every desired radial direction around the foveal centre. The angle between each fitted direction is completely arbitrary, but smaller angles increase the number of directions, by this enhancing the resolution of the three-dimensional reconstruction.

In the numerical approximation of Equation 4.1, the interpolating function f_{ip} is not accessed directly. Rather, it is sampled in one direction φ returning a list of radius-values and corresponding f_{ip} values as shown in Listing 4.3. This approach has the advantage that the interpolating function is not required during the optimisation procedure and needs to be accessed only once during sampling.

```
getTargetFuncPoints[phi_, fovea_, rEnd_, nSamplingPoints_] := Transpose[
  Table[
    {r, fovea[r * Sin[phi], r * Cos[phi]]},
    {r, 0, rEnd, N[rEnd / (nSamplingPoints - 1)]}]
  ]
];

model[m_, s_, g_, a_, r_] := (r^g*m*s^2)*Exp[-r^g*m] + a (1 - Exp[-r^g*m]);
rmsModel[m_, s_, g_, a_, rPts_, fovPts_] :=
  Sqrt[Mean[(model[m, s, g, a, rPts] - fovPts)^2]]
```

Listing 4.3: Sampling of f_{ip} in one direction φ (line 1 to 6). The arguments of getTargetFuncPoints are the desired direction φ, the interpolated thickness map f_{ip}, r_{max} and the number of requested sampling points along the direction. The returned sampling points are employed in rmsModel to calculate the RMS for the model with parameters m, s, g, and a.

The final implementation of the fovea modelling provides more features to parallelise the fitting in different directions, adjust initial optimisation parameters for accuracy and speed, and to process OCT scans automatically. However, the sampling and the target-function containing rmsModel are at the very core of the procedure and we can use artificial data to show a complete fit.

4.5.1 *Example*

Assuming the functions `model` and `rmsModel` are defined as above, we can create an artificial example of noisy foveal shape data using known model parameters and fit the model. Although it does not resemble the original fluctuations in the retinal layers which are introduced by a combination of OCT noise and errors in the layer segmentation algorithm of the device, we will use an additive, uniformly distributed noise term in the example below.

```
1   With[{m = 1.3, s = 0.6, g = 1.67, a = 0.125},
2     data = Table[
3       {r, model[m, s, g, a, r] + RandomReal[{-.01, .01}]},
4       {r, 0, 3, 0.01}
5     ]
6   ];
7
8   With[{d = Transpose@data},
9     callTargetFunc[args__?NumericQ] := rmsModel[args, d[[1]], d[[2]]]
10  ]
11
12  NMinimize[{
13    callTargetFunc[mu, sigma, gamma, alpha],
14    And[0 < mu < 12, 0 < sigma < 2, 1 < gamma < 10, -1 < alpha < 1]},
15    {mu, sigma, gamma, alpha},
16    Method -> "DifferentialEvolution"
17  ]
18
19  (*
20    {0.00570828,
21    {mu -> 1.30393, sigma -> 0.601235, gamma -> 1.66197, alpha -> 0.124728}}
22  *)
```

Listing 4.4: Minimal example of fitting the model equation using DE. The noisy `data` simulates the sampled retinal thickness from the OCT scan and is created by using the model with the parameters $\mu = 1.3$, $\sigma = 0.6$, $\gamma = 1.67$ and $\alpha = 0.125$ and adding random noise. A target function is constructed which employs the RMS and is then used in the optimisation procedure. The resulting RMS and the estimated model parameters are given in the lines 20 and 21 respectively.

In Listing 4.4, the first code-block creates the sampled, noisy foveal shape from known model parameters. In the second block, we define the target function that takes a sequence of parameter values `args` and calculates the RMS of the differences between the model with these parameters and the sampled shape.

The definition of the target function in lines 8 to 10 contains two crucial parts. First, the arguments of `callTargetFunc` are guarded by `NumericQ` to make the function only applicable if numeric values are provided. This is important to prevent the `NMinimize` call from evaluating it symbolically. Secondly, the data is transposed to the form $\{\{r_1, r_2, \ldots\}, \{v_1, v_2, \ldots\}\}$, where r_i are the radii values and v_i are corresponding foveal shape values. This structure change is necessary to employ optimised vector instructions in the call to `rmsModel` which works on lists rather than performing an explicit iteration over the values to calculate the RMS. In Section 4.6.2, we will discuss this matter in greater detail.

The last block calls `NMinimize` to find the best fitting model parameters for the data and the last comment shows the result which has the RMS as its first element.
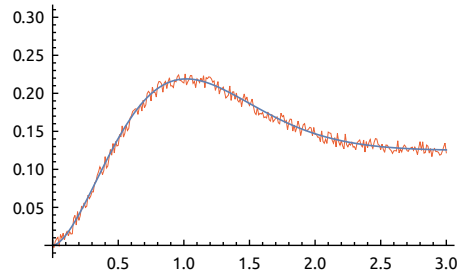
Figure 4.4: Result of the example fit from Listing 4.4.

As expected with such an artificial example, the found model parameters represent the defined values accurately. In addition to the numeric results, Figure 4.4 shows a plot of the example-data and the fitted model function.

For real OCT data, the fit shown above is executed for different directions. The case which is displayed in Figure 3.2 results in eight parameter sets. The sampling directions which were fitted are $0, \frac{\pi}{4}, \frac{2\pi}{4}, \ldots, \frac{7\pi}{4}$, where each fit is represented by separate values for μ, σ, γ and α.

4.6 PERFORMANCE CONSIDERATIONS

4.6.1 *Differential Evolution optimisation*

The DE algorithm optimises a problem by maintaining a set of initial *agents*. The agents are points in the parameter space and represent solution candidates that are improved during the iterations of the algorithm. In the case of the fovea model, an agent is a tuple $\mu, \sigma, \gamma, \alpha$ and during each DE-iteration, its position in the parameter space is recalculated by combining the positions of three, randomly selected other agents in a certain manner (for details, we refer to [72]). When the new position leads to an improvement, the agent is assigned the new parameter set. When one of the agents has reached a solution of sufficient quality or when the number of iterations exceeds a particular value, the algorithm returns the parameter set of the most successful agent.

Evidently the positions of the initial agents in the parameter space have influence on the convergence-speed of the algorithm. It needs to be ensured that initial points are valid regarding the parameter restrictions provided, and they should sample the whole parameter space. However, during the modelling of a large set of OCT scans, the model parameters of previous calculations can serve as additional initial agents for subsequent runs of the procedure. Since common foveal shapes occupy only a sub-region of the parameter space, this can lead to an improvement as fewer iterations are required to achieve a solution of sufficient quality.

Figure 4.5 shows the example from Section 4.5 where explicit initial points for the DE-algorithm were chosen. The coloured points are the positions of the DE-agents for the parameters μ and σ. In the first row of this figure, 20 random points are used as initial agents and after 10 iterations, none of the final agents (shown in red) resemble the exact solution to a sufficient degree. In the second row, five of the random points were replaced by points near the final solution which ensures that (a) the DE-algorithm is guided to some degree and (b) the parameter space is still sampled sufficiently to allow for extreme shapes. As Figure 4.5d shows, even after 10 iterations, a sufficient number of agents have already converged close to the exact solution. In fact,
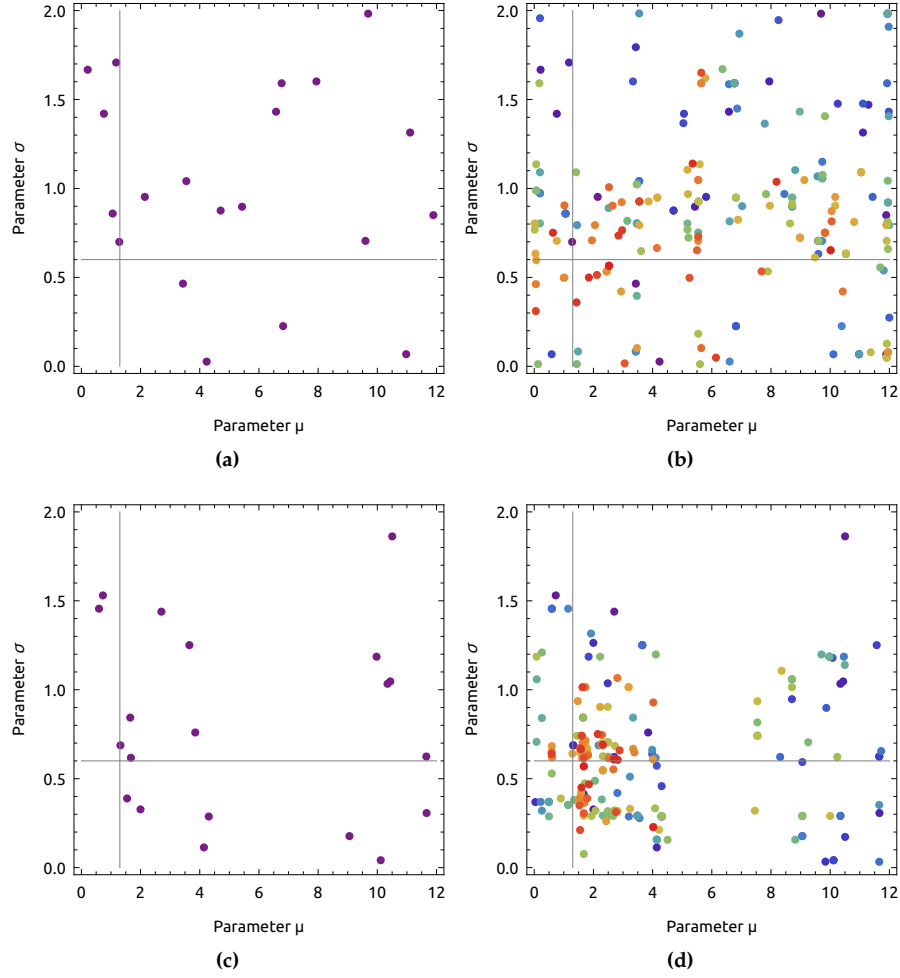
Figure 4.5: Convergence of DE after 10 iterations (from purple to red) of the parameters μ and σ. The gray cross-hairs indicates the position of the exact solution. (a) shows the positions of the 20 randomly chosen points. In (b), the progression during the iterations can be observed. Even in the later iterations (red), many agents are still not close to the desired solution. (c) shows 15 randomly chosen points and 5 points that are near the desired solution. Evidently, (d) shows that agents are closer to the solution after 10 iterations.

while the remaining optimisation error is 0.0233 for Figure 4.5b, it is with 0.0158 notably smaller for Figure 4.5d.

To improve the convergence of the DE-algorithm further, hybrid approaches have been suggested that include a fast, local optimisation step in each iteration to improve the position of the agents [73]. When such a local optimisation step is included, the remaining error of the example from Figure 4.5d drops to 0.0058 after 10 iterations.

In summary, if parameters of similar foveal shapes are available, including them in the list of initial points in addition to the random agents can help the DE to find better solution candidates in fewer iterations. Furthermore, we advise to improve the global optimisation by including a local search after each iteration. Both suggestions might notably improve the accuracy of the sought solution after a fixed number of iterations.

4.6.2 *Parallelisation on different levels*

Today, even normal desktop machines have several physical central processing unit (CPU) cores available and many modern CPUs include extensions for vectorised computation. The nature of the presented modelling procedure allows for parallelisation on different levels. First, the fitting of the model function in several directions is independent from one another and each fit can run as a separated computation. The changes in the implementation are minimal apart from assigning each fit its own computational thread. For this reason, such parallelisation is often referred to as embarrassingly parallel problem [74]. Most of the modern programming languages offer ways to employ this kind of parallelisation. For C++ two prominent frameworks are OpenMP[5] and the Threading Building Blocks[6] which provide advanced features but also allow for such a direct parallelisation.

Mathematica provides the Parallel Computing Tools[7] but there, the parallelisation is more expensive because *Mathematica*, as an interpreted language, maintains a computational kernel with all definitions for the current session. When a parallel task is employed, subkernels are started and each parallel task runs on its own, independent subkernel. This, however, requires that all necessary function definitions and data are transferred to the subkernel which can lead to performance bottlenecks when large chunks of data need to be sent between the main computational kernel and the subkernels for input or output. For the modelling here this is of no major concern since only the vector of sampled OCT thicknesses for the current direction is required on each subkernel and the parameter set for the fitted foveal shape is the sole return value that needs to be transferred back to the main kernel. Therefore, a first step in improving the performance is to distribute the fitting of different foveal directions to different threads which run in parallel.

But even with distributed fitting, there is still room for improvement. As shown in the previous section, the DE-algorithm updates the solution candidates, i.e. agents, by constantly recalculating the RMS on new position in the parameter space. We chose the target function to be the RMS between the sampled OCT retinal thickness and the fovea model evaluated on the sampling points. In the sequential DE algorithm, the most expensive calculation is the repeated evaluation of the RMS for different values of μ, σ, γ, and α for all agents in every iteration.

The RMS-calculation consists of computing the squared distance between model and OCT measurement for each sampling point, calculating the mean of the values and finally the square-root of the result. Instead of calculating the squared distances with an iteration point by point, modern computer architectures provide vector instructions which are optimised for performance. This form of parallelisation is commonly referred to as single-instruction, multiple data (SIMD) in which the same operation is calculated independently on several data elements using special vector processing units of today's hardware. Many programming languages expose such features either through libraries or they support such operations natively. In C++, libraries like the Intel Integrated Performance Primitives (IPP)[8] or the Intel Math Kernel Library (MKL)[9] offer a large variety of highly optimised, mathematical functions

---

5 https://www.openmp.org/
6 https://www.threadingbuildingblocks.org/
7 https://reference.wolfram.com/language/ParallelTools/tutorial/Overview.html
8 https://software.intel.com/en-us/intel-ipp
9 https://software.intel.com/en-us/mkl

that work on vector arguments. OpenMP also contains specific directives to employ SIMD parallelisation.

Mathematica has support for vector operations and functional programming paradigms built into the language. Many mathematical functions are *listable* and can take arbitrary tensors as input and perform the calculation by applying the function on the elements of the tensor. For machine precision numbers, such operations are internally optimised and use libraries like IPP or MKL to offer vectorised evaluation.[10]

In Listing 4.3, we have already seen how to employ the listability of numerical functions in the definition of rmsModel for calculating the squared differences between the model and OCT sampling points. There, the sampled points fovPts and the sampling radii rPts are vectors of numbers and the vector of squared differences is calculated without an explicit iteration by using the lists as arguments instead of single numbers.

```
1   model[m_, s_, g_, a_, r_] :=
2       (r^g * m * s^2) * Exp[-r^g * m] + a (1 - Exp[-r^g * m]);
3
4   (* RMS that natively works on tensors *)
5   rmsModel[m_, s_, g_, a_, rPts_, fovPts_] :=
6       Sqrt[Mean[(model[m, s, g, a, rPts] - fovPts)^2]];
7
8   (* RMS implementation with explicit iteration *)
9   rmsModelIter[m_, s_, g_, a_, rPts_, fovPts_] := Module[
10    {
11      sqrDiff = 0.0
12    },
13    Do[
14      sqrDiff += (model[m, s, g, a, rPts[[i]]] - fovPts[[i]])^2,
15      {i, Length[rPts]}
16    ];
17    Sqrt[sqrDiff / Length[rPts]]
18  ];
19
20  (* Creating 10^6 sampling points for speed-test *)
21  n = 10^6;
22  {mu, sigma, gamma, alpha} = {1.0, 0.5, 2.0, .1};
23  rPts = Range[0, 3, 3.0/(n - 1)];
24  fovPts = model[mu, sigma, gamma, alpha, rPts];
25
26  AbsoluteTiming[rmsModel[mu, sigma, gamma, alpha, rPts, fovPts]]
27  AbsoluteTiming[rmsModelIter[mu, sigma, gamma, alpha, rPts, fovPts]]
```

Listing 4.5: Comparison of RMS calculation performance. The first implementation (lines 4 to 6) employs *listable* operations, while the second one (lines 8 to 18) uses an explicit iteration over the elements. For 10^6 sample points, the iterative implementation rmsModelIter needs 6.053 s to finish, while rmsModel needs only 0.024 s.

Listing 4.5 compares the performance of this implementation with a version of the RMS that is computed using an explicit loop to iterate over the elements. The runtime over 10^6 sampling points for the loop implementation is 6.053 s, while the rmsModel function only needs 0.024 s. The rmsModel implementation is not only about 250 times faster and easier to understand, it is also more accurate because the Mean function employs a compensated summation which does not exhibit the numerical errors of a forward summation [75].

To conclude: For prototyping and testing, the above considerations about performance are of secondary nature. However, if the goal is to model a

---

large set of OCT scans or to implement a program which can model foveae in real-time, a careful profiling of performance bottlenecks is required to apply optimisation at the right places. In this section, we presented thread parallelisation and vectorisation techniques for the CPU. However, today's graphics hardware offers a wide range of parallelisation possibilities and allows for the usage of several thousand processors. Computing frameworks like CUDA or OpenCL provide user-friendly application programming interfaces (APIs) to access the underlying hardware capabilities, and bindings for several programming languages exists. Although it was not evaluated in the scope of this work, the fovea modelling might benefit from such a massive parallelisation.

5

RESULTS AND DISCUSSION OF APPLICATIONS

In this chapter, we want to look at different applications of the fovea model. We start by presenting the results of the initial feasibility study that showed the successful application of the fovea model on a large dataset of optical coherence tomography (OCT) scans [10]. This will be followed by the results of a detailed study that aimed to uncover properties of the foveal characteristics, their asymmetries and correlations regarding, e.g. eye position and gender [69]. In Wagner et al. [70], we analysed properties of the choroid boundary and used the fovea model to calculate anatomical regions of interest. Finally, the model was used in Frey et al. [71] to calculate the model parameters for an *average* fovea based on the results of Scheibe et al. [69]. The calculated parameters were then used to select an OCT scan that closely matches the average fovea, and employ it in a light-ray simulation. Finally, in unpublished work that is currently in preparation, we modelled the deep, funnel-like foveae of kestrels to investigate in the development of these exceptionally interesting structures.

All studies in the next sections that base on human subjects followed the tenets of the Declaration of Helsinki for the use of human subjects. Details about the experimental setup and biological discussions can be found in the corresponding publications. In the following, we concentrate on results and discussions of the modelling and foveal characteristics.

5.1 FEASIBILITY STUDY
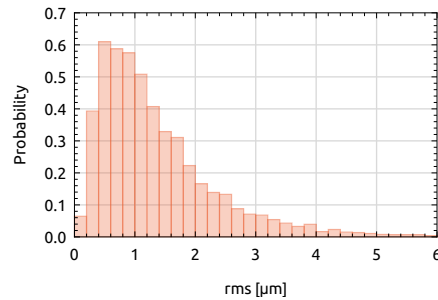
Figure 5.1: Histogram of fitting errors. The errors are Gamma-distributed with a mean of 1.40 μm. The maximum of the distribution is located at 0.684 μm.

In a first feasibility study, we applied the model approach presented here on a large set of human OCT scans and calculated basic fovea characteristics [10]. The goal was to gain insight into the behaviour and quality of the fovea model. Therefore, we used a database of 460 OCT scans and dismissed 28 where either the quality of the scan or the retinal pigment epithelium (RPE)/inner limiting membrane (ILM) segmentation turned out to be insufficient. For

Parameter	Mean	Standard deviation
μ	1.28	0.290
σ	0.471	0.0649
γ	1.69	0.243
α	0.0586	0.0452

Table 5.1: The mean and standard deviation of the model parameters found in 5184 fits.

the remaining 432 datasets, 12 directions (equally distributed in $\pi/6$ steps) were modelled with a fit radius r_{max} of 2 mm each, and therefore exactly $432 \times 12 = 5184$ fits were carried out.

In Figure 5.1 the distribution of the root mean square (RMS) of all fits is depicted. The mean of this distribution is 1.40 µm with a standard deviation of 1.002 µm. Compared to the mean retinal thickness of 231 ± 19 µm for the right eye and 230 ± 19 µm for the left eye that was measured by the SPECTRALIS SD-OCT (Heidelberg Engineering), the error of 1.40 µm is negligible.

Table 5.1 shows statistical values of the parameters present in the model and describes the mean fovea shape of the population investigated. Note that, due to the distinct influence of each parameter on the profile of the model, the standard deviations cannot directly be compared.

The most likely error source of the method is the OCT acquisition procedure, because most artefacts appearing are measurement inaccuracies, caused by the technician during the OCT scan acquisition. The following list provides a detailed explanation of all errors found in the 28 dismissed scans:

- During the measurement, the technician aims to keep the laser at the right distance to the retina. This adjustment has to be done manually and failed in 14 cases. The result is a horizontal cropping at the top of the scan, which appears as sharp cut-off in the final OCT scan.

- In an optimal measurement, the laser is centred in the pupil plane to maximise the light intensity reaching the retina. When the technician does not recentre the laser optimally, a vertical cropping of the scan occurs. The final OCT scan is then affected by two artefacts: primarily, the scan appears slanted to one side, and, if not corrected at this point, a gradual fading towards the edge of the scan occurs. 7 datasets were affected by this error.

- When the subject does not fixate centrally, the measured region has to be adjusted by the technician to map the foveal region of interest. If the technician fails to carry out this manual re-mapping, a different area of the retina is scanned, and the fovea is not centred in the final OCT dataset. With a de-centred fovea, insufficient data is available in some directions, and the model fit cannot be carried out. This has occurred in 4 datasets.

- In subjects where the vitreous body is retracted, a second bright line appears in the OCT scan, somewhat parallel to the retina. This line is falsely detected as ILM by the SPECTRALIS SD-OCT segmentation software, and renders a model fit impossible. This has occurred in 3 cases.

Another potential source of error is the retina layer detection algorithm of the SPECTRALIS SD-OCT on boundary regions. Although the software extracted the layer data reliably for most parts of the scanned volume, near the boundary a few data points were missing in examined patient scans. Therefore, one should include a safety margin instead of fitting the model for the whole extent of the scanned area to ensure that the procedure uses correctly identified RPE/ILM data only. Although the above errors are not related to the model procedure, they might have a severe impact on the overall success of the approach.

Finally, Figure 5.2 shows the central slice of a region extended beyond the modelled area. The red line depicts the model function with the calculated parameters for this specific fovea. Noteworthy, only the solid line represents the region fitted, while the dashed part shows a strikingly good accordance with the real retinal surface even outside the modelled area. However, one should always be aware that areas outside the fitted regions are an *extrapolation* and should not be used without verification.
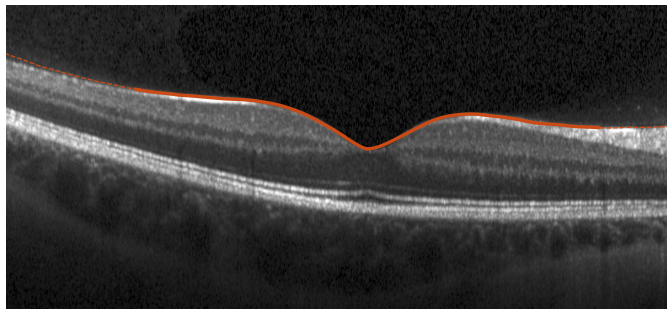
Figure 5.2: Projection of the modelled fovea into the appropriate image plane of the original OCT scan. The solid line indicates the 5 mm central region used for fitting the model. The dashed line represents an extrapolation of the model function outside the fitted region.

In summary, this work showed that the presented model allows a detailed three-dimensional analysis of the fovea, additionally to an exact mathematical calculation of all relevant parameters, which describe the foveal structure and its asymmetry. By applying this model, a few defined parameters can be used to compare individual foveal profiles.

5.2 FOVEAL CHARACTERISTICS AND THE ASYMMETRY OF THE FOVEAL PIT

In a second publication, we aimed to investigate the foveal properties of subjects from a study that fulfilled certain requirements regarding patient health, gender and age distribution [69]. For this, 220 strictly controlled Caucasian subjects of European descent were employed [76]. From the 220 patients both eyes were scanned, but 31 OCT scans needed to be discarded for bad quality and therefore, 409 OCT scans were analysed. For 19 subjects only the right scan and for 12 subjects only the left scan was available and, therefore, the analysis employed 208 right and 201 left eyes.

The data presented are based on 109 men and 111 women aged 21 years to 77 years with a mean/SD of 43 ± 13 years and 44 ± 14 years respectively. The men and women were within the following age decade brackets: 20 year-decade: 25 men and 25 women, 30 year-decade: 21 men and 18 women, 40 year-decade: 29 men and 28 women, 50 year-decade: 19 men and 22

women, 60 year-decade: 12 men and 16 women, and 70 year-decade: 3 men and 2 women.

The refractive error was distributed in a range of −9 D to 6 D with a mean/SD for men of −1.04 ± 2.24 D and women of −0.631 ± 2.250 D. Women and men showed no significant differences in ametropia ($p = .108$). Refraction was quantified based on the sphere obtained during best corrected subjective refraction. This spherical refractive error was more hyperopic as expected with age (men: $r = 0.321$, $p < .001$, women: $r = 0.39$, $p < .001$). Axial length was distributed between 20.8 mm to 27.6 mm with a mean/SD of 24.30 ± 1.02 mm for men and 23.40 ± 1.01 mm for women. A more detailed statistic of the sampled eyes' properties can be found in Table 5.2.

eye	age	AL	BCVA	SE	S
right	42.6 ± 13.6	23.8 ± 1.12	−0.119 ± 0.0862	−0.523 ± 2.18	−0.823 ± 2.24
left	42.7 ± 13.6	23.8 ± 1.13	−0.125 ± 0.0774	−0.553 ± 2.19	−0.824 ± 2.23

Table 5.2: Properties of subjects' right and left eyes given as mean and standard-deviation. The table shows age (in years), axial length (AL in mm), best corrected visual acuity, which is the visual acuity in logMAR achieved with the optimal refractive correction in place (BCVA in logMar), spherical equivalent (SE in D) and sphere (S in D).

All datasets were captured with a SPECTRALIS SD-OCT (Heidelberg Engineering) where each volume scan consisted of 97 B-scans with 512 A-scans per B-scan and 496 sample points per A-scan. For each OCT scan, an angle of 20° in both, x- and y-direction was used. The resulting exact metric dimension in x- and y-direction depends on the subject's specific eye parameters, but each dataset represents a scanned volume of approximately 6 mm × 6 mm × 1.92 mm. The correct OCT image magnification was calculated, taking into account the subject's anterior corneal radius (mean of steep and flat meridian) and the focus obtained during measurement. These values were used to follow the approach given in the work of Garway-Heath et al. [77].

5.2.1 *Fovea modeling*

For each eye 40 equally angular distributed radial fovea fits were calculated, resulting in a total of 16 360 foveal model shapes. The overall RMS fit error was 3.01 ± 1.09 µm. Based on the model-parameters μ, σ, γ, and α, the following foveal characteristics were investigated

1. maximum hight on the foveal rim (see Section 3.3.2)

2. maximum foveal slope (see Section 3.3.3)

3. central foveal subfield thickness (CFST) (see Section 3.3.4)

4. area inside the foveal bowl (see Section 3.3.5)

5. foveal radius (see Section 3.3.7)

Table 5.3 shows the mean/SD values of all obtained model parameters and foveal characteristics. For each presented property the median value of all fitted 40 directions and the values in four anatomical directions are given (i.e. nasal, temporal, inferior and superior). Additionally, each row is divided into right and left eye to make a direct comparison possible. Finally, the table
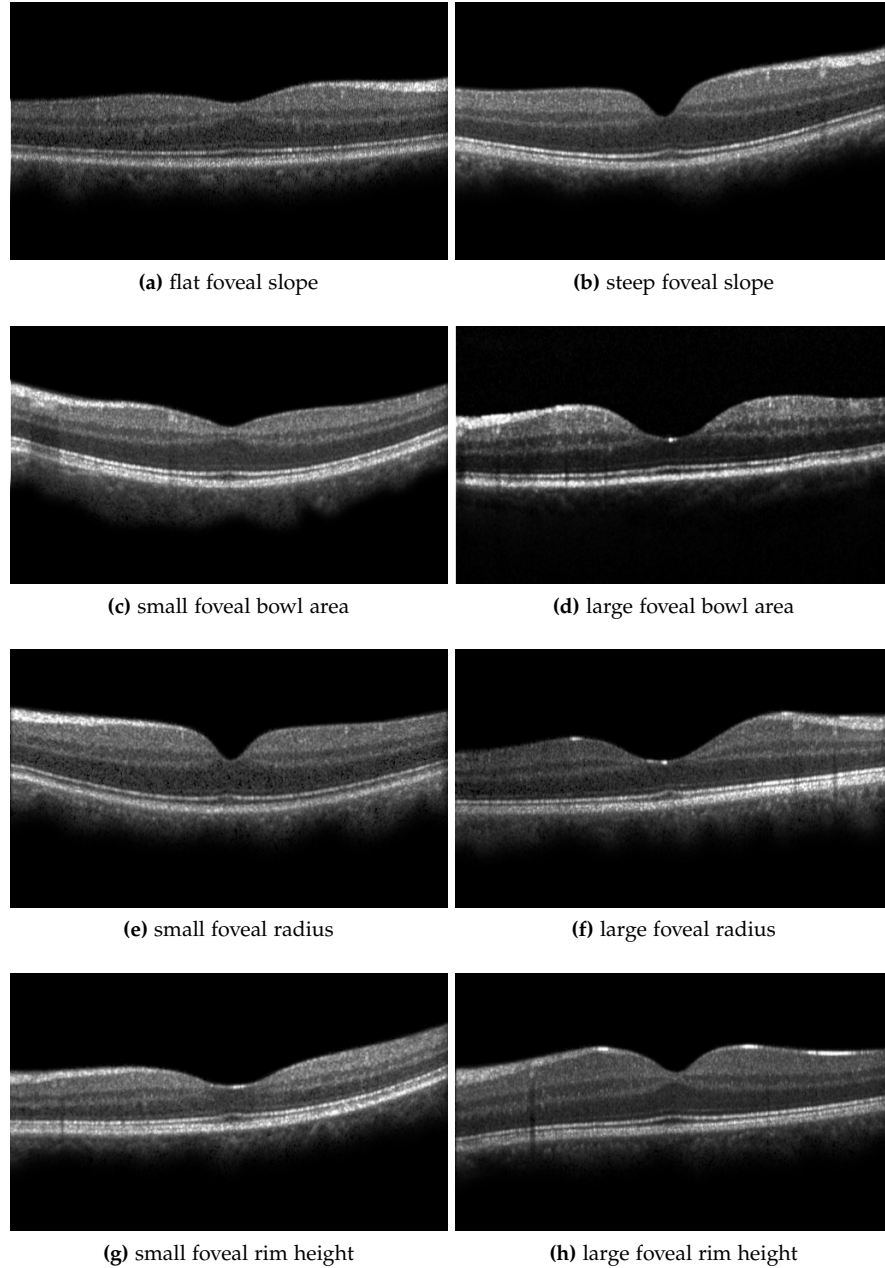
is divided into three large blocks separately showing the groups: all subjects, male subjects and female subjects. In addition to Table 5.3, mean/SD values of CFST and minimal central retinal thickness in the fovea (CRT_{min}) split by gender and eye position are given in Table 5.4.

		model parameters				foveal characteristics			
		μ	σ	γ	α	slope [°]	A_{bowl} [mm²]	r_{fov} [mm]	h_{rim} [μm]
all subjects									
median	r	1.26±0.185	0.472±0.0378	1.68±0.195	0.0610±0.0319	11.5±2.11	0.0537±0.0130	0.874±0.0772	357±15.6
	l	1.26±0.183	0.470±0.0344	1.68±0.190	0.0628±0.0294	11.5±2.10	0.0539±0.0129	0.879±0.0752	357±15.6
nasal	r	1.10±0.302	0.469±0.113	1.67±0.235	0.0593±0.114	10.6±2.04	0.0628±0.0153	1.00±0.110	360±16.0
	l	1.19±0.341	0.450±0.0839	1.68±0.224	0.0742±0.0525	10.9±2.09	0.0616±0.0153	0.975±0.108	361±16.2
temporal	r	1.23±0.271	0.451±0.0550	1.66±0.212	0.0518±0.0361	10.1±2.13	0.0486±0.0127	0.894±0.0933	342±15.8
	l	1.14±0.241	0.468±0.0866	1.66±0.223	0.0392±0.0837	9.81±2.00	0.0499±0.0132	0.920±0.0933	342±15.6
inferior	r	1.30±0.249	0.512±0.0671	1.63±0.204	0.0421±0.0531	12.3±2.29	0.0508±0.0130	0.826±0.0803	357±16.3
	l	1.28±0.240	0.516±0.0638	1.63±0.228	0.0396±0.0511	12.3±2.22	0.0506±0.0127	0.827±0.0784	357±16.2
superior	r	1.43±0.249	0.470±0.0431	1.74±0.220	0.0721±0.0306	12.7±2.30	0.0549±0.0137	0.837±0.0822	362±16.5
	l	1.43±0.244	0.466±0.0439	1.74±0.196	0.0747±0.0328	12.6±2.37	0.0554±0.0135	0.843±0.0773	363±16.5
male									
median	r	1.26±0.194	0.484±0.0410	1.62±0.177	0.0562±0.0345	11.8±2.16	0.0523±0.0124	0.861±0.0809	360±14.7
	l	1.26±0.195	0.482±0.0328	1.62±0.171	0.0593±0.0308	11.8±2.03	0.0528±0.0125	0.864±0.0778	360±15.1
nasal	r	1.07±0.312	0.494±0.142	1.60±0.220	0.0419±0.154	10.8±2.16	0.0613±0.0145	0.993±0.104	363±15.6
	l	1.19±0.399	0.464±0.0927	1.62±0.216	0.0693±0.0526	11.2±2.03	0.0605±0.0148	0.966±0.106	365±16.3
temporal	r	1.24±0.314	0.459±0.0667	1.62±0.210	0.0481±0.0387	10.3±2.16	0.0475±0.0127	0.884±0.105	345±15.1
	l	1.14±0.275	0.486±0.102	1.60±0.212	0.0290±0.109	10.1±1.97	0.0490±0.0129	0.905±0.0998	346±14.8
inferior	r	1.29±0.265	0.531±0.0774	1.58±0.200	0.0321±0.0640	12.6±2.39	0.0494±0.0124	0.813±0.0806	361±15.7
	l	1.28±0.263	0.530±0.0638	1.56±0.211	0.0330±0.0559	12.6±2.16	0.0490±0.0124	0.813±0.0837	360±15.6
superior	r	1.46±0.243	0.477±0.0437	1.70±0.194	0.0692±0.0308	12.9±2.28	0.0528±0.0128	0.816±0.0800	364±15.4
	l	1.44±0.244	0.474±0.0431	1.70±0.182	0.0723±0.0324	12.9±2.29	0.0542±0.0129	0.829±0.0783	366±15.2
female									
median	r	1.26±0.176	0.460±0.0294	1.73±0.198	0.0659±0.0282	11.3±2.04	0.0552±0.0135	0.887±0.0712	354±15.9
	l	1.26±0.171	0.457±0.0317	1.74±0.192	0.0664±0.0275	11.3±2.14	0.0550±0.0133	0.893±0.0699	354±15.7
nasal	r	1.13±0.289	0.444±0.0654	1.75±0.228	0.0771±0.0413	10.5±1.90	0.0643±0.0159	1.01±0.117	357±15.7
	l	1.19±0.270	0.435±0.0713	1.75±0.217	0.0793±0.0522	10.7±2.13	0.0626±0.0159	0.985±0.111	357±15.4
temporal	r	1.21±0.220	0.443±0.0387	1.71±0.205	0.0557±0.0330	9.91±2.08	0.0497±0.0126	0.905±0.0784	339±15.9
	l	1.13±0.202	0.449±0.0620	1.72±0.220	0.0498±0.0426	9.51±2.00	0.0509±0.0134	0.935±0.0840	339±15.7
inferior	r	1.31±0.233	0.493±0.0480	1.69±0.192	0.0523±0.0367	11.9±2.14	0.0522±0.0135	0.838±0.0783	354±16.1
	l	1.28±0.216	0.502±0.0609	1.69±0.227	0.0465±0.0449	11.9±2.23	0.0522±0.0130	0.842±0.0701	354±16.3
superior	r	1.40±0.253	0.463±0.0416	1.78±0.237	0.0750±0.0303	12.4±2.29	0.0570±0.0143	0.859±0.0792	359±17.3
	l	1.42±0.245	0.457±0.0433	1.78±0.202	0.0772±0.0331	12.3±2.43	0.0567±0.0140	0.858±0.0737	360±17.4

Table 5.3: Calculated model parameters and foveal characteristics grouped by gender and divided into main anatomical directions. The values in the table show the mean and the standard deviation over all subjects in the specified group. The rows of the table are split into three main groups which are (1) all, (2) male and (3) female subjects. For each mentioned group, model parameters and foveal characteristics are given by a median value of the 40 fitted directions or by a value in one of the four anatomical directions (nasal, temporal, inferior and superior). Furthermore, each row contains values of left and right eyes separately. For every entry in the table, the mean and the standard deviation is given. While the model parameters are unit-less, the used units for foveal slope, bowl area, radius and rim height can be found in the table heading.

Figure 5.3 shows examples of foveae that exhibit extreme values in particular foveal characteristics. The selected OCT images are the central scans through the fovea and show the nasal and temporal direction. The mean value of both directions was taken to select examples that possess the largest and smallest values in the specific characteristic. The single images show the following characteristics: 5.3a and 5.3b foveal slope with 5.1° and 16.9° respectively, 5.3c and 5.3d foveal bowl area with 0.025 mm² and 0.098 mm² respectively, 5.3e and 5.3f foveal radius with 0.72 mm and 1.23 mm respectively, and 5.3g and 5.3h foveal rim height with 290.4 μm and 392.8 μm respectively.

In the following sections, the data presented in summarised form in Table 5.3 and Table 5.4, will be combined and discussed in different ways to illustrate inter-relationships.

(a) flat foveal slope

(b) steep foveal slope

(c) small foveal bowl area

(d) large foveal bowl area

(e) small foveal radius

(f) large foveal radius

(g) small foveal rim height

(h) large foveal rim height

Figure 5.3: Selected OCT scans to illustrate extreme foveal characteristics. While the left column displays minimal values, the right column shows maximal values of the specified characteristic. From first to last row the pairs demonstrate extreme examples for foveal slope, bowl area, radius and rim height respectively. Each image shows the central OCT scan through the fovea. The mean values (from nasal and temporal direction depicted) of the shown fovea are: for the foveal slope (a) 5.1° and (b) 16.9°, for the foveal bowl area (c) 0.025 mm² and (d) 0.098 mm², for the foveal radius (e) 0.72 mm and (f) 1.23 mm and for the foveal rim height (g) 290.4 μm and (h) 392.8 μm.

5.2.2 *Correlation between right and left eye*

One compelling topic is the correlation between a subject's right and left eye. Regarding a specific research question, it would theoretically be possible to double a studies' sample size by using both eyes of a subject in an analysis. Yet, can these eyes be regarded as statistically independent? Merely the fact that they are from the same person disqualifies them as being as diverse as two eyes from different subjects. On the other hand, there might be research questions that focus on specific problems where corresponding eyes can indeed be regarded as uncorrelated in some sense. In general, an existing correlation between right and left eye of the same subject is often inevitable and therefore, a usage of all eyes in, e.g. a statistical test is not allowed. A detailed discussion about this topic can be found in the work of Armstrong [78].

For the current work, we presumed that a correlation between right and left eyes most likely appears in foveal characteristics which include information about the absolute size. Therefore, the foveal radius r_{fov} and the foveal bowl area A_{bowl} were chosen to compare eyes within the same subject, where right and left eye were both available. Figure 5.4 shows scatter-plots of these correlations and presents with a striking connection between right and left eyes. Both the foveal radius and the foveal bowl area possess high correlations of $r = 0.924$ ($p < .001$) and $r = 0.959$ ($p < .001$) between right and left eyes respectively.

(a) foveal radius ($r = 0.924$)   **(b)** foveal bowl area ($r = 0.959$)
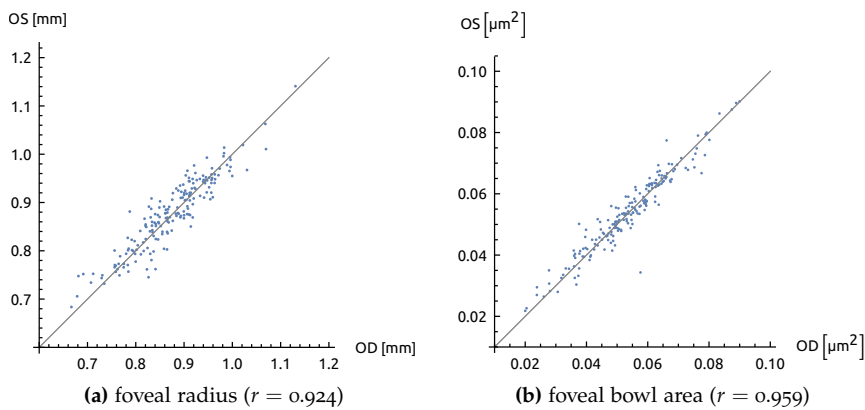
Figure 5.4: Scatterplots for two different foveal characteristics showing the correlation between right (OD) and left (OS) eyes. The plots clearly show that right and left eyes are highly correlated for the foveal radius ($p < .001$) and the bowl area ($p < .001$). Both characteristics are considered to be directly correlated to the overall size of the eye.

The consequence of this is that one has to be extremely cautious when mixing right and left eyes into the same sample group. If in doubt, it is advised to stick to the common rule of using only one eye per subject (e.g. right eye) as it is done in many studies. In the following, the tables and analyses are given for the respective eye independently and when the eye position is not specified, only right eyes were compared.

As we have seen, the foveal radius and the bowl area are valuable characteristics to show inter-subject correlations. However, they have many further application domains and we will outline their importance in the remainder of this section.

Clinically, an exact description and measurement of bowl area is useful in detection of vitreomacular interface pathology, e.g. macular hole development. Different types and stages of macular holes exist, each of which will affect the bowl area parameter, beginning with foveal detachment (stage 1), partial thickness holes (stage 2) and full thickness holes (stage 3). Epiretinal membranes which may develop pseudoholes can also be identified by the bowl area parameter. Potentially, the bowl area parameter can only be measured in early stages, as the model used here can only deal successfully with stage 1 holes (see the general discussion in Chapter 6). This has to be investigated in a subsequent study. However, as the potential key application is early diagnosis of new cases or beginning fellow-eye involvement, the paradigm presented will produce highly accurate results where they are needed most.

Macular holes caused by persistent adherence of the cortical vitreous to the fovea with adjacent vitreoretinal separation, often begin gradually and are associated with visual acuity reduction, metamorphopsia and a central scotoma. Fellow-eye involvement has been shown to affect 21 % of unilateral cases [79] or was shown to newly develop in 13 % of eyes within 48 months [80]. Cross-sectional OCT images provide information on the vitreomacular interface not visible with biomicroscopy. In addition, the OCT has been employed to measure the hole diameter as average of vertical and horizontal diameter, determined at the minimal extent of the hole [81]. In a different application, the OCT is used to identify the anatomical status after macular hole surgery by an *adjusted* hole size parameter which is defined as the ratio between the hole size and the fellow eye's *foveolar floor* size (distance between the boundaries free of ganglion cell layer) [82].

The novel assessment based on model parameters enables scientists and clinicians alike to assess hole formation on a new level of accuracy. The hope is that by quantifying even small deviations from the norm, a better grading and an earlier detection of hole formation is possible.

5.2.3 *Retinal thickness differences between male and female subjects*

CFST has been defined within other populations on the same OCT device. Heussen et al. [15] measured CFST to be 278.9 µm for the device's automatic measurement mode. Wolf-Schnurrbusch and colleagues established 289 µm [18] in their population, while Grover and associates found the CFST to be 271.4 ± 19.6 µm [16]. A difference in retinal thickness between male and female subjects was already reported in different studies [83], however some research findings [84] were potentially established due to confounding factors (e.g. axial length [85]). Previous gender related findings for CFST on the same OCT device also reported smaller thicknesses for women (men: 264.5 ± 22.8 µm and women 253.6 ± 19.3 µm [52], with $p = .0086$). Grover et al. [45] found no gender differences for CFST measured with the SPECTRALIS SD-OCT (men: 273.8 ± 23.0 µm and women 266.3 ± 21.9 µm, with $p = .1$), which can be attributed to insufficient sample sizes.

In this investigation, we established gender differences as depicted in Table 5.4 and Figure 5.5: the CFST is significantly larger in males than in females for both eyes ($p < .001$), but a significant difference in CRT_{min} between different gender could not be found (right eyes $p = .139$, left eyes $p = .308$).

With CRT_{min}, CFST, and h_{rim} (see Table 5.3), a comprehensive comparison of three retinal thickness measures can be given. This leads to a greater

		all	male	female
CFST [µm]	r	277.48 ± 19.817	282.74 ± 20.277	272.12 ± 17.897
	l	277.74 ± 19.702	282.58 ± 20.441	272.74 ± 17.659
CRT_{min} [µm]	r	229.67 ± 18.844	232.02 ± 20.402	227.27 ± 16.875
	l	230.00 ± 18.947	231.81 ± 20.305	228.14 ± 17.343

Table 5.4: The central foveal subfield thickness (CFST) and the minimal central retinal thickness in the fovea (CRT_{min}) both in [µm] given as mean and standard-deviation for all subjects and divided by gender. Each row is split into right (r) and left (l) eyes. While the CFST is significantly larger in males than in females for both eyes ($p < .001$ both), a significant difference in CRT_{min} between different gender could be found (right eyes $p = .139$, left eyes $p = .308$). Note that the gender differences in CFST are still significant even if a correction for axial length was done.

insight, because as depicted in Figure 5.5, foveal rim thickness values can be analysed for different anatomical directions. The Box-Whisker-Plot shows that there are clear differences between directions and that, e.g. temporal rim heights are smaller than in any other directions ($p < .001$ for all in men and women). Regardless of the directional differences, female subjects show significantly smaller h_{rim} values in all four directions ($p = .002$, $p = .006$, $p = .001$, and $p = .03$ for the directions nasal, temporal, inferior and superior respectively).
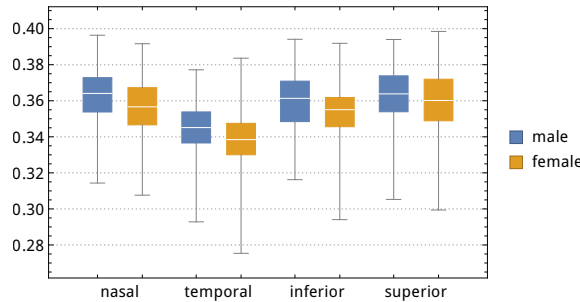
Figure 5.5: Rim height h_{rim} [mm] of male and female subjects divided into the four anatomical directions. Male rim heights are larger than female rim heights in each direction. The nasal, temporal and inferior differences are significant ($p = .002$, $p = .006$, $p = .001$ and $p = .03$ respectively). Noteworthy, in superior direction, the difference is statistically not as strong as in the other directions.

For the first time characteristics like h_{rim} can be calculated for various directions like presented here for nasal, temporal, inferior and superior directions. This sets a precedent in resolving structural variations and since not only the four anatomical directions can be analysed, but virtually every direction, novel findings like shown in Figure 5.7 can easily be investigated.

The relationship of the presented h_{rim} with data in the literature is difficult to establish. A comparison of histology with OCT has been computed previously for a macaque fovea to aid conversion [86], but relative shrinkage is likely to depend on specific fixation and embedding protocols. Besides species specific proportions, individual variations have to be, at least in part, attributed to preceding preparatory influences. When manually measuring a histological fovea section of baboon tissue (Figure 6B in Krebs and Krebs [87]), maximum rim height was 363 µm. For a human fovea, a maximum rim height was measured manually as 320 µm (left side of image) and 333 µm

(right side of image), see Figure 6-91 in Fine and Yanoff [88]. Published OCT data, for example in Figure 1 of [89], gave 379 μm nasally and 347 μm on the temporal side of the horizontal scan depicted. Although this is only an individual scan (healthy subject "S3" of [89], gender or age not given), this data is based on OCT, hereby facilitating comparison to the current data. Differences of this example image to the current model data presented in the next paragraph can be attributed to manual measurement from the published image versus model based computation, alongside individual variation with unknown gender or age information.

In this work, nasally, h_{rim} was 360 μm and significantly larger than temporally with 342 μm ($p < .001$). Men presented with larger maximum rim height compared to women (right eye: nasally 364 μm versus 357 μm with $p = .002$; temporally 345 μm versus 339 μm with $p = .001$).

5.2.4 *Asymmetry of the foveal region*

As already mentioned in the discussion so far, the human fovea is not a round and symmetric structure. When the foveal form along different (anatomical) directions is compared, the fovea presents itself as a highly varying structure that shows clear differences in all investigated characteristics.

(a) foveal radius r_{fov} [mm] **(b)** foveal slope [°]
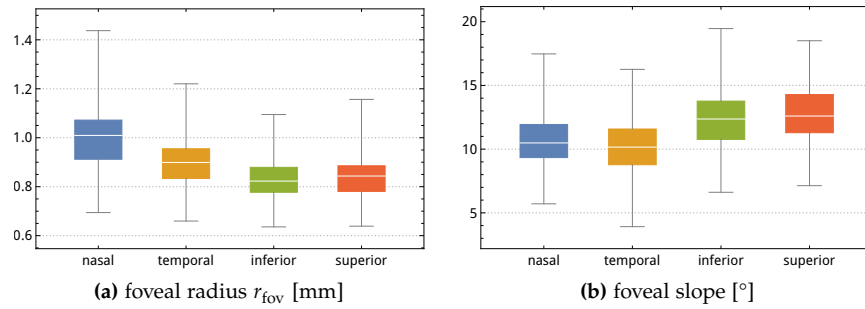
Figure 5.6: Asymmetries of foveal characteristics when viewed for different anatomical directions. The nasal radius is larger than all the other 3 directions ($p < .001$) and the temporal radius is larger than radii in inferior and superior direction ($p < .001$). A difference between the foveal radius in inferior and superior direction could not be shown ($p = .149$). The foveal slope in superior direction is larger than in nasal and temporal direction ($p < .001$ for both), but a significant difference to the inferior direction cannot be shown ($p = .107$).

Figure 5.6 reveals the dependency of foveal radius and slope angle on anatomical directions. The foveal radius is larger in nasal and temporal direction compared to inferior and superior position. This suggests that the fovea has an elliptic form with the larger axis along the nasal to temporal direction. Interestingly, the foveal slope shows a different behaviour as the temporal direction has the smallest slope angle and both inferior and superior angles are clearly larger than the others (*p*-values, see Figure 5.6). This interesting finding can be demonstrated better when taking all modelled directions into account. Figure 5.7 shows a polar plot of the foveal radius and slope for all right eyes. With the current data, it can be shown that the foveal radius is inversely correlated with slope as a steeper slope will lead to a smaller radius and vice versa ($r = 0.408$ with $p < .001$).

One possible explanation for this result is the influence of the nerve fibre layer (NFL) on the retinal thickness which in return influences the foveal slope.

(a) foveal radius [mm]

(b) foveal slope [°]
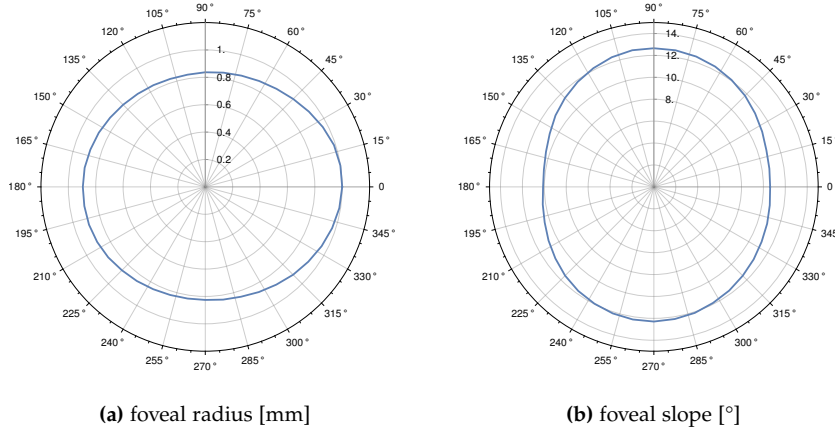
Figure 5.7: Asymmetries of foveal radius and slope in a direct polar plot of all right eyes taking 40 modelled directions into account. Anatomical directions nasal, superior, temporal and inferior are represented by 0°, 90°, 180° and 270° respectively. (a) shows the elliptic form of the foveal radius that has its largest extent along the nasal-temporal axis, although the ellipse appears to be slightly rotated. The foveal slope in (b) shows similar behaviour, where the largest extend is along the inferior-superior axis.

Nerve fibres running radially from the optic nerve towards the fovea arrive at the nasal side. There, they split up to run around the NFL-free zone of the fovea until they are reunited at the temporal side. Whether this hypothesis contains some truth needs to be further investigated and discussed with experts in the field of foveal development.

5.2.5 *Conclusion*

The main goal of this study was to present a detailed and accurate analysis of various fovea characteristics to reveal existing foveal variations and, above all, to expose the highly asymmetric form of foveae. Another purpose was to make the current analysis comparable to existing results which is one reason why commonly used characteristics like CFST were presented. In the case of CFST it was demonstrated that some researchers found similar results [15, 16, 18], while others [52] showed larger differences compared to this study. Previously published significant differences of CFST between men and women were also found. On the other hand, CRT_{min} presented with no gender differences.

The presented results for the foveal slope showed general agreement with the results presented in [51, 52]. The vast improvement of the current results is that now it is possible to give a detailed analysis for various different directions. While Wagner-Schuman and colleagues showed a slope of $12.2 \pm 3.2°$ for men, in this study a great variance of more than 2° could be demonstrated in different anatomical directions (men right eye, nasal: 10.8°, temporal: 10.3°, inferior: 12.6°, superior: 12.9°).

For characteristics like h_{rim}, a comparison to existing literature was difficult as analyses of larger subject groups could not be found. A comparison with histological examples disclosed that such data demonstrates h_{rim} to be about 40 μm smaller [87], while manual measurement of OCT scans presented in a recent work [89] was close to the results presented here. There seems to be a consensus that the nasal h_{rim} is larger than temporal. However, an analysis

as detailed as given in this study, taking all four directions into account, does not seem to exist so far.

Finally, Figure 5.7 presents a way to unleash the full potential of such a detailed multi-directional analysis as described here. It is now not only possible to measure differences in a particular direction, with the method at hand, completely new approaches and insights become available. For instance, Figure 5.7 raises interesting follow-up questions, e.g. how close the presented elliptic form is to a real ellipse and how differences could be explained. Another issue is that the ellipse-like shape seems to be slightly rotated. In the light of the fact that the optic nerve head is towards the upper right position compared to the right eye fovea, one could ask whether the direction of the major axis is connected to the position of the optic nerve head.

5.3   ANATOMICAL REGIONS FOR A CHOROID BOUNDARY ANALYSIS

The aim of this analysis was to develop a method for the detection of the outer choroid boundary (OCB) within OCT images and it has been published in Wagner et al. [70]. The choroid is a vascular structure between the retina and sclera that is primarily responsible for the oxygenation and metabolic activity of the RPE and the outer retina. In OCT images, the visual as well as automated identification of the highly reflective RPE/OCB is easy but the detection of the OCB is much more challenging. The signal of the OCB is weak compared to other layers and background-noise renders it difficult to reliably detect the layer.
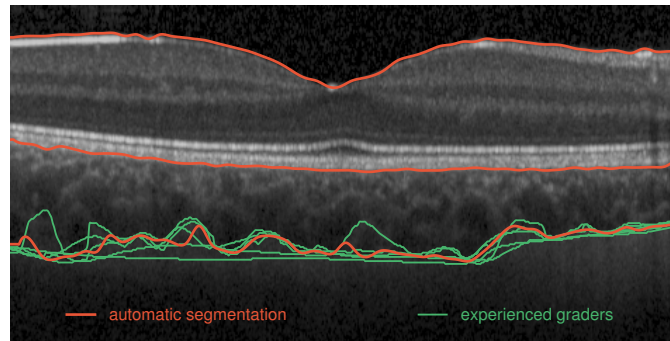
Figure 5.8: Detection of the OCB (as well as ILM and RPE) by the automated algorithm from [70] (red) and the OCB segmentation of five experienced graders (green). The picture shows that the automatic segmentation lies well within the range of the manual graders.

Therefore, the goal was to establish a novel method to detect the OCB in normal OCT images without relying on special imaging modes that enhance the resolution in the choroid. The approach bases on the application of quadratic measure filters within the space functions of bounded variation and works in the noisy and low-signal area of the choroid.

Within this work, the success of the OCB detection method was verified against five manual segmentations to show that the automated approach works well within that inter-operator variance. Figure 5.8 shows an example, where the red lines were automatically detected using the novel approach and the green lines show the OCB segmentation of five experienced graders.

For the analysis of the choroid thickness, which is the distance between RPE and OCB, we aimed to introduce three regions that depend on the anatomy

of the subject's retina. Specifically, we were interested in comparing the highly active foveal region with regions outside this central area. This, however, required knowledge about the foveal structure for each subject and a modelling of all analysed OCT scans to calculate the foveal radii was necessary (see Section 3.3.7). Figure 5.9 shows a visualisation of the regions that were used in the quantification of the choroid thickness.
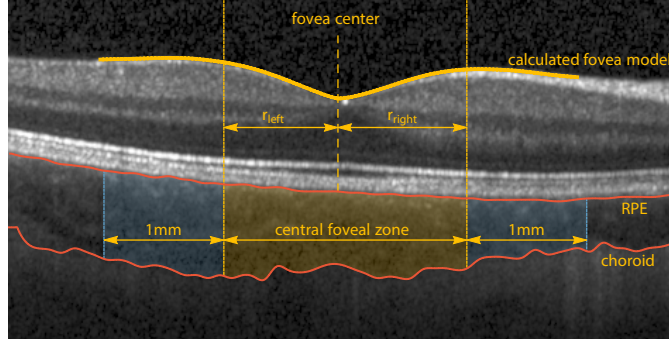
Figure 5.9: Choroid thickness quantification procedure. Inscribed RPE and OCB layers are automatically extracted. ILM layer replaced by foveal model $\mathcal{M}(r)$ left and right from the fovea centre. Based on the fovea model, left and right bowl radius are calculated as described in Equation 3.11. The region between the radii defines an individual central foveal zone for each subject. Additionally, two outer 1 mm-regions are defined which results in three zones where the mean choroid thickness is assessed.

For this work, subjects of the LIFE Child study at Leipzig were employed and OCT data from 50 children (25 male, 25 female) of the ages 8 to 13 have been randomly selected.[1] All 50 OCT scans within this study were modelled successfully with the method presented here and this work shows an application where the fovea model acts as a tool to support a different analysis.

5.4 FOVEAL SHAPE AND THE IMAGE FORMATION IN HUMAN EYES

The aim of this study was an extended and realistic analysis of ray-optical simulations for a comprehensive anatomical eye model [71]. As shown in Section 2.2, historical examinations have been reduced to simple geometrical fovea models derived from postmortem preparations and considered only a few superficial ray propagation aspects. The realistic simulation of the anterior part in this study employed aspherical topographical profiles deduced from in-vivo OCT scans of human foveae. The optical effects of a commonly shaped and an extraordinarily shaped foveal pit were both compared to the analysis of an assumed pure spherical boundary layer.

To perform the simulations, an OCT scan of an eye that presented with an *average foveal shape* was required. Therefore, the detailed model parameter analysis from Scheibe et al. [69] was employed to select median parameters according to Table 5.1. A plot of such an average fovea is shown in Figure 5.10. With the median parameters, the large database of modelled OCT scans was filtered to select a scan which presented with the most common foveal shape.

The ray analysis investigated in the influence of the aperture size, wavelength, and incident angle on the spot size and shape, as well as the axial focal and lateral centroid position. The major result of the study showed a

---

1 The use of data was approved by the institutional review board of the Leipzig Research Center for Civilization Diseases (LIFE).
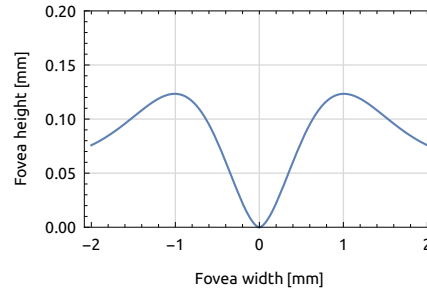
Figure 5.10: Plot of an average fovea using the median parameter values for the right eyes from Table 5.1. Both shapes (left and right of the centre) use the model parameters $\mu = 1.26$, $\sigma = 0.472$, $\gamma = 1.68$ and $\alpha = 0.061$. On the basis of these parameters, an OCT scan was selected which resembles an *average* fovea (see Figure 2 in Frey et al. [71]).

lateral displacement of about 2 µm and an axial shift of the best focal position of less than 4 µm. These findings indicate only small optical effects that are laterally in the range of interreceptor distances and axially less than the photoreceptor outer segment dimension.

5.5 ANALYSIS OF THE FOVEAL DEVELOPMENT OF BIRDS OF PREY

(a) foveal radius ($r = 0.924$)   (b) foveal bowl area ($r = 0.959$)
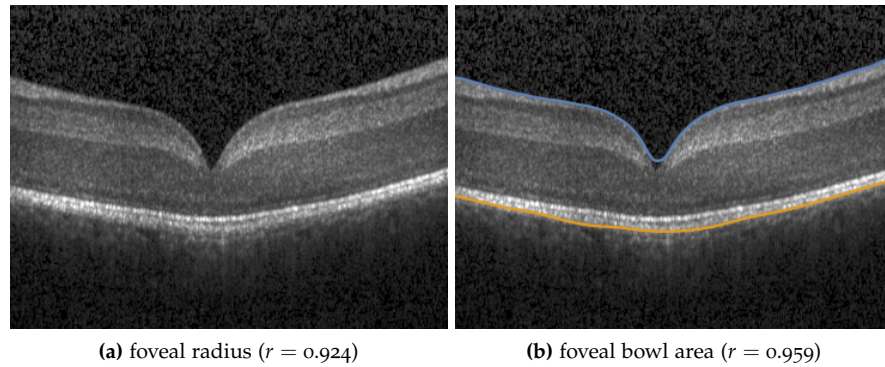
Figure 5.11: OCT of a bird of prey (common kestrel). (a) shows the central B-scan through the funnel-like fovea of the bird. (b) demonstrates the result of the SPECTRALIS SD-OCT layer segmentation which is optimised for human foveal shapes and cannot cope with such an acute pit.

In the beginning of this thesis, we saw that funnel-like foveae accompanied by a superior vision of some birds were one motivation of investigating the function of different foveal shapes. In this unpublished project, we aim to study the development of the kestrel's fovea by applying the model on OCT scans of specimen in different developmental stages. Initial tests showed that the model might be suitable to represent even such unusual foveal shapes to a large degree. However, there are several difficulties to overcome that are unrelated to the model and need a careful consideration.

Figure 5.11 shows an example OCT scan taken from a common kestrel (Falco tinnunculus) with an age of 25 d. If one aims to model the complete three-dimensional structure of its fovea, the major challenge is to acquire an OCT volume scan of high quality. Firstly, it is difficult to fix the view of animals on the target of the OCT device for the time required to take a

complete scan of high resolution. Therefore, the acquired volume will be of a lower resolution than what would be possible with a human subject. But even with reduced resolution to speed up the scanning procedure, the data might contain artefacts where neighbouring sections are misaligned due to rapid movements.

A second difficulty is the layer segmentation algorithm which appears to be optimised for human foveal shapes. Figure 5.11b shows that the method used by the SPECTRALIS SD-OCT software makes assumptions about the smoothness of layers and is not able to successfully extract the pointy foveal centre.

Using the SPECTRALIS SD-OCT's software, it is possible to manually re-align incorrectly segmented layers to some degree. However, it appears that the program uses splines which also enforce smoothness in the results and therefore correcting the layer for a funnel-like fovea becomes a time-consuming task.

Figure 5.12 shows the result of modelling the shown example after manually correcting the ILM layer. The RMS errors of both left and right fit is smaller than 10^{-5} mm and the model representation shows an excellent alignment with the data.
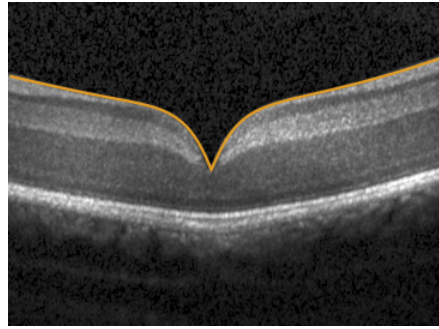
Figure 5.12: Result of modelling a kestrel OCT. Since the OCT device's layer segmentation algorithm was unsuccessful at the pointy foveal centre, the ILM segmentation was manually corrected. The fitting error was 6.18×10^{-6} mm and 4.12×10^{-6} mm for the left and right side respectively. Model parameters for the left and the right side are $\mu = 4.3011$, $\sigma = 0.2225$, $\gamma = 1.062$, and $\alpha = 0.1871$ and $\mu = 4.1022$, $\sigma = 0.2947$, $\gamma = 1.1112$, and $\alpha = 0.1873$ respectively.

Noteworthy is the value of the γ parameters shown in Figure 5.12. Although the other parameters deviate as well from the ones present in a human fovea (see Table 5.1), the purpose of the γ parameter is to adjust the foveal shape between the concaviclivate forms of humans and convexiclivate forms as in the shown example. Therefore, while human foveae have a γ value around 1.7, the extreme form shown here is close to the lower limit of $\gamma = 1$. This, however, raises the question if the lower limit of γ is justified for such extreme foveae like the one we have seen here. Since the lower bound of γ ensures the validity of certain model characteristics, a careful re-evaluation of the consequences for the analytic results presented in Chapter 3 is required.

Summarising, applying the model to deep, funnel-like foveae is feasible. To ensure correct outcomes, the OCT layer segmentation algorithm needs to be replaced by a custom implementation that can handle the acute foveal pit. Since we already worked on a similar method for detecting the outer choroid boundary, an extension of this method for the ILM and RPE boundary looks promising [70].

6

GENERAL DISCUSSION

In this thesis, we presented a concise parametric model for foveal shapes. Starting from a historical review of the matter to motivate the interest in form and function of foveae, we examined recent publications and showed how optical coherence tomography (OCT), a modern in-vivo imaging technique, opened the doors for a deeper investigation of foveal shapes. After discussing strengths and weaknesses of earlier fovea models, we derived a suitable model function and investigated its mathematical properties. Opposed to previous works, the chosen model is only able to represent the shape of one foveal direction starting from its centre. To reproduce the complex and asymmetric shape of an entire three-dimensional fovea, a unique radial fitting approach was introduced which combines several fits in different directions from the foveal centre outwards. This method has several compelling advantages. Firstly, the parametric model function remains simple and allows for the symbolic calculation of, e.g. derivatives, antiderivatives and limits. Therefore, deduced fovea characteristics were calculated symbolically in almost all cases. Secondly, the radial fitting allows for the representation of a wide range of foveae without employing complicated expressions to account for asymmetries. Since all directions are fitted with the same model function, it is possible to compare different directions within the same fovea, and asymmetries can be quantified in terms of model parameters. Therefore, it is possible to analyse exactly how, e.g. the foveal pit radius or its steepness differ within distinct anatomical directions and the results in Section 5.2.4 showed valuable findings that were not possible before. Finally, one major advantage of the proposed method is its flexibility. Although we showed that the parametric model works for a wide range of foveal shapes, it might not be able to account for all possible foveae. However, the radial fitting is not bound to a specific model function. As shown by Yadav et al. [59], the radial fitting can be employed with different model functions which are more appropriate in certain situations.

After introducing the theoretical foundation of the model, we presented information about important implementation details. The aim of this chapter was to give as much guidance as possible to ensure that the presented methods can be reproduced and extended in the future. Although we employed one particular OCT device throughout this work, i.e. the SPECTRALIS SD-OCT (Heidelberg Engineering), we have tried to convey general remarks wherever possible to allow for an adaption to different OCT devices. Additionally, we inspected certain aspects of how the implementation can be optimised for speed which included details of the employed Differential Evolution (DE) algorithm and the parallelisation of the method on different levels.

Since its introduction, the parametric fovea model has proven its practicality in several projects and the results of selected applications have been shown and discussed in Chapter 5. In this chapter, we present a general

discussion of aspects that have so far only been outlined or not considered at all.

Regarding the first step in the modelling approach, i.e. the acquisition of OCT data, we already presented a detailed list in Section 5.1 highlighting common sources of error during the scanning procedure. High quality OCT scans ensure that the retinal layers can be extracted successfully and, therefore, a modelling of the fovea is feasible. However, even with an experienced OCT operator, the compliance of the scanned subject is of crucial importance because movements of the eye during the scan can introduce artefacts in acquired data. This problem was already pointed out by Dubis, McAllister, and Carroll [50]:

> One of the problems with reconstructing foveal volumes from time-domain OCT is eye movement. Even in individuals with superior fixation stability, small saccades occur that can disrupt the ability to automatically model the pit contour. Thus, aligning scans from within the fast mac dataset is an important first step in reconstructing foveal morphology.

The advance of OCT technology and the improvement of eye tracking, scanning speed and automatic alignment makes a post-processing of this kind often obsolete. However, in subjects like animals, the eye movement can still be problematic. To illustrate the matter, Figure 6.1 shows a colour-representation of the retinal thickness map for OCT scans of a kestrel and an adult human. Note that since the thickness map uses the relative difference between two layers of the same B-Scan, misalignments between neighbouring sections are of second concern. Still, the left image of the kestrel's OCT presents with more colour-inconsistencies indicating that the eye movement of the bird during the scanning procedure affected the quality of the result. The right image of the human scan presents with a large degree of coherence, although this scan used a higher resolution with over 130.000 A-scans compared to the kestrel with only about 50.000 A-scans. Consequently, the scan of the human fovea took considerably longer but the compliance of an adult to keep a steady fixation during the procedure ensured a better quality. The fixation-problem is not restricted to scans of animals. Experience shows that young children and elderly might also present with a lower time span of concentrating on the fixation target. Therefore, in the design of larger studies using subjects such as children, elderly or animals, a careful assessment of the scan protocol is important to balance resolution and introduced artefacts.

Another aspect that is of concern when working with eyes of children or animals are the scaling factors necessary to calculate the size of the OCT data in metric units along the B- and C-scan direction. Although we worked exclusively with the SPECTRALIS SD-OCT, this discussion can be generalised to any OCT device.

In order to transform the shift of the OCT laser between different A-scans to a deviation in metric units on the retina, OCT devices use a theoretical eye-model underneath that makes certain assumptions about the size of the eye, refraction of the cornea and other anatomical properties. The SPECTRALIS SD-OCT in particular uses an adapted version of Garway-Heath et al. [77] to calculate the scaling-factors from the first cornea anterior radius and the refractive error.[1] All other properties of the employed adult human eye-model are assumed to be invariable. For eyes, like the ones of children or animals, which deviate substantially in size or anatomy from an adult human eye, the

---

1 Personal communications with Heidelberg Engineering
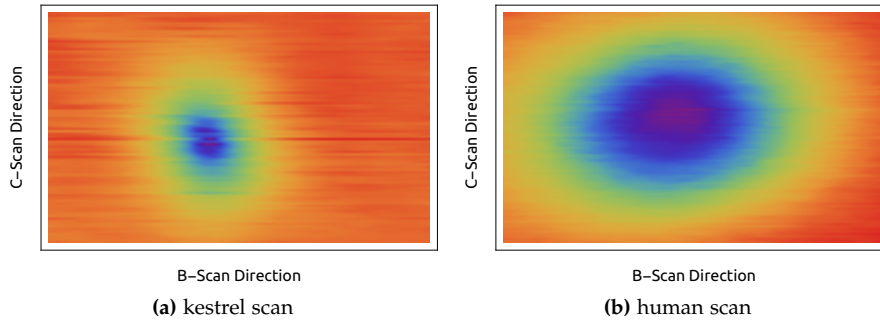
Figure 6.1: Quality comparison between the OCT scan of a common kestrel and an adult human subject. Images show the retinal thickness of 90 B-scans in the foveal region. Colour differences indicate different retinal heights ranging from purple for small values to red for larger values. Visible B-scan line patterns in (a) indicate scanning artifacts due to the eye movement of the animal. These are present at a much smaller degree in (b) due to the steady fixation of an adult during the procedure.

assumptions of the underlying eye-model might be incorrect. Therefore, one has to be careful when drawing conclusions from measurements that use the metric units provided by the device in such situations. More importantly, since all fovea modelling approaches rely on this scaling, the characteristics of the model shapes are prone to the same errors.

In the case of the SPECTRALIS SD-OCT, the corneal radius and the refractive error of the scanned subject are required for the calculation of the scaling factors. The radius of the cornea has to be specified by the operator or otherwise a (possibly incorrect) default value will be used. However, the refractive error is estimated from the focus setting during the scan. This scan focus can be adjusted to ensure a sharp scanning laser ophthalmology (SLO) image and our investigations show that this setting is employed as refractive error in the Garway-Heath et al. formula to calculate the scaling factor. However, especially children and young subjects possess the ability to focus on a wide range of distances and it is possible that they compensate for a wrong focus setting by accommodation. This means that the operator gets a sharp SLO image and might not notice that the focus setting does not represent the correct refractive error. Therefore, the wrong setting for the scan focus might go unnoticed and can result in an incorrect calculation of the true sizes.

To understand the calculation of the scaling factors and to investigate this issue, we have performed several experiments using one of our colleagues as a test-subject (female, age 34, no visual correction). One of the experiments is shown in Figure 6.2 where we acquired two scans of the same foveal region but used different focus settings of 2.09 dpt and −3.49 dpt. The two settings represent two extreme values for which the subject was still able to focus correctly on the fixation target of the OCT device, and, therefore, creating a sharp SLO image on the operator's monitor. In the overlay of the SLO images of both scans in Figure 6.2a, only a slight shift is visible, but the size of the region appears to be the same because the vessel structure of the images are accurately aligned. However, extracting the metric size of both SLO images from the meta-data of the scans, the device claims that the sides of the image for 2.09 dpt and −3.49 dpt are 8.55 mm and 9.39 mm respectively. Similarly, Figure 6.2b shows the central B-scan for both datasets and includes two lines which roughly indicate the boundary of the foveal pit. Again, both B-scans

seem to be aligned and there is no indication that one of them represents a larger region. However, the reported widths of the B-scans are 4.28 mm and 4.69 mm for the upper and lower image respectively which is the same relative difference as already seen in the SLO images.

(a) Overlay of two SLO images   (b) OCT scan comparison
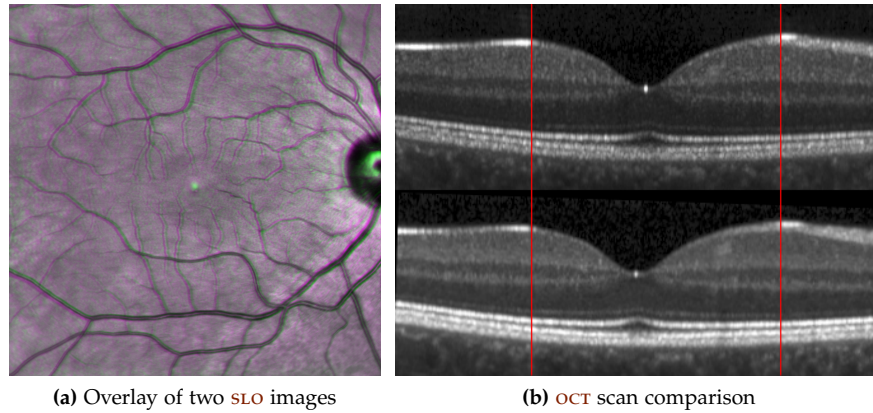
Figure 6.2: Influence of accommodation on OCT scaling factors by using different focus settings (2.09 dpt and −3.49 dpt) on the same subject and foveal region. Figure (a) is an overlay of the SLO images of both scans and shows differences as colours. The small coloured seams around the vessels indicate a high degree of alignment of both scans. Figure (b) shows the central region of both scans and the red lines roughly indicate the end of the foveal pit. While there are no obvious visual differences between both scans, the SPECTRALIS SD-OCT reports the width of the B-scans in Figure (b) as 4.28 mm and 4.69 mm for the upper and lower image respectively.

The relative difference in size between the scans is about 10 %. Although we presented two extreme cases, where the test-subject actively focused, it is unclear to which extent this issue appears in real experiments. Since even recent fovea models [59] rely on a correct scaling, an investigation of the black-box algorithms of the OCT device is necessary. However, with the awareness of this issue, it is already possible to improve the situation. First, it might be possible to recalculate correct scaling factors from exact measurements the eye's properties when the underlying eye-model and formula used by the OCT device is known. Secondly, standard operating procedures (SOPs) for the operators of the OCT devices can be adjusted accordingly. Within our group, we took the following steps:

- Measurements of refractive error and corneal radius are acquired before the actual OCT scan.

- The initial setting for the scan focus has to be adjusted to the correct refractive error. This gives the subject the opportunity to see the fixation target with an appropriate initial setting and the operator can then make adjustments to ensure a sharp SLO image.

- The operator inputs the correct corneal radius into the scan profile.

For eyes of different size (children) or anatomy, there is to the knowledge of the author no adequate solution. However, our group has started to use 3D printing to build a phantom eye with an inscribed grid of known dimensions on the retina. This approach might help to compare OCT scans with a known ground truth. A detailed analysis of these results will help to understand how trustworthy the measurements of specific OCT devices are.

Like most other fovea models, the approach presented here uses the retinal thickness extracted from the OCT scan instead of employing the volume data directly. As already mentioned, the SPECTRALIS SD-OCT provides the retinal layer positions from which the foveal thickness map can be calculated. Since other OCT devices might not provide such a feature, the two required retinal layers, i.e. the inner limiting membrane (ILM) and the retinal pigment epithelium (RPE), need to be segmented from the grey-level volume data of the scan. In contrast to other retinal layers that are not as clearly distinguishable, for the extraction of the ILM and RPE boundary a large variety of scientifically documented methods is available by now. These include de-noising by diffusion and subsequent edge detection [90], de-noising and simultaneous edge detection by variational methods [91], active contour methods [92], graph-theoretical approaches [93–96] and classification by support vector machines [97]. Furthermore, in [98] a statistical segmentation method was proposed, which is essentially based on the application of a neural network. In addition to the methods above, our group worked on the recognition of the outer choroid boundary. This approach can be adapted to extract the ILM and RPE boundary [70].

One limitation of the presented model and parametric models in general (e.g. [50, 53, 59]) is the representation of pathological foveae. Degenerations like macular holes which tear the retina apart cannot be modelled, because the tissue boundary between vitreous and retina (which was the ILM) often present with folds and is highly irregular. A bijective model function that requires a one-to-one correspondence between position and the foveal thickness is not able to account for such situations. In addition, an accurate computation of the fovea centre necessary for the radial modelling might no longer be possible. Thus, even with a free-form model function that can represent highly irregular shapes, we advise against the use of the radial fitting procedure. We suspect that in such cases an assessment of the exact shape is of minor interest. Approaches like the one presented by Ding et al. [55], which quantify the degree of irregularity or allow for a discrimination of different levels of severity, are superior in such cases.

However, when working with healthy foveae, the combination of radial fitting with the presented parametric model has been shown to perform exceptionally well for a large range of possible foveal shapes. The mathematical structure of the model function is particularly appealing as it allows for an analytic inspection of its properties and a determination of symbolic solutions for foveal characteristics. If, however, the flexibility of the parametric model is indeed insufficient to accurately fit foveal shapes of, e.g. non-human eyes then the approach presented here is still of great value. By replacing the parametric model with a different function, the radial fitting method can serve as a flexible approach that has been proven to work reliably, is easy to implement and can be parallelised.

7

OUTLOOK

In this short outlook, we want to elaborate on future goals to enlarge the modelling approach and to make it accessible to a larger scientific audience. One crucial part between the raw optical coherence tomography (OCT) scan and the modelling is the computation of the retinal thickness map for the scan. This computation relies on an accurate detection of the retinal pigment epithelium (RPE) and inner limiting membrane (ILM) layer within the data. However, entrusting the OCT vendors to provide these segmentations can be problematic for several reasons. Firstly, the underlying algorithms for the segmentation are not publicly available which has an impact on the reproducibility of scientific research using these methods. Secondly, the layer segmentation might give different results for different OCT manufacturers if the layers are provided at all. Therefore, one future goal is to implement the layer segmentation independently from the employed OCT device. As already discussed, existing work for the detection of the outer choroid boundary (OCB) will serve as an excellent basis which can be extended to recognise the required ILM and RPE boundary [70, 99]. This leads to a scientifically documented algorithm, independent of proprietary OCT software.

Similarly, the usage of Wolfram *Mathematica* as a high-level language to implement the algorithms was an excellent choice since it contains many functions for symbolic and numeric computations that were convenient during the development. However, to target a larger scientific audience, the implementation should be made available in one of the popular languages like C++, Java, Python or Julia.

As already discussed in the last chapter, another disadvantage of a *black-box* OCT device is that it is not evident, how accurate the mapping from OCT pixel coordinates to metric units is. In Wagner et al. [70], we already used an adapted version of Garway-Heath et al. [77] to calculate the pixel width in millimetre because the required eye-specific information of the subjects was available. A custom-made dummy eye with properties similar to real eyes might help to uncover what exactly is imaged and what types of distortions are present in a specific OCT-device. In collaboration with the research group of Mike Francke, the exploration of such a dummy eye using state-of-the-art 3D printing technology has already been started. The key feature of the dummy eye is an accurate measurement grid at the back of the eye which allows for an exact comparison between the grid visible in the OCT scan and its known dimensions. Such an approach would lead to a higher confidence in the measured dimensions when scanning eyes of different sizes or species. Currently, the correctness of the metric dimensions should not be taken for granted and an approach for the calculation of correct pixel sizes would lead to an improvement for any OCT-based analysis and for the foveal modelling in particular.

The strength of the presented model approach, however, is not entirely the flexible parametric equation but the method of modelling an OCT dataset radially around the centre of the fovea. This scheme has already been picked up by Yadav et al. [59] who used cubic Bézier functions to represent the foveal shape. Generalising this idea, another future goal is to extend the fovea modelling approach to different types of underlying model functions. This increases its value in situations where a parametric model is too restrictive and cannot represent a particular foveal shape. Therefore, a public framework which allows for the selection of predefined models or the definition of custom model functions and which uses the radial fitting procedure would be of great value for the eye research community.

MATHEMATICAL DETAILS

Throughout this thesis, derivatives and the antiderivative of the model equation

$$\mathcal{M}(r; \mu, \sigma, \gamma, \alpha) = \underbrace{\mu \sigma^2 r^\gamma \cdot \exp\left(-\mu r^\gamma\right)}_{A} + \underbrace{\alpha \left(1 - \exp\left(-\mu r^\gamma\right)\right)}_{B} \tag{A.1}$$

were employed to prove properties or calculate characteristics. Nevertheless, details of these calculations were omitted as it would have drawn the attention away from the major aspects. Below, we will present all necessary steps and details required for the calculation of formulas that were employed.

To find the derivatives of Equation A.1, only basic rules, like the *chain rule*, are required and although expressions might become large, no deep math is involved. As the derivative of $\exp(-\mu r^\gamma)$ will be used several times, note that it is calculated using the chain rule

$$\exp(f(r))' = \exp(f(r)) \cdot f'(r) \tag{A.2}$$

which leads to

$$\partial_r \exp(-\mu r^\gamma) = -\mu r^{\gamma-1} \exp(-\mu r^\gamma). \tag{A.3}$$

A.1 FIRST DERIVATIVE $\partial_{rr} \mathcal{M}(r)$

The two parts, A and B, of Equation A.1 can be derived separately and put back together

$$\partial_r A = \left(\partial_r \mu \sigma^2 r^\gamma\right) \cdot \exp\left(-\mu r^\gamma\right) + \mu \sigma^2 r^\gamma \cdot \left(\partial_r \exp\left(-\mu r^\gamma\right)\right) \tag{A.4}$$

$$= \gamma \mu \sigma^2 r^{\gamma-1} \exp\left(-\mu r^\gamma\right) - \gamma \mu^2 \sigma^2 r^{2\gamma-1} \exp\left(-\mu r^\gamma\right), \tag{A.5}$$

$$\partial_r B = \alpha \gamma \mu r^{\gamma-1} \exp\left(-\mu r^\gamma\right). \tag{A.6}$$

In the final form $\partial_r \mathcal{M} = \partial_r A + \partial_r B$, several terms can be collected to give a more concise expression

$$\partial_r \mathcal{M} = \alpha \gamma \mu r^{\gamma-1} \exp\left(\mu\left(-r^\gamma\right)\right) - \tag{A.7}$$

$$\gamma \mu^2 \sigma^2 r^{2\gamma-1} \exp\left(\mu\left(-r^\gamma\right)\right) + \tag{A.8}$$

$$\gamma \mu \sigma^2 r^{\gamma-1} \exp\left(\mu\left(-r^\gamma\right)\right) \tag{A.9}$$

$$= \gamma \mu r^{\gamma-1} \exp\left(\mu\left(-r^\gamma\right)\right) \left(\alpha + \sigma^2 \left(1 - \mu r^\gamma\right)\right). \tag{A.10}$$

A.2   SECOND DERIVATIVE $\partial_{rr} \mathcal{M}(r)$

For the calculation of the second derivative, Equation A.10 is the starting point which consists of three factors, each dependent on r

$$C = \gamma \mu r^{\gamma-1}, \tag{A.11}$$
$$D = \exp\left(-\mu r^\gamma\right), \tag{A.12}$$
$$E = \alpha + \sigma^2 \left(1 - \mu r^\gamma\right), \tag{A.13}$$

and therefore the second derivative will have the form

$$(C \cdot D \cdot E)' = D \cdot E \cdot C' + C \cdot E \cdot D' + C \cdot D \cdot E'.$$

With the help of Equation A.3, we only need to take care of C and E and the calculation of the required three derivatives gives

$$\partial_r C = (\gamma - 1)\gamma \mu r^{\gamma-2}, \tag{A.14}$$
$$\partial_r D = \gamma \mu \left(-r^{\gamma-1}\right) \exp\left(\mu\left(-r^\gamma\right)\right), \tag{A.15}$$
$$\partial_r E = \gamma \mu \sigma^2 \left(-r^{\gamma-1}\right). \tag{A.16}$$

Substituting these results and simplifying the expression gives the second derivative as

$$\partial_{rr}\mathcal{M}(r) = \gamma \mu r^{\gamma-2} \exp\left(\mu\left(-r^\gamma\right)\right) \cdot$$
$$\left(\alpha\left(\gamma - \gamma \mu r^\gamma - 1\right) + \sigma^2\left(\mu r^\gamma + \gamma\left(\mu r^\gamma\left(\mu r^\gamma - 3\right) + 1\right) - 1\right)\right). \tag{A.17}$$

A.3   THIRD DERIVATIVE $\partial_{r^3} \mathcal{M}(r)$

The calculation of the third derivative is similar to the one for the second derivative. Equation A.17 consists of three factors that need to be derived and assembled into the final form. We omit the details here and solely present the result

$$\partial_{r^3} \mathcal{M}(r) = \gamma \mu r^{\gamma-3} \exp\left(\mu\left(-r^\gamma\right)\right) \cdot$$
$$\left[(\gamma - 2)(\gamma - 1)\left(\alpha + \sigma^2\right) + \gamma \mu^2 r^{2\gamma}\left(\alpha\gamma + 3(2\gamma - 1)\sigma^2\right) - \right.$$
$$\left. \gamma^2 \mu^3 \sigma^2 r^{3\gamma} - (\gamma - 1)\mu r^\gamma\left(3\alpha\gamma + (7\gamma - 2)\sigma^2\right)\right]. \tag{A.18}$$

A.4   ANTIDERIVATIVE OF $\mathcal{M}(r)$

Lemma 7. *Assuming $\gamma > 0$ and using the incomplete Gamma-function $\Gamma(a, x)$ (see [64, p. 81]) defined as*

$$\Gamma(a, x) = \int_x^\infty \exp(-t) \cdot t^{a-1}\, \mathrm{d}t,$$

the integral of the model function is given by

$$\int \mathcal{M}(r)\, \mathrm{d}r = \frac{\alpha r \left(\mu r^\gamma\right)^{-1/\gamma} \Gamma\left(\frac{1}{\gamma}, r^\gamma \mu\right)}{\gamma} -$$
$$\frac{\mu \sigma^2 r^{\gamma+1} \left(\mu r^\gamma\right)^{-\frac{\gamma+1}{\gamma}} \Gamma\left(1 + \frac{1}{\gamma}, r^\gamma \mu\right)}{\gamma} + \alpha r. \tag{A.19}$$

Proof. We prove the correctness of the antiderivative by deriving the found expression with respect to r and simplifying it to the original model function. First, we note that the derivative of $\Gamma(a, f(r))$ is given by

$$\partial_r \Gamma(a, f(r)) = -\exp(-f(r)) f(r)^{a-1} f'(r), \tag{A.20}$$

and, therefore, the derivatives for the two terms involving Γ can be calculated and simplified to

$$\partial_r \Gamma(\frac{1}{\gamma}, r^\gamma \mu) = -\frac{\gamma (\mu r^\gamma)^{\frac{1}{\gamma}} \exp(\mu(-r^\gamma))}{r}, \tag{A.21}$$

$$\partial_r \Gamma(1 + \frac{1}{\gamma}, r^\gamma \mu) = -\frac{\gamma (\mu r^\gamma)^{\frac{1}{\gamma}+1} \exp(\mu(-r^\gamma))}{r}. \tag{A.22}$$

Using above identities, we can derive each term in the sum of the antiderivative separately. For the first term, this gives

$$\partial_r \left(\frac{\alpha r (\mu r^\gamma)^{-1/\gamma} \Gamma\left(\frac{1}{\gamma}, r^\gamma \mu\right)}{\gamma} \right) = -\alpha \exp(\mu(-r^\gamma))$$

$$- \frac{\alpha \mu r^\gamma (\mu r^\gamma)^{-\frac{1}{\gamma}-1} \Gamma\left(\frac{1}{\gamma}, r^\gamma \mu\right)}{\gamma} + \frac{\alpha (\mu r^\gamma)^{-1/\gamma} \Gamma\left(\frac{1}{\gamma}, r^\gamma \mu\right)}{\gamma}$$

$$= -\alpha \exp(\mu(-r^\gamma)). \tag{A.23}$$

Note that the two rational terms simplify to zero when expanding the exponent of μr^γ in the first one. For the second term, we get a similar result which can be simplified:

$$\partial_r \left(-\frac{\mu \sigma^2 r^{\gamma+1} (\mu r^\gamma)^{-\frac{\gamma+1}{\gamma}} \Gamma\left(1 + \frac{1}{\gamma}, r^\gamma \mu\right)}{\gamma} \right) =$$

$$\mu^2 \sigma^2 r^{2\gamma} (\mu r^\gamma)^{\frac{1}{\gamma}-\frac{\gamma+1}{\gamma}} \exp(\mu(-r^\gamma))$$

$$- \frac{(\gamma+1)\mu \sigma^2 r^\gamma (\mu r^\gamma)^{-\frac{\gamma+1}{\gamma}} \Gamma\left(1 + \frac{1}{\gamma}, r^\gamma \mu\right)}{\gamma}$$

$$+ \frac{(\gamma+1)\mu^2 \sigma^2 r^{2\gamma} (\mu r^\gamma)^{-\frac{\gamma+1}{\gamma}-1} \Gamma\left(1 + \frac{1}{\gamma}, r^\gamma \mu\right)}{\gamma}$$

$$= \mu \sigma^2 r^\gamma \exp(\mu(-r^\gamma)). \tag{A.24}$$

The last term of the antiderivative is given by $\partial_r \alpha r = \alpha$ and, therefore, we can show that the final result simplifies to the original model function

$$\partial_r \int \mathcal{M}(r) \, dr = \mu \sigma^2 r^\gamma \exp(\mu(-r^\gamma)) - \alpha \exp(\mu(-r^\gamma)) + \alpha \tag{A.25}$$

$$= \mu \sigma^2 r^\gamma \cdot \exp(-\mu r^\gamma) + \alpha(1 - \exp(-\mu r^\gamma)). \tag{A.26}$$

$\square$

Note that Rich, Scheibe, and Abbasi [100] worked on *Rubi*, an open-source system for rule-based, symbolic integration which is capable to show detailed steps necessary to find antiderivatives for symbolic expressions. In the case of the model function, the Rubi rules 2.3.2.1.2 and 2.3.2.2.1.2.2 are crucial as

they are necessary to integrate the appearing exponential terms of the model function.[1] The first rule 2.3.2.1.2 is used to find

$$\int \exp\left(-\mu r^\gamma\right) dr = -\frac{r\left(\mu r^\gamma\right)^{-1/\gamma} \Gamma\left(\frac{1}{\gamma}, r^\gamma \mu\right)}{\gamma} \tag{A.27}$$

and the second rule 2.3.2.2.1.2.2 is used to find

$$\int \exp\left(-\mu r^\gamma\right) \cdot r^\gamma\, dr = -\frac{r^{\gamma+1}\left(\mu r^\gamma\right)^{-\frac{\gamma+1}{\gamma}} \Gamma\left(1+\frac{1}{\gamma}, r^\gamma \mu\right)}{\gamma}. \tag{A.28}$$

These identities can be verified by derivation and were used to calculate the antiderivative of the model function.

A.5 VOLUME OF A CIRCULAR SECTOR V_i

At the end of Section 3.3.4, the computation of central foveal subfield thickness (CFST) employed a symbolic solution of the volume sector

$$V_i = \varphi_d \int_0^{r_{\text{CFST}}} r \cdot \mathcal{M}_i(r)\, dr. \tag{A.29}$$

To calculate the definite integral, the antiderivative of

$$\int r \cdot \mathcal{M}(r)\, dr =$$
$$\int \mu \sigma^2 r^{\gamma+1} \exp\left(\mu\left(-r^\gamma\right)\right) - \alpha r \exp\left(\mu\left(-r^\gamma\right)\right) + \alpha r\, dr \tag{A.30}$$

is required which can be found similarly to the antiderivative of the model function. The key is the Rubi rule 2.3.2.2.1.2.2 shown in Equation A.28 which can be generalised to capture both terms involving the exponential in above integral:

$$\int r^\lambda \exp\left(\mu\left(-r^\gamma\right)\right) dr = -\frac{r^{\lambda+1}\left(\mu r^\gamma\right)^{-\frac{\lambda+1}{\gamma}} \Gamma\left(\frac{\lambda+1}{\gamma}, r^\gamma \mu\right)}{\gamma}. \tag{A.31}$$

Using $\lambda = \gamma + 1$ and $\lambda = 1$, the antiderivative of the integral A.30 can be determined as

$$\int r \cdot \mathcal{M}(r)\, dr = \frac{\alpha r^2}{2} - \frac{\mu \sigma^2 r^{\gamma+2}\left(\mu r^\gamma\right)^{-\frac{\gamma+2}{\gamma}} \Gamma\left(\frac{\gamma+2}{\gamma}, r^\gamma \mu\right)}{\gamma} +$$
$$\frac{\alpha r^2\left(\mu r^\gamma\right)^{-2/\gamma} \Gamma\left(\frac{2}{\gamma}, r^\gamma \mu\right)}{\gamma}. \tag{A.32}$$

The correctness of the antiderivative can be verified by deriving and simplifying it back to the original form $r \cdot \mathcal{M}(r)$. The final step to determine the definite integral is the calculation of the limits at the integration boundaries. For $r_{\text{CFST}} > 0$, the limit at r_{CFST} from below can be determined as

$$\lim_{r \to r_{\text{CFST}}-} \int r \cdot \mathcal{M}(r)\, dr =$$
$$\frac{\alpha r_{\text{CFST}}^2}{2} - \frac{\sigma^2 \mu^{-2/\gamma} \Gamma\left(\frac{\gamma+2}{\gamma}, r_{\text{CFST}}^\gamma \mu\right)}{\gamma} + \frac{\alpha \mu^{-2/\gamma} \Gamma\left(\frac{2}{\gamma}, r_{\text{CFST}}^\gamma \mu\right)}{\gamma} \tag{A.33}$$

---

1 See the section *Rules* on https://rulebasedintegration.org for details about their derivation.

and the limit at 0 from above can be determined as

$$\lim_{r \to 0+} \int r \cdot \mathcal{M}(r) \, dr = \frac{\alpha \mu^{-2/\gamma} \Gamma\left(\frac{2}{\gamma}\right)}{\gamma} - \frac{\sigma^2 \mu^{-2/\gamma} \Gamma\left(\frac{\gamma+2}{\gamma}\right)}{\gamma}. \tag{A.34}$$

Subtracting both results and simplifying appearing terms leads directly to the formula for V_i presented in Equation 3.5 on page 29.

B

ABBREVIATIONS

API application programming interface

CAS computer algebra system

CPU central processing unit

DE Differential Evolution

DOG difference of Gaussians

FAZ foveal avascular zone

CFST central foveal subfield thickness

CPT central point thickness

CRT central retinal thickness in the fovea

CRT_{min} minimal central retinal thickness in the fovea

ETDRS Early Treatment Diabetic Retinopathy Study Research Group

FCS foveal central subfield

ILM inner limiting membrane

IPP Intel Integrated Performance Primitives

IRL inner retinal layers

MKL Intel Math Kernel Library

NFL nerve fibre layer

OCT optical coherence tomography

ONL outer nuclear layer

OCB outer choroid boundary

RMS root mean square

RPE retinal pigment epithelium

SIMD single-instruction, multiple data

SLO scanning laser ophthalmology

SOP standard operating procedure

SPG Sloped Piecemeal Gaussian

[1]   Ida C. Mann. *The Development of the Human Eye*. 1st ed. London: Cambridge University Press, 1928.

[2]   Gordon L. Walls. *The vertebrate eye and its adaptive radiation*. Vol. 100. Bloomfield Hills, Mich., Cranbrook Institute of Science, Aug. 1942, p. 818. DOI: 10.5962/bhl.title.7369.

[3]   Jörg Trotter. *Das Auge: ein Handbuch für Augenoptiker*. Optik-Verlag, Jan. 1994. ISBN: 978-3922269397.

[4]   Virginia L. Taylor, Kristin J. Al-Ghoul, Wesley Lane, Andrew Davis, Jerome R. Kuszak, and Martin J. Costello. „Morphology of the normal human lens." In: *Investigative Ophthalmology & Visual Science* 37.7 (July 1996), p. 1396. DOI: 10.1016/S0002-9394(14)72090-2.

[5]   Russell G. Foster, Ignacia Provencio, David Hudson, Stuart Fiske, Willem J. Degrip, and Michael Menaker. „Circadian photoreception in the retinally degenerate mouse (rd/rd)." In: *Journal of Comparative Physiology A* 169.1 (July 1991), pp. 39–50. DOI: 10.1007/bf00198171.

[6]   Denis A. Baylor, Trevor D. Lamb, and King-Wai Yau. „Responses of retinal rods to single photons." In: *The Journal of Physiology* 288.1 (Mar. 1979), pp. 613–34. ISSN: 0022-3751.

[7]   Holger Dietze. *Die optometrische Untersuchung*. Georg Thieme Verlag, Apr. 23, 2008. DOI: 10.1055/b-0034-39913.

[8]   Albert J. Augustin and James F. Collins. *Augenheilkunde*. Springer, 2001. DOI: 10.1007/978-3-662-05922-7.

[9]   Andreas Bringmann, Steffen Syrbe, Katja Görner, Johannes Kacza, Mike Francke, Peter Wiedemann, and Andreas Reichenbach. „The primate fovea: Structure, function and development." In: *Progress in Retinal and Eye Research* 66 (Sept. 2018), pp. 49–84. DOI: 10.1016/j.preteyeres.2018.03.006.

[10]   Patrick Scheibe, Anfisa Lazareva, Ulf-Dietrich Braumann, Andreas Reichenbach, Peter Wiedemann, Mike Francke, and Franziska G. Rauscher. „Parametric model for the 3D reconstruction of individual fovea shape from OCT data." In: *Experimental Eye Research* 119 (Feb. 2014), pp. 19–26. DOI: 10.1016/j.exer.2013.11.008.

[11]   Toco Y. P. Chui, Zhangyi Zhong, Hongxin Song, and Stephen A. Burns. „Foveal avascular zone and its relationship to foveal pit shape." In: *Optometry & Vision Science* 89.5 (May 2012), p. 602. DOI: 10.1097/opx.0b013e3182504227.

[12]   Julia Lamparter, Richard A. Russell, Haogang Zhu, Ryo Asaoka, Takehiro Yamashita, Tuan Ho, and David F. Garway-Heath. „The Influence of Intersubject Variability in Ocular Anatomical Variables on the Mapping of Retinal Locations to the Retinal Nerve Fiber Layer and Optic Nerve Head." In: *Investigative Opthalmology & Visual Science* 54.9 (Sept. 2013), p. 6074. DOI: 10.1167/iovs.13-11902.

[13]   Myron Yanoff and Jay S. Duker. „Structure and Function of the Neural Retina." In: *Ophthalmology: Expert Consult*. 3rd ed. Elsevier Health Sciences, Dec. 2013. Chap. 6.1, pp. 511–514. DOI: 10.1097/00006982-199903000-00022.

[14]   Early Treatment Diabetic Retinopathy Study Research Group. „Classification of Diabetic Retinopathy from Fluorescein Angiograms: ETDRS Report Number 11." In: *Ophthalmology* 98.5, Supplement (May 1991), pp. 807–822. ISSN: 0161-6420. DOI: 10.1016/S0161-6420(13)38013-0.

[15]   Florian M. Heussen, Yanling Ouyang, Emma C. McDonnell, Ramsudha Narala, Humberto Ruiz-Garcia, Alexander C. Walsh, and SriniVas R. Sadda. „Comparison of manually corrected retinal thickness measurements from multiple spectral-domain optical coherence tomography instruments." In: *British Journal of Ophthalmology* 96.3 (July 6, 2011), pp. 380–385. DOI: 10.1136/bjo.2010.201111.

[16]   Sandeep Grover, Ravi Keshavamurthy, Vikram S. Brar, and Kakarala V. Chalam. „Comparison of Retinal Thickness in Normal Eyes Using Stratus and Spectralis Optical Coherence Tomography." In: *Investigative Ophthalmology & Visual Science* 51.5 (May 2010), p. 2644. DOI: 10.1167/iovs.09-4774.

[17]   Ilse Krebs, Eva Smretschnig, Sarah Moussa, Werner Brannath, Irene Womastek, and Susanne Binder. „Quality and Reproducibility of Retinal Thickness Measurements in Two Spectral-Domain Optical Coherence Tomography Machines." In: *Investigative Ophthalmology & Visual Science* 52.9 (Aug. 2011), p. 6925. DOI: 10.1167/iovs.10-6612.

[18]   Ute E. K. Wolf-Schnurrbusch, Lala Ceklic, Christian K. Brinkmann, Milko E. Iliev, Manuel Frey, Simon P. Rothenbuehler, Volker Enzmann, and Sebastian Wolf. „Macular Thickness Measurements in Healthy Eyes Using Six Different Optical Coherence Tomography Instruments." In: *Investigative Ophthalmology & Visual Science* 50.7 (July 2009), p. 3432. DOI: 10.1167/iovs.08-2970.

[19]   Gordon L. Walls. „Significance of the foveal depression." In: *Archives of Ophthalmology* 18.6 (Dec. 1937), pp. 912–919. DOI: 10.1001/archopht.1937.00850120046005.

[20]   Gustav Valentin. „Ein Beitrag zur Kenntniss der Brechungsverhältnisse der Thiergewebe." German. In: *Archiv für die gesamte Physiologie des Menschen und der Tiere* 19.1 (Jan. 1879), pp. 78–105. ISSN: 0365-267x. DOI: 10.1007/BF01639843.

[21]   Gordon L. Walls. „Postscript On Image Expansion By The Foveal Clivus." In: *Archives of Ophthalmology* 23.4 (Apr. 1940), pp. 831–832. ISSN: 0003-9950. DOI: 10.1001/archopht.1940.00860130925009.

[22]   Richard J. Pumphrey. „The theory of the fovea." In: *Journal of Experimental Biology* 25.3 (Apr. 1948), pp. 299–312. ISSN: 0022-0949.

[23]   Stephen L. Polyak. *The Retina*. 1st ed. The University of Chicago Press, 1941.

[24]   John F. Fulton. *A Text-book of Physiology*. W. B. Saunders, 1955.

[25]   Eugene Wolff. *The Anatomy of the Eye and its Orbit*. H. K. Lewis and Co., Ldt., 1948.

[26]   Robert A. Weale. „Why Does the Human Retina Possess a Fovea?" In: *Nature* 212.5059 (Oct. 1966), pp. 255–256. DOI: 10.1038/212255a0.

[27] Robert A. Weale. „Polarized light and the human fundus oculi." In: *The Journal of Physiology* 186.1 (Sept. 1966), pp. 175–186. DOI: 10.1113/jphysiol.1966.sp008027.

[28] Lindesay Harkness and Henry C. Bennet-Clark. „The deep fovea as a focus indicator." In: *Nature* 272.5656 (May 1978), pp. 814–816. DOI: 10.1038/272814a0.

[29] Allan W. Snyder and William H. Miller. „Telephoto lens system of falconiform eyes." In: *Nature* 275.5676 (Sept. 1978), pp. 127–129. DOI: 10.1038/275127a0.

[30] Robert Fox, Stephen W. Lehmkuhle, and David H. Westendorf. „Falcon visual acuity." In: *Science* 192.4236 (Apr. 1976), pp. 263–265. DOI: 10.1126/science.1257767.

[31] Pedro E. Maldonado, Humberto Maturana, and Francisco J. Varela. „Frontal and Lateral Visual System in Birds." In: *Brain, Behavior and Evolution* 32.1 (July 1988), pp. 57–62. DOI: 10.1159/000116532.

[32] Susana Bloch and Carlos Martinoya. „Comparing frontal and lateral viewing in the pigeon. I. Tachistoscopic visual acuity as a function of distance." In: *Behavioural Brain Research* 5.3 (July 1982), pp. 231–244. DOI: 10.1016/0166-4328(82)90031-6.

[33] Stig Steenstrup and Ole Munk. „Optical Function of the Convexiclivate Fovea with Particular Regard to Notosudid Deep-sea Teleosts." In: *Optica Acta: International Journal of Optics* 27.7 (July 1980), pp. 949–964. DOI: 10.1080/713820342.

[34] N. Adam Locket. „Problems of deep foveas." In: *Australian and New Zealand Journal of Ophthalmology* 20.4 (Dec. 1992), pp. 281–295. ISSN: 1440-1606. DOI: 10.1111/j.1442-9071.1992.tb00740.x.

[35] Andreas Reichenbach, Kristian Franze, Silke Agte, Stephan Junek, Antje Wurm, Jens Grosche, Alexej Savvinov, Jochen Guck, and Serguei N. Skatchkov. „Live cells as optical fibers in the vertebrate retina." In: *Selected topics on optical fiber technology*. InTech, Feb. 2012. Chap. 10, pp. 247–270. DOI: 10.5772/2429.

[36] Anita E. Hendrickson and Cristine Yuodelis. „The Morphological Development of the Human Fovea." In: *Ophthalmology* 91.6 (June 1984), pp. 603–612. ISSN: 0161-6420. DOI: 10.1016/S0161-6420(84)34247-6.

[37] Daniel J. O'Leary. „The Radius of Curvature of the Human Foveal Pit." In: *The Australian Journal of Optometry* 68.5 (Sept. 1985), pp. 179–182. ISSN: 1444-0938. DOI: 10.1111/j.1444-0938.1985.tb00999.x.

[38] David Huang, Eric A. Swanson, Charles Lin, Joel S. Schuman, William G. Stinson, Warren Chang, Michael R. Hee, Thomas Flotte, Kenron Gregory, and Carmen A. Puliafito. „Optical coherence tomography." In: *Science* 254.5035 (Dec. 1991), pp. 1178–1181. ISSN: 0036-8075. DOI: 10.1126/science.1957169.

[39] Joseph M. Schmitt. „Optical Coherence Tomography (OCT): a review." In: *IEEE Journal on Selected Topics in Quantum Electronics* 5.4 (Aug. 1999), pp. 1205–1215. DOI: 10.1109/2944.796348.

[40] Wolfgang Drexler. „Ultrahigh-resolution optical coherence tomography." In: *Journal of Biomedical Optics* 9.1 (Feb. 2004), p. 47. DOI: 10.1117/1.1629679.

[41]   Wolfgang Drexler and James G. Fujimoto. „State-of-the-art retinal optical coherence tomography." In: *Progress in Retinal and Eye Research* 27.1 (Jan. 2008), pp. 45–88. DOI: 10.1016/j.preteyeres.2007.07.005.

[42]   Daniel F. Kiernan, William F. Mieler, and Seenu M. Hariprasad. „Spectral-Domain Optical Coherence Tomography: A Comparison of Modern High-Resolution Retinal Imaging Systems." In: *American Journal of Ophthalmology* 149.1 (Jan. 2010), 18–31.e2. DOI: 10.1016/j.ajo.2009.08.037.

[43]   Michelle L. Gabriele, Gadi Wollstein, Hiroshi Ishikawa, Juan Xu, Jongsick Kim, Larry Kagemann, Lindsey S. Folio, and Joel S. Schuman. „Three dimensional optical coherence tomography imaging: Advantages and advances." In: *Progress in Retinal and Eye Research* 29.6 (Nov. 2010), pp. 556–579. ISSN: 1350-9462. DOI: 10.1016/j.preteyeres.2010.05.005.

[44]   Pei-Chang Wu, Yin-Ju Chen, C-H Chen, Y-H Chen, S-J Shin, H-J Yang, and Hsu-Ko Kuo. „Assessment of macular retinal thickness and volume in normal eyes and highly myopic eyes with third-generation optical coherence tomography." In: *Eye* 22.4 (Apr. 2007), pp. 551–555. ISSN: 0950-222X. DOI: 10.1038/sj.eye.6702789.

[45]   Sandeep Grover, Ravi Keshavamurthy, Vikram S. Brar, and Kakarala V. Chalam. „Normative Data for Macular Thickness by High-Definition Spectral-Domain Optical Coherence Tomography (Spectralis)." In: *American Journal of Ophthalmology* 148.2 (June 2009), pp. 266–271. ISSN: 0002-9394. DOI: 10.1016/j.ajo.2009.03.006.

[46]   Toco Y. P. Chui, Dean A. VanNasdale, Ann E. Elsner, and Stephen A. Burns. „The Association Between the Foveal Avascular Zone and Retinal Thickness." In: *Investigative Ophthalmology & Visual Science* 55.10 (Sept. 30, 2014), p. 6870. DOI: 10.1167/iovs.14-15446.

[47]   Sotaro Ooto, Masanori Hangai, Atsushi Sakamoto, Atsuo Tomidokoro, Makoto Araie, Tomohiro Otani, Shoji Kishi, Kenji Matsushita, Naoyuki Maeda, Motohiro Shirakashi, Haruki Abe, Hisashi Takeda, Kazuhisa Sugiyama, Hitomi Saito, Aiko Iwase, and Nagahisa Yoshimura. „Three-Dimensional Profile of Macular Retinal Thickness in Normal Japanese Eyes." In: *Investigative Ophthalmology & Visual Science* 51.1 (Jan. 2010), p. 465. DOI: 10.1167/iovs.09-4047.

[48]   Sarah Tick, Florence Rossant, Itebeddine Ghorbel, Alain Gaudric, José-Alain Sahel, Philippe Chaumet-Riffaud, and Michel Paques. „Foveal Shape and Structure in a Normal Population." In: *Investigative Ophthalmology & Visual Science* 52.8 (July 2011), p. 5105. DOI: 10.1167/iovs.10-7005.

[49]   Susan E. Yanni, Jingyun Wang, Melody Chan, Joseph Carroll, Sina Farsiu, Joel N. Leffler, Rand Spencer, and Eileen E. Birch. „Foveal avascular zone and foveal pit formation after preterm birth." In: *British Journal of Ophthalmology* 96.7 (Apr. 29, 2012), pp. 961–966. DOI: 10.1136/bjophthalmol-2012-301612.

[50]   Adam M. Dubis, John T. McAllister, and Joseph Carroll. „Reconstructing foveal pit morphology from optical coherence tomography imaging." In: *British Journal of Ophthalmology* 93.9 (2009), pp. 1223–1227. DOI: 10.1136/bjo.2008.150110.

[51] Adam M. Dubis, Benjamin R. Hansen, Robert F. Cooper, Joseph Beringer, Alfredo Dubra, and Joseph Carroll. „Relationship between the Foveal Avascular Zone and Foveal Pit Morphology.“ In: *Investigative Ophthalmology & Visual Science* 53.3 (Mar. 2012), p. 1628. DOI: 10.1167/iovs.11-8488.

[52] Melissa Wagner-Schuman, Adam M. Dubis, Rick N. Nordgren, Yuming Lei, Daniel Odell, Hellen Chiao, Eric Weh, William Fischer, Yusufu Sulai, Alfredo Dubra, and Joseph Carroll. „Race- and Sex-Related Differences in Retinal Thickness and Foveal Pit Morphology.“ In: *Investigative Ophthalmology & Visual Science* 52.1 (Aug. 2011), pp. 625–634. ISSN: 1552-5783. DOI: 10.1167/iovs.10-5886.

[53] Yoreh Barak, Mark P. Sherman, and Shlomit Schaal. „Mathematical Analysis of Specific Anatomic Foveal Configurations Predisposing to the Formation of Macular Holes.“ In: *Investigative Ophthalmology & Visual Science* 52.11 (Oct. 2011), p. 8266. DOI: 10.1167/iovs.11-8191.

[54] Brooke Nesmith, Akash Gupta, Taylor Strange, Yuval Schaal, and Shlomit Schaal. „Mathematical Analysis of the Normal Anatomy of the Aging Fovea.“ In: *Investigative Ophthalmology & Visual Science* 55.9 (Sept. 2014), p. 5962. DOI: 10.1167/iovs.14-15278.

[55] Yin Ding, Brian Spund, Sofya Glazman, Eric M. Shrier, Shahnaz Miri, Ivan Selesnick, and Ivan Bodis-Wollner. „Application of an OCT data-based mathematical model of the foveal pit in Parkinson disease.“ English. In: *Journal of Neural Transmission* 121.11 (Nov. 2014), pp. 1367–1376. ISSN: 0300-9564. DOI: 10.1007/s00702-014-1214-2.

[56] Andrew Turpin, Siyuan Chen, Juan A. Sepulveda, and Allison M. Mckendrick. „Customizing Structure-Function Displacements in the Macula for Individual Differences.“ In: *Investigative ophthalmology & visual science* 56 (Sept. 2015), pp. 5984–5989. DOI: 10.1167/iovs.15-17384.

[57] Lei Liu, Wendy L. Marsh-Tootle, Elise N. Harb, Wei Hou, Qinghua Zhang, Heather A. Anderson, Thomas T. Norton, Katherine K. Weise, Jane E. Gwiazda, Leslie Hyman, and the COMET Group. „A sloped piecemeal Gaussian model for characterising foveal pit shape.“ In: *Ophthalmic and Physiological Optics* 36.6 (Oct. 2016), pp. 615–631. DOI: 10.1111/opo.12321.

[58] Juan A. Sepulveda, Andrew Turpin, and Allison M. Mckendrick. „Individual Differences in Foveal Shape: Feasibility of Individual Maps Between Structure and Function Within the Macular Region.“ In: *Investigative ophthalmology & visual science* 57 (Sept. 2016), pp. 4772–4778. DOI: 10.1167/iovs.16-19288.

[59] Sunil K. Yadav, Seyedamirhosein Motamedi, Timm Oberwahrenbrock, Frederike C. Oertel, Konrad Polthier, Friedemann Paul, Ella M. Kadas, and Alexander U. Brandt. „CuBe: parametric modeling of 3D foveal shape using cubic Bézier.“ In: *Biomedical Optics Express* 8.9 (Aug. 2017), p. 4181. DOI: 10.1364/boe.8.004181.

[60] Anett Karl, Silke Agte, Astrid Zayas-Santiago, Felix N. Makarov, Yomarie Rivera, Jan Benedikt, Mike Francke, Andreas Reichenbach, Serguei Skatchkov, and Andreas Bringmann. „Retinal adaptation to dim light vision in spectacled caimans (Caiman crocodilus fuscus): Analysis of retinal ultrastructure.“ In: *Experimental eye research* 173 (May 2018), pp. 160–178. DOI: 10.1016/j.exer.2018.05.006.

[61]   Bret A. Moore, Luke P. Tyrrell, Jason M. Kamilar, Shaun P. Collin, Nathaniel J. Dominy, Margaret I. Hall, Christopher P. Heesy, Thomas J. Lisney, Ellis R. Loew, Gillian L. Moritz, Saúl S. Nava, Eric Warrant, Kara E. Yopak, and Esteban Fernández-Juricic. „Structure and Function of Regional Specializations in the Vertebrate Retina." In: *Evolution of Nervous Systems*. Elsevier, Jan. 2017, pp. 351–372. DOI: 10.1016/b978-0-12-804042-3.00008-7.

[62]   Neil A. Gershenfeld. *The Nature of Mathematical Modeling*. Cambridge University Press, Nov. 1998. ISBN: 0521570956.

[63]   Sunil K. Yadav. „Surface Denoising based on The Variation of Normals and Retinal Shape Analysis." PhD thesis. Freie Universität Berlin, Oct. 2018.

[64]   Milton Abramowitz and Irene A. Stegun. *Pocketbook of Mathematical Functions*. Ed. by Milton Abramowitz and Irene A. Stegun. Harri Deutsch Verlag, 1984. ISBN: 3871448184.

[65]   Brian Gough. *GNU Scientific Library Reference Manual - Third Edition*. Network Theory Ltd., Jan. 2009. ISBN: 0954612078.

[66]   Wolfram Research, Inc. (Champaign, Illinois). *Mathematica Version 11.3*. 2018. URL: https://www.wolfram.com.

[67]   Ulrich Pinkall and Konrad Polthier. „Computing discrete minimal surfaces and their conjugates." In: *Experiment. Math.* 2.1 (Feb. 1993), pp. 15–36. DOI: 10.1080/10586458.1993.10504266.

[68]   Matthias Steffen. „A simple method for monotonic interpolation in one dimension." In: *Astronomy and Astrophysics* 239 (Nov. 1990), p. 443. DOI: 10.1016/b978-0-12-448750-5.50006-2.

[69]   Patrick Scheibe, Maria T. Zocher, Mike Francke, and Franziska G. Rauscher. „Analysis of foveal characteristics and their asymmetries in the normal population." In: *Experimental Eye Research* 148 (2016), pp. 1–11. ISSN: 0014-4835. DOI: 10.1016/j.exer.2016.05.013.

[70]   Marcus Wagner, Patrick Scheibe, Mike Francke, Beatrice Zimmerling, Katharina Frey, Mandy Vogel, Stephan Luckhaus, Peter Wiedemann, Wieland Kiess, and Franziska G. Rauscher. „Automated detection of the choroid boundary within OCT image data using quadratic measure filters." In: *Journal of Biomedical Optics* 22.2 (Feb. 2017), p. 025004. DOI: 10.1117/1.jbo.22.2.025004.

[71]   Katharina Frey, Beatrice Zimmerling, Patrick Scheibe, Franziska G. Rauscher, Andreas Reichenbach, Mike Francke, and Robert Brunner. „Does the foveal shape influence the image formation in human eyes?" In: *Advanced Optical Technologies* 6.5 (2017), pp. 403–410. DOI: 10.1515/aot-2017-0043.

[72]   Rainer Storn and Kenneth Price. „Differential Evolution – A Simple and Efficient Heuristic for global Optimization over Continuous Spaces." In: *Journal of Global Optimization* 11 (4 Jan. 1997), pp. 341–359. ISSN: 0925-5001. DOI: 10.1023/A:1008202821328.

[73]   Ankush Mandal, Aveek Das, Prithwijit Mukherjee, Swagatam Das, and Ponnuthurai Suganthan. „Modified differential evolution with local search algorithm for real world optimization." In: *Proc. IEEE Congr. Evol. Comput.* (June 2011), pp. 1565–1572. DOI: 10.1109/CEC.2011.5949802.

[74] Maurice Herlihy and Nir Shavit. *The Art of Multiprocessor Programming, Revised Reprint*. Amsterdam: Morgan Kaufmann, May 2012. ISBN: 978-0-123-97337-5.

[75] Nicholas J. Higham. *Accuracy and Stability of Numerical Algorithms*. SIAM: Society for Industrial and Applied Mathematics, Aug. 2002. ISBN: 0898715210.

[76] Maria T. Zocher, Jos J. Rozema, Nicole Oertel, Jens Dawczynski, Peter Wiedemann, and Franziska G. Rauscher. „Biometry and visual function of a healthy cohort in Leipzig, Germany.“ In: *BMC Ophthalmology* 16.1 (June 2016), p. 79. ISSN: 1471-2415. DOI: 10.1186/s12886-016-0232-2.

[77] David F. Garway-Heath, Alicja R. Rudnicka, Tom Lowe, Paul J. Foster, Frederick W. Fitzke, and Roger A. Hitchings. „Measurement of optic disc size: equivalence of methods to correct for ocular magnification.“ In: *British Journal of Ophthalmology* 82.6 (June 1998), pp. 643–649. DOI: 10.1136/bjo.82.6.643.

[78] Richard A. Armstrong. „Statistical guidelines for the analysis of data obtained from one or both eyes.“ In: *Ophthalmic and Physiological Optics* 33.1 (Jan. 2013), pp. 7–14. ISSN: 1475-1313. DOI: 10.1111/opo.12009.

[79] Michael R. Hee, Carmen A. Puliafito, Carlton Wong, Jay S. Duker, Elias Reichel, Joel S. Schumann, Eric A. Swanson, and James G. Fujimoto. „Imaging fellow eyes in patients diagnosed with idiopathic macular holes using optical coherence tomography (OCT).“ In: *Ophthalmology* 102.suppl (May 1995), pp. 748–756. DOI: 10.1016/S0161-6420(95)30959-1.

[80] Sarah E. Benson, Patricio G. Schlottmann, Catie Bunce, and David G. Charteris. „Comparison of macular hole size measured by optical coherence tomography, digital photography, and clinical examination.“ In: *Eye* 22.1 (Jan. 2008), pp. 87–90. DOI: 10.1038/sj.eye.6702947.

[81] Se W. Kang, Kyeon Ahn, and Don I. Ham. „Types of macular hole closure and their clinical implications.“ In: *British Journal of Ophthalmology* 87.8 (Aug. 2003), pp. 1015–1019. DOI: 10.1136/bjo.87.8.1015.

[82] Jeacheol Shin, Y-K Chu, Y-T Hong, O-W Kwon, and Suk Ho Byeon. „Determination of macular hole size in relation to individual variabilities of fovea morphology.“ In: *Eye* (Aug. 2015). DOI: 10.1038/eye.2015.81.

[83] Mark L. Kirby, Martin Galea, Edward Loane, Jim Stack, Stephen Beatty, and John M. Nolan. „Foveal anatomic associations with the secondary peak and the slope of the macular pigment spatial profile.“ In: *Investigative ophthalmology & visual science* 50.3 (Mar. 2009), pp. 1383–1391. DOI: 10.1167/iovs.08-2494.

[84] François C. Delori, Douglas G. Goger, Claudia Keilhauer, Paola Salvetti, and Giovanni Staurenghi. „Bimodal spatial distribution of macular pigment: evidence of a gender relationship.“ In: *J. Opt. Soc. Am. A* 23.3 (Mar. 2006), pp. 521–538. DOI: 10.1364/JOSAA.23.000521.

[85] Jan M. Provis, Adam M. Dubis, Ted Maddess, and Joseph Carroll. „Adaptation of the central retina for high acuity vision: Cones, the fovea and the avascular zone.“ In: *Progress in Retinal and Eye Research* 35 (July 2013), pp. 63–81. ISSN: 1350-9462. DOI: 10.1016/j.preteyeres.2013.01.005.

[86]   Elisabeth M. Anger, Angelika Unterhuber, Boris Hermann, Harald Sattmann, Christian Schubert, James E. Morgan, Alan Cowey, Peter K. Ahnelt, and Wolfgang Drexler. „Ultrahigh resolution optical coherence tomography of the monkey fovea. Identification of retinal sublayers by correlation with semithin histology sections." In: *Experimental eye research* 78.6 (June 2004), pp. 1117–1125. DOI: 10.1016/j.exer.2004.01.011.

[87]   Wolf Krebs and Ingeborg Krebs. „Primate retina and choroid." In: *New York, London, Heidelberg: Springer Verlag* 8 (1991), p. 134. DOI: 10.1007/978-1-4613-9095-4.

[88]   Ben Fine and Myron Yanoff. *Ocular histology: a text and atlas*. Harper Collins Publishers, 1979.

[89]   Ravi S. Jonnal, Omer P. Kocaoglu, Robert J. Zawadzki, Sang-Hyuck Lee, John S. Werner, and Donald T. Miller. „The Cellular Origins of the Outer Retinal Bands in Optical Coherence Tomography Images-Cellular Origins of the OCT Outer Retinal Bands." In: *Investigative ophthalmology & visual science* 55.12 (Oct. 2014), pp. 7904–7918. DOI: 10.1167/iovs.14-14907.

[90]   Delia F. Cabrera Fernández, Harry M. Salinas, and Carmen A. Puliafito. „Automated detection of retinal layer structures on optical coherence tomography images." In: *Optics Express* 13.25 (Dec. 2005), p. 10200. DOI: 10.1364/opex.13.010200.

[91]   Mircea Mujat, Raymond C. Chan, Barry Cense, Boris H. Park, Chulmin Joo, Taner Akkin, Teresa C. Chen, and Johannes F. de Boer. „Retinal nerve fiber layer thickness map determined from optical coherence tomography images." In: *Optics Express* 13.23 (Dec. 2005), pp. 9480–9491. DOI: 10.1364/OPEX.13.009480.

[92]   Akshaya Mishra, Alexander Wong, Kostadinka Bizheva, and David A. Clausi. „Intra-retinal layer segmentation in optical coherence tomography images." In: *Optics express* 17.26 (Dec. 2009), pp. 23719–23728. DOI: doi:10.1364/OE.17.023719.

[93]   Stephanie J. Chiu, Xiao T. Li, Peter Nicholas, Cynthia A. Toth, Joseph A. Izatt, and Sina Farsiu. „Automatic segmentation of seven retinal layers in SDOCT images congruent with expert manual segmentation." In: *Optics express* 18.18 (Aug. 30, 2010), pp. 19413–19428.

[94]   Alexander Ehnes. „Entwicklung eines Schichtsegmentierungsalgorithmus zur automatischen Analyse von individuellen Netzhautschichten in optischen Kohärenztomographie-B-Scans." PhD thesis. Universitätsbibliothek Giessen, June 2014.

[95]   Mona K. Garvin, Michael D. Abramoff, Xiaodong Wu, Stephen R. Russell, Trudy L. Burns, and Milan Sonka. „Automated 3-D intraretinal layer segmentation of macular spectral-domain optical coherence tomography images." In: *IEEE transactions on medical imaging* 28.9 (Sept. 2009), pp. 1436–1447. DOI: 10.1109/TMI.2009.2016958.

[96]   Kang Li, Xiaodong Wu, Danny Z. Chen, and Milan Sonka. „Optimal surface segmentation in volumetric images-a graph-theoretic approach." In: *IEEE transactions on pattern analysis and machine intelligence* 28.1 (Jan. 2006), pp. 119–134. DOI: 10.1109/TPAMI.2006.19.

[97]   Koenraad A. Vermeer, Josine Van der Schoot, Hans G. Lemij, and Johannes F. de Boer. „Automated segmentation by pixel classification of retinal layers in ophthalmic OCT images." In: *Biomedical optics express* 2.6 (June 2011), pp. 1743–1756. DOI: 10.1364/BOE.2.001743.

[98]   Vedran Kajić, Boris Považay, Boris Hermann, Bernd Hofer, David Marshall, Paul L. Rosin, and Wolfgang Drexler. „Robust segmentation of intraretinal layers in the normal human fovea using a novel statistical model based on texture and shape analysis." In: *Optics express* 18.14 (July 2010), pp. 14730–14744.

[99]   Marcus Wagner. „An Application of Quadratic Measure Filters to the Segmentation of Chorio-Retinal OCT Data." In: *Journal of Mathematical Imaging and Vision* 60.2 (Feb. 2018), pp. 216–231. ISSN: 1573-7683. DOI: 10.1007/s10851-017-0752-2.

[100]   Albert Rich, Patrick Scheibe, and Nasser Abbasi. „Rule-based integration: An extensive system of symbolic integration rules." In: *Journal of Open Source Software* 3.32 (Dec. 2018), p. 1073. DOI: 10.21105/joss.01073.

DECLARATION OF AUTHORSHIP